DISSERTATION

A TRANSIENT, THREE-DIMENSIONAL NUMERICAL STUDY OF CHEMICAL VAPOR DEPOSITION IN BATCH REACTORS

Submitted by

William Wangard, III

Department of Mechanical Engineering

In partial fulfillment of the requirements

for the degree of Doctor of Philosophy

Colorado State University

Fort Collins, Colorado

Summer 2001

COLORADO STATE UNIVERSITY

March 15, 2001

WE HEREBY RECOMMEND THAT THE DISSERTATION PREPARED UNDER OUR SUPERVISION BY WILLIAM WANGARD, III, ENTITLED "A TRANSIENT, THREE-DIMENSIONAL NUMERICAL STUDY OF CHEMICAL VAPOR DEPOSITION IN BATCH REACTORS," BE ACCEPTED AS FULFILLING IN PART THE REQUIREMENTS FOR THE DEGREE OF DOCTOR OF PHILOSOPHY.

Committee on Graduate Work

Co-adviser

Adviser

Department Head

ABSTRACT

A TRANSIENT, THREE-DIMENSIONAL NUMERICAL STUDY OF CHEMICAL VAPOR DEPOSITION IN BATCH REACTORS

A time-accurate model of multicomponent reacting flow with homogeneous and heterogeneous chemical reactions was developed to simulate the transport phenomena, gas-phase chemistry, and deposition profiles in constant-volume chemical vapor deposition reactors with arbitrarily complex geometry in two or three dimensions. A fully rigorous multicomponent gas transport model including thermal diffusion was used. A transformation was applied to the matrix of ordinary diffusion coefficients to form a matrix of effective ordinary diffusion coefficients. This transformation permitted a decoupling of the species continuity equations from one another. A first-order, time-accurate splitting procedure was used to integrate the species and energy equations, which were stiff due to terms arising from the homogeneous and heterogeneous chemical reactions. The stiff equations were solved with the CVODE library. A variable-density projection method was used to solve the variable-property momentum equations. The partial differential equations describing the model were discretized using a conservative finite difference method implemented on overset grids. The overset method was used to obtain solutions on arbitrarily complex geometrical domains. A computer code was developed using the OVERTURE object-oriented class library. The CHEMKIN library was used to compute thermodynamic properties of multicomponent mixtures of ideal gases and homogeneous reaction rates. The CHEMKIN TRANSPORT library was used to compute multicomponent transport properties. The SURFACE CHEMKIN library was used to compute the heterogeneous reaction rates. Numerical simulations included natural convection in two-dimensional horizontal

and tilted reactors, chemical vapor deposition in a three-dimensional reactor with a heterogeneous chemistry, chemical vapor deposition in a two-dimensional reactor with moderately complex homogeneous and heterogeneous chemistry, and a CPU timing study with a system with a complicated homogeneous and heterogeneous reaction model. Results indicated that the solver obtained accurate solutions in CVD batch systems having complicated homogeneous and heterogeneous reaction models for both small and moderate Rayleigh number flows.

William Wangard, III
Department of Mechanical Engineering
Colorado State University
Fort Collins, Colorado 80523
Summer 2001

To Dad, with love ...

November 19, 1935 — February 9, 2000

"Don't worry, Gromit. Everything's under control!"

— The Wrong Trousers, AARDMAN ANIMATIONS, 1993

ACKNOWLEDGEMENTS

I can say without a moment's hesitation that I never could have finished this work without the love and support of many, many people. I am indebted to all of you.

Let me give thanks first to my many friends here in Colorado. To Joe and Tonia: thanks for the many movies, backyard barbecues, duck tales, hearty helpings of roast beef with Yorkshire pudding, and homemade jam. To Heather: thanks for the late night shopping sprees, bike rides to wherever, and the many times just spent being together. To Yun, Linda, Wu, Ben, Allyson, Rene, and Kee Hong, thank you for giving me perspective on what I've tried to accomplish.

To the Selep family — Di, Wayne, Matthew, Mike, Julie, thank you for being with me while being so far away. Your love and friendship has helped me in my darkest moments.

To my adviser, David Dandy: thank you for being so patient and supportive over these many years. Not only did you help me find a research project that was both challenging and exciting, you helped me accomplish a higher goal than I thought was possible.

To my mentor and friend Bill Henshaw: I can't thank you enough for all your wisdom, advice, assistance and good humour.

To my family — Angela, Alex, and Mom, thanks for standing behind me every step of the way with love and enthusiasm. And finally, to my dad, thank you for being such a wonderful father. I love you so much.

TABLE OF CONTENTS

LIST OF FIGURES

LIST OF TABLES

Roman Letters

Name	Description	Units
$\boldsymbol{A}$	Stoichiometric coefficient matrix for homogeneous reactions	—
A_i	Pre-exponential factor for the ith chemical reaction	reaction dep.
A	Area	cm^2
a_m	Activity of the mth species	—
$\boldsymbol{B}$	Stoichiometric coefficient matrix for heterogeneous reactions	—
B_i	Landau-Teller rate law constant	$\mathrm{K}^{1/3}$
$\boldsymbol{C}$	Mole-mass fraction conversion matrix	—
C_i	Landau-Teller rate law constant	$\mathrm{K}^{2/3}$
c	Total concentration in gas phase	$\mathrm{mol\,cm}^{-3}$
c_m	Partial concentration of the mth species	$\mathrm{mol\,cm}^{-3}$
$\boldsymbol{d^T}$	Multicomponent thermal diffusion coefficients	$\mathrm{g\,cm}^{-1}\,\mathrm{s}^{-1}$
d_m^T	Multicomponent thermal diffusion coefficient of the mth species	$\mathrm{g\,cm}^{-1}\,\mathrm{s}^{-1}$
c_p	Mean specific heat capacity at constant pressure	$\mathrm{erg\,g}^{-1}\,\mathrm{K}$
c_{p_m}	Specific heat capacity at constant pressure of the mth species	$\mathrm{erg\,g}^{-1}\,\mathrm{K}$
c_v	Mean specific heat capacity at constant volume	$\mathrm{erg\,g}^{-1}\,\mathrm{K}$
c_{vm}	Specific heat capacity at constant volume of the mth species	$\mathrm{erg\,g}^{-1}\,\mathrm{K}$

$\boldsymbol{D}$	Matrix of multicomponent ordinary diffusion coefficients	$\mathrm{cm^2\,s^{-1}}$
D_{mn}	The mnth element of $\boldsymbol{D}$	$\mathrm{cm^2\,s^{-1}}$
$\boldsymbol{e_g}$	Unit vector pointing in the direction of $\boldsymbol{g}$	
e	Mean specific internal energy	$\mathrm{erg\,g^{-1}}$
e_m	Specific internal energy of the mth species	$\mathrm{erg\,g^{-1}}$
e_{f_m}	Standard heat of formation of the mth species	$\mathrm{erg\,g^{-1}}$
$\boldsymbol{F}$	Stoichiometric coefficient matrix for forward chemical reactions	—
$\boldsymbol{g}$	Body force per unit mass, $\lvert\boldsymbol{g}\rvert = g$	$\mathrm{cm\,s^{-2}}$
$\boldsymbol{g}_m$	Body force per unit mass on the mth species	$\mathrm{cm\,s^{-2}}$
$\Delta\hat{g}_i^0$	Standard molar Gibb's free energy of the ith reaction	$\mathrm{erg\,mol^{-1}}$
$\hat{g}_m^0$	Standard state molar Gibb's free energy of the mth species	$\mathrm{erg\,mol^{-1}}$
$\hat{h}_m^0$	Standard state molar enthalpy of the mth species	$\mathrm{erg\,mol^{-1}}$
h_m	Partial specific enthalpy of the mth species (includes energy of formation)	$\mathrm{erg\,g^{-1}}$
$\boldsymbol{I}$	The identity (or unit) tensor	—
I	The number of chemical reactions (homogeneous or heterogeneous)	—
J	Jacobian transformation	
$\boldsymbol{j}$	Vector of diffusion flux of all species	$\mathrm{g\,cm^{-2}\,s^{-1}}$
$\boldsymbol{j}_m$	Diffusion flux of the mth species	$\mathrm{g\,cm^{-2}\,s^{-1}}$
K_g	Number of gas phase species	—

$K_s(n)$	Number of surface phase species in the nth surface phase	—
$K_b(n)$	Number of bulk phase species in the $n$the bulk phase	—
k	Thermal conductivity	$\mathrm{erg\,s^{-1}\,cm^{-1}\,K^{-1}}$
k_B	Boltzmann's constant	$\mathrm{erg\,K^{-1}}$
k_{p_i}	Equilibrium constant of the ith chemical reaction	reaction dep.
k_{f_i}	Forward rate constant of the ith chemical reaction	reaction dep.
k_{r_i}	Reverse rate constant of the ith chemical reaction	reaction dep.
$\boldsymbol{L}^{ij,kl}$	Block matrices used to compute transport coefficients	$\mathrm{K\,s^3\,g^{-1}\,cm^{-1}}$
M	Number of gas phase species ($=K_g$)	—
$\boldsymbol{n}$	Surface normal vector	—
N_b	Number of bulk phases	—
N_s	Number of surface phases	—
$\mathcal{N}$	Avogadro's number	$\mathrm{mol^{-1}}$
$\boldsymbol{P}$	Inverse of the $\boldsymbol{L}^{00,00}$ matrix	$\mathrm{g\,cm\,K^{-1}\,s^{-3}}$
p	Thermodynamic pressure	$\mathrm{dyne\,cm^{-2}}$
p_d	Dynamic pressure	$\mathrm{dyne\,cm^{-2}}$
p_s	Static pressure	$\mathrm{dyne\,cm^{-2}}$
p_o	Background (or mean) pressure	$\mathrm{dyne\,cm^{-2}}$
p_{atm}	Atmospheric pressure	$\mathrm{dyne\,cm^{-2}}$
$\boldsymbol{q}$	Heat flux vector	$\mathrm{erg\,cm^{-2}\,s^{-1}}$

q_i	Rate of progress variable for the ith chemical reaction	$\mathrm{mol\,cm^{-3}\,s^{-1}}$
$\boldsymbol{R}$	Stoichiometric coefficient matrix for reverse chemical reactions	—
$\mathcal{R}$	Universal gas constant	$\mathrm{erg\,mol^{-1}\,K^{-1}}$
R	$(\mathcal{R}/\tilde{w})$	$\mathrm{erg\,g^{-1}\,K^{-1}}$
R_m	Universal gas constant divided by molecular weight of mth species	$\mathrm{erg\,g^{-1}\,K^{-1}}$
r_m	Production rate of mth species from homogeneous chemical reaction	$\mathrm{mol\,cm^{-3}\,s^{-1}}$
$\boldsymbol{S}$	Total stress tensor	$\mathrm{dyne\,cm^{-2}}$
s_m	Molar production rate of mth species from heterogeneous chemical reaction	$\mathrm{mol\,cm^{-2}\,s^{-1}}$
s_{mn}	Average molecular diameter of the mth and nth species	cm
$\hat{s}^0_m$	Molar standard state entropy of the mth species	$\mathrm{erg\,mol^{-1}\,K^{-1}}$
$\boldsymbol{T}$	Viscous stress tensor	$\mathrm{dyne\,cm^{-2}}$
t	Time	s
$\boldsymbol{u}$	Mass-average velocity	$\mathrm{cm\,s^{-1}}$
$\boldsymbol{u}_m$	Velocity of the mth species in gas mixture	$\mathrm{cm\,s^{-1}}$
$\tilde{\boldsymbol{u}}_m$	Diffusion velocity of the mth species in gas mixture	$\mathrm{cm\,s^{-1}}$
V	Volume	$\mathrm{cm^3}$
$\boldsymbol{W}$	Diagonal Matrix of molecular weights	$\mathrm{g\,mol^{-1}}$
$\tilde{w}$	Mean molecular weight of gas mixture	$\mathrm{g\,mol^{-1}}$
w_m	Molecular weight of mth species	$\mathrm{g\,mol^{-1}}$

$z_k(n)$	Site fraction of the kth surface species in the nth surface phase	—

Greek Letters

β_i	Temperature exponent in reaction kinetics	—
$\mathbf{\Gamma}$	Effective ordinary multicomponent diffusion coefficients	$\mathrm{cm\,s^{-2}}$
γ_n	Density of sites of phase n	$\mathrm{mol\,cm^{-2}}$
γ_n^0	Standard-state surface site density of site type n	$\mathrm{mol\,cm^{-2}}$
δ_m	Molecular (or Lennard-Jones) diameter of the mth species	cm
δ_m^*	Reduced dipole moment	—
ϵ_m	Lennard-Jones potential well depth	erg/k_B
ζ_m	Dipole moment of species m	Debye
η_k	Areal concentration of the kth surface species	$\mathrm{mol\,cm^{-2}}$
θ	Temperature	K
θ_m^*	Reduced temperature of the mth species	—
λ	Mean free path	cm
λ_m	Mean free path of the mth species in gas mixture	cm
μ	Viscosity of the gas mixture	$\mathrm{g\,cm^{-1}\,s^{-1}}$
ξ_m	Symbol for the mth chemical species	—
ρ	Mass density of gas mixture	$\mathrm{g\,cm^{-3}}$
ρ_m	Partial density of the mth species in gas mixture	$\mathrm{g\,cm^{-3}}$

ρ_s	Static fluid density field	$\mathrm{g\,cm^{-3}}$
$\tilde{\rho}$	Difference between actual density and static fluid density	$\mathrm{g\,cm^{-3}}$
ρ_m''	Areal density of solid film	$\mathrm{g\,cm^{-2}}$
σ_m	Mass production rate of mth species from heterogeneous chemical reaction	$\mathrm{g\,cm^{-2}\,s^{-1}}$
ς	Solution vector for computation of transport properties	$\mathrm{erg\,s^{-1}\,cm^{-1}\,K^{-1}}$
$\boldsymbol{\chi}$	Vector containing the mole fractions	—
χ_m	Mole fraction of the mth species in the gas mixture	—
$\boldsymbol{\psi}$	Vector containing the mass fractions	—
ψ_m	Mass fraction of the mth species in gas mixture	—
$\upsilon_k(n)$	Number of sites that species k occupies on the nth phase	—
$\Omega^{(2,2)*}$	Collision integral	—

Characteristic Quantities

c_{vc}	Characteristic mean specific heat capacity at constant volume	$\mathrm{erg\,g^{-1}\,K^{-1}}$
D_c	Characteristic ordinary diffusion coefficient	$\mathrm{cm^2\,s^{-1}}$
e_c	Characteristic specific internal energy	$\mathrm{erg\,g^{-1}}$
k_c	Characteristic thermal conductivity	$\mathrm{erg\,s^{-1}\,cm^{-1}\,K^{-1}}$
l_c	Characteristic length	cm
r_c	Characteristic gas-phase chemical production rate	$\mathrm{g\,cm^{-3}\,s^{-1}}$

u_c	Characteristic velocity	$\mathrm{cm\,s^{-1}}$
θ_c	Characteristic temperature	K
$\Delta_c\theta$	Characteristic temperature difference	K
μ_c	Characteristic viscosity	$\mathrm{g\,cm^{-1}\,s^{-1}}$
ρ_c	Characteristic density	$\mathrm{g\,cm^{-3}}$
$\Delta_c\rho$	Characteristic density difference	$\mathrm{g\,cm^{-3}}$

Dimensionless Groups

Kn	Knudsen number: λ/l_c	—
Gr	Grashof number: $\rho_c\Delta_c\rho g l_c^3/\mu^2$	—
Pr	Prandtl number: $\mu_c c_{vc}/k_c$	—
E	Energy generation number: $e_c r_c l_c^2/(k_c\Delta_c\theta)$	—
Ga	Gay-Lussac number: $\Delta_c\theta/\theta_c$	—
Sc	Schmidt number: $\mu_c/(\rho_c D_c)$	—
Da	Gas phase Damköhler number: $r_c l_c^2/(\rho_c D_c)$	—
Le	Lewis number: Pr/Sc	—

Chapter 1

INTRODUCTION

This dissertation presents the development of a model of thermally-activated chemical vapor deposition in batch reactors. The model is developed from the general conservation laws and rigorous transport theory of multicomponent gases. A computer code is developed to numerically solve the model with real fluid properties and a wide range of chemical reaction mechanisms in geometrically complex reactors.

1.1 Background

1.1.1 A General Description of Chemical Vapor Deposition

Chemical vapor deposition (CVD) is a process used to deposit a film (or coating) onto a substrate by means of a series of chemical reactions with gaseous reactants. The properties of the film and the substrate are fundamentally important to the functionality of many products and devices, such as integrated circuits (Blewer and McConica, 1989), optical coatings (Jensen, 1989), protective coatings, and lasers (Nakamura and Fasol, 1997).

Chemical vapor deposition involves gas phase (homogeneous) and surface (heterogeneous) chemical reactions combined with transport processes. A schematic representation of the elements of the process are shown for a region near a reacting surface is shown in Fig. (1.1). The chemical and transport processes can be summarized as follows:

1. homogeneous chemical reactions which produce additional gaseous (and possibly ionic) species,

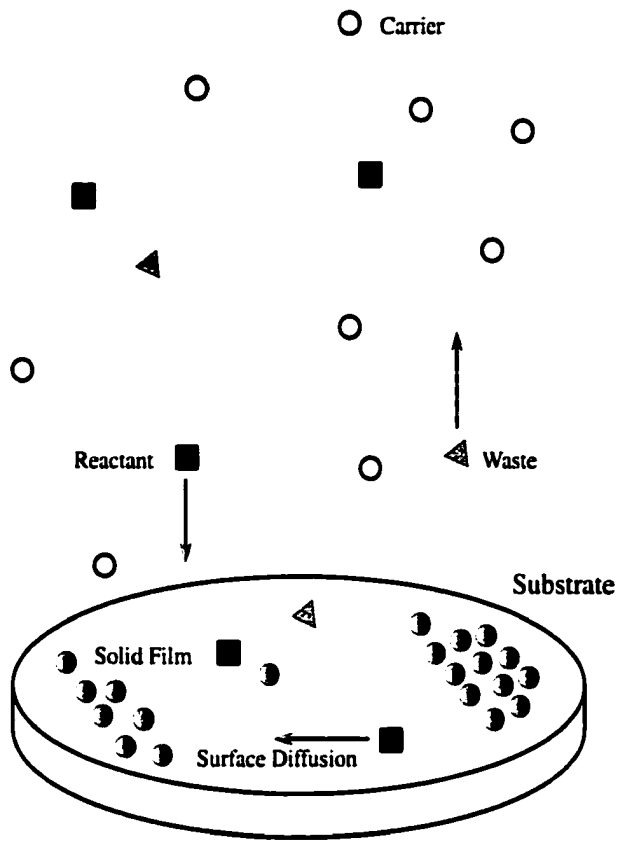

Figure 1.1: Schematic of a CVD process.

2. mass transport by convection and diffusion of gaseous species in the bulk region to the surface.

3. chemisorption of gaseous species.

4. surface diffusion of the chemisorbed (surface) species,

5. heterogeneous reactions which produce a solid film and other surface and gas phase species,

6. desorption of the surface species into the gas phase, and

7. mass transport of the reaction products into the bulk region.

There are many categories of CVD processes. These include thermally-activated

CVD, plasma-enhanced CVD, UV radiation-enhanced CVD, laser-induced CVD, electron-beam assisted CVD, and ion-beam assisted CVD (Morosanu, 1990). In each of these systems, the distinguishing characteristic is the type of energy source used to activate the chemical reactions. CVD is also characterized by the chemical reactants used in the system, such as in OMCVD, in which the reactants include organometallic species. Atmospheric-pressure and low-pressure CVD, in which case the system is run near atmospheric pressure or reduced pressures on the order of 1 Torr (Morosanu, 1990). This work is concerned primarily with the modeling of thermally-activated CVD, operated at either low- or atmospheric pressures, with a variety of possible chemical gas phase species.

1.1.2 Modeling of CVD Reactors

Numerically simulating a CVD system involves several steps. The first is to chose the scale on which the system is modeled: microscopic or macroscopic. Microscopic scale CVD modeling focuses on the mechanisms behind the growth of solid films due to heterogeneous reaction processes, such as nucleation phenomena, island growth, and surface diffusion (Jensen, 1989). Macroscopic CVD modeling focuses on the mechanisms governing the transport phenomena on the interior of the reactor. These phenomena include, of course, convection and diffusion of gas species in a multicomponent mixture. Macroscopic CVD models may include kinetic mechanisms for surface and gas phase reactions, but these are generally obtained from literature, and generally assumed to be valid representations of the physical processes that are actually occurring. Sensitivity analysis is useful to determine the relevance of particular chemical reactions in a particular mechanism (Kee et al., 1996; Ern and Giovangigli, 1995), and these analyses can performed without solving a fully two- or three-dimensional simulation.

The vast majority of experimental (and numerical) CVD is conducted in contin-

uous flow reactors. In a continuous flow reactor, the system is operated under steady state conditions. This is done so that process control is as straightforward as possible. Time is eliminated from the list of process variables, such as system pressure, substrate temperature, gas flow rates, etc. A set of various continuous flow CVD reactor geometries is shown in Fig. (1.2). Some designs are more suited towards particular CVD chemistries, total substrate surface area, etc. The substrate is affixed to the susceptor, which is maintained at (approximately) constant temperature by heating or cooling, depending on the particular CVD system.

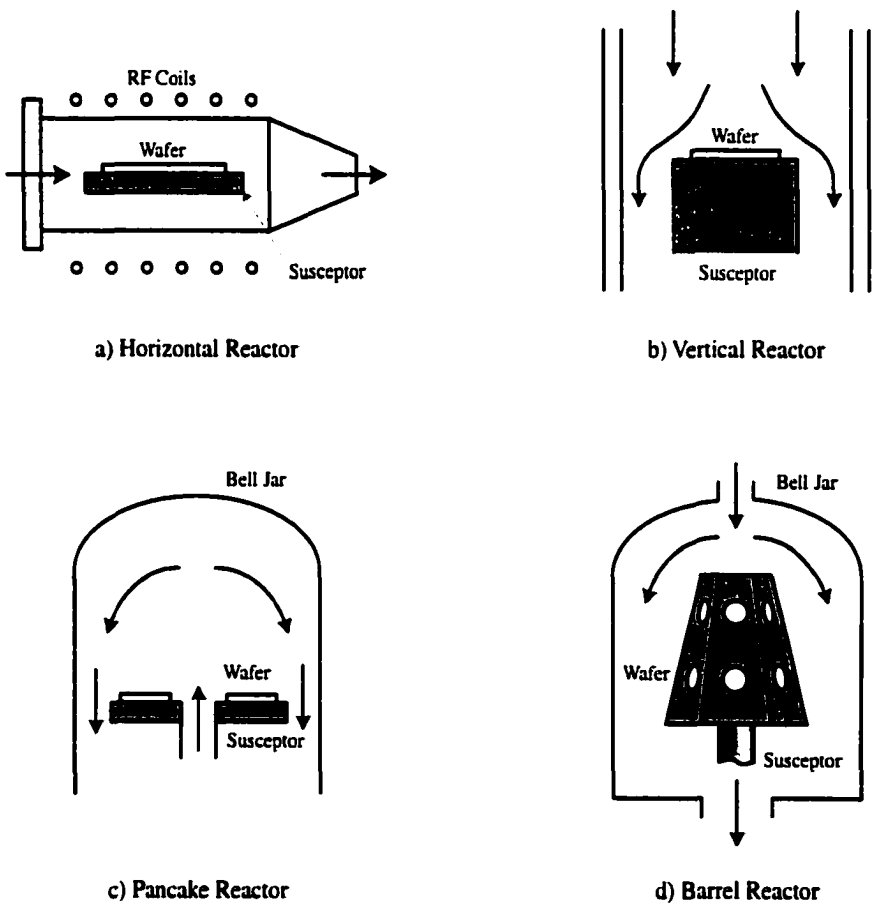

Figure 1.2: Sketches of several continuous flow thermal CVD reactor configurations (Kleijn, 1991).

In Ern et al. (1996), a numerical model of a three-dimensional, horizontal channel,

steady continuous flow CVD reactor was developed to study gallium arsenide growth from trimethylgallium and arsine source reactants. Fluid flow and temperature computations were computed using a vorticity-velocity formulation of the Navier-Stokes and energy balance equations. Detailed gas phase and surface chemistry mechanisms were incorporated. A rigorous theory of multicomponent gas transport was used (Ern and Giovangigli, 1994). The model was used to predict deposition profiles and complex buoyancy-induced flow phenomena that commonly occurs in these types of reactors (Jensen, 1989).

In Kleijn and Hoogendoorn (1991) and Kleijn (1991), numerical simulations of of thermally-activated CVD in continuous flow systems were studied. CVD chemistries were tungsten by hydrogen reduction of tungsten hexafluoride, tungsten deposition by silane reduction, and gallium arsenide deposition by trimethylgallium and arsine. Homogeneous reaction kinetics were ignored, and heterogeneous reaction kinetics were simplified. Reactor geometries investigated include flow in axisymmetric pedestal reactors, and horizontal channel reactors. In more recent studies of steady flow reactors, detailed homogeneous and heterogeneous reaction mechanisms were included Okkerse et al. (1998, 2000)

A recent study of CVD in geometrically complex steady flow reactors was published by Salinger et al. (1999). In this work, CVD of gallium arsenide was simulated in a horizontal flow reactor. Effect of susceptor tilt angle was studied. An earlier study of three-dimensional flow effects in a steady flow horizontal reactor demonstrated that wall temperatures and velocity profiles are strongly coupled (Moffat and Jensen, 1988). The chemistry studied was homoepitaxial deposition of silicon from silane. Dilute reactants were assumed to simplify the equations governing the conservation of species. A simplified model of gas phase and surface kinetics was employed compared to the model of Coltrin et al. (1984). In that work a detailed gas phase and surface reaction kinetic mechanism was used, along with a rigorous

model of multicomponent gas transport, but the results were for two-dimensional, steady state CVD systems.

The theory of multicomponent gas transport is an important aspect of CVD modeling. Many papers have focused on the importance of studying various aspects of these phenomena. The kinetic theory of multicomponent transport is based on the original works of Maxwell and Boltzmann (Boltzmann, 1964). The first detailed solution of the theory was presented almost simultaneously by Enskog and Chapman, in 1916 and 1917, respectively. In their work, they explicitly derived the relationship between mass diffusion and the various driving forces (concentration gradients, temperature gradients, pressure gradients, and body force differences between species). These results are compiled in the work by Chapman and Cowling (1939).

A complete formalism for computing the transport coefficients in a multicomponent gas mixture was given by Hirschfelder et al. (1954). Additional theory and implementation was supplemented by Monchick and Mason (1961), and implemented a computer code (Kee et al., 1986). Other formalisms for the theory have been developed by Ferziger and Kaper (1972) and Ern and Giovangigli (1994).

Several studies have been performed to show the importance of using rigorous multicomponent models for simulating gas transport processes. The importance of thermal diffusion in CVD systems has been thoroughly investigated (Holstein, 1988; Kleijn and Hoogendoorn, 1991; Kleijn et al., 1989; Jenkinson and Pollard, 1984). Results of these works show that thermal diffusion should not be neglected; errors in the deposition rates up to 30% may result without this effect. The reciprocal phenomena, called the diffusion-thermo (or Dufour heat flux) has been shown to be negligible (Jenkinson and Pollard, 1984; Kleijn, 1991; Holstein, 1988). Simplified methods for the computation of multicomponent gas transport have received mixed results. In Kleijn (1991), a simplified transport model yielded errors of less than 5%. The dilute limit approximation for the transport properties computed by the

methods of Ern and Giovangigli (1994) yielded poor accuracy in Ern et al. (1996) and Ern and Giovangigli (1995).

1.2 Motivation

The primary goal of this work is to develop a rigorous model of thermally-activated CVD in batch reactors with complex geometry. (Hereafter, unless otherwise indicated, CVD implies thermally-activated CVD.) Until now, there has not been any significant model development for CVD batch systems.

A CVD **batch** system consists of vessel that is charged with mixture of reactant gases and is operated with no flow into or out of the reactor during the deposition process. Any of the reactor configurations shown in Fig. (1.2) could be used in batch mode if the inlet and outlet ports were closed during the operation of the unit.

There are several issues which motivate the study of CVD batch reactors. A major advantage is the nearly complete utilization of the limiting reactant species and minimal waste of high purity carrier gases. The deposition rate is determined by the concentration of the reactant species near the surface of the reactor. In some CVD systems such as low pressure CVD of tungsten (10^{-3}–10 Torr), the predominant transport mechanism is diffusion, consequently the near-surface gas composition is nearly identical to the reactor exit composition. In the work of McConica et al. (1994), tungsten was deposited in a batch reactor by hydrogen reduction of tungsten hexafluoride and was carried out at 64 Torr; results were compared to a commercial continuous flow CVD reactor operated at 80 Torr. High purity carriers were not used in the batch system; thus, even at the lower system pressure, the reactant concentrations were higher than in the continuous flow reactor. Tungsten films of thickness 2380 Åwere grown on a 6 inch diameter silicon wafer. The deposition times in the batch reactor and continuous flow reactor were 14 and 48 seconds, respectively.

The continuous flow reactor also generated 680 times (by volume) more effluent gas that had to be processed, since it operated at a low reactant utilization (5%). The higher surface concentrations in the batch system yielded faster growth rates and the lack of high purity carriers saved on material costs.

Deposition profiles in some reactors may improve if operated under batch conditions. Obtaining uniformly thick films is difficult to achieve experimentally (and numerically) due to the complex nature of the phenomena in CVD systems. The relationship between utilization and film uniformity depends on the nature of the CVD chemistry and the geometry of the reactor. Several studies of steady flow atmospheric CVD of gallium arsenide by trimethylgallium and arsine have been reported (Ern and Giovangigli, 1995; Salinger et al., 1999). In Ern and Giovangigli (1995), the reactant utilization was estimated to be 75%. The nonuniformity in deposition profiles on the susceptor in this study was due not only to high reactant utilization, but also from the formation of longitudinal buoyancy rolls which affected the distribution of reactants at the surface. In Moffat and Jensen (1988), a base case of silicon CVD by reduction of silane in hydrogen in a horizontal channel reactor heated on the entire bottom surface. The utilization was estimated a approximately 1%. The deposition thickness decreased by 53% in the streamwise direction not due to the low conversion, but due to the formation of complex three-dimensional buoyancy rolls. It is likely that these structures could be dampened by increasing the flow rate (Jensen, 1989), but that would decrease the utilization.

Thus, it is possible that batch systems can achieve as good film uniformity as continuous flow CVD systems, but operate at higher conversion, which would be less wasteful. This is the main motivation for this work.

Another motivation of this work is the paucity of modeling of CVD in reactors with geometrical complexity. As the illustrations of the reactor geometries shown in Fig. (1.2) show, the geometry of CVD reactors are not always simple. Susceptors are

sometimes tilted to take advantage of buoyancy effects. Barrel shaped susceptors are also geometrically complex. In this work, a numerical solution is obtained in complex geometries by using the overset grid method (Henshaw, 1998), and using a general curvilinear finite difference method to solve the differential equations arising from the CVD batch model.

1.3 Industrial Applications

The CVD batch solver has several potential industrial applications. Two of these include the following: (1) feasibility of batch CVD design modifications, and (2) investigation of the feasibility of conversion of continuous flow CVD systems to batch operation.

In the first category, this model would be used as a component tool in the design process of a CVD batch system. The design cycle of a CVD reactor may take several years, especially if new technologies are being investigated (Sampath, 2001). Assuming that the model were validated against a prototype system, this model then could be used to assess the efficacy of design modifications such as reactor orientation, operating conditions, and initial conditions. Poor design modifications could be assessed prior to the costly process of building and testing a prototype.

A great deal of care is needed, however, in validation of the batch CVD model against a prototype reactor. Special attention must be made to accurately representing the homogeneous and heterogeneous reaction kinetics. The CVD batch model assumes that these data accurately reflect, in a macroscopic sense, the physical phenomena that result in the formation of new gas species, and indeed that of the formation of the solid film. Failure to obtain accurate kinetic models would render the solution meaningless from the reactor designer's point of view.

In the second category, this work could be used by researchers interested in con-

version of a continuous flow CVD system to batch operation. This type of conversion may be of interest primarily due to the high cost of reactant gases often used. At the time of this writing, one manufacturer's price for Arsine (ArH_3) a gas used in CVD of gallium arsenide devices, is \$8.44 per gram. The cost of more exotic gases is often much more, such as \$32.00 per gram for Germane (GeH_4). If the continuous flow system is operated under conditions leading to low conversion, which may be necessary to have near-constant conditions at the wafer surface, there can be significant savings associated with running in batch mode.

The general procedure for use of this model for such a purpose is straightforward, but not trivial. Ideally, the first step would be to model the flow CVD system with a commercial, academic, or in-house flow CVD code. Of course, it is also necessary to make sure that the reaction kinetics mechanisms are adequately tuned. Next, the same reactor geometry can be modeled in batch mode with this work with the same reaction kinetics models, if they are appropriate over the operating conditions. Initial and operating conditions could by parametrically varied to assess conditions which would yield uniform deposition, or uniform near-surface reactant concentrations. It is important to be able to match the near-surface conditions that occur in a flow system with that of a batch system if one is seeking a simple conversion of the reactor type from flow to batch. Otherwise, the category of use falls back to that of batch reactor design, and this could be cost or time prohibitive.

The primary use of the model would be to identify the reactor conditions that would give as close as possible initial and operating conditions that mimic the near-surface conditions in the flow system. In a batch system this is difficult for several reasons. Since the volume is fixed, changes in mole numbers or average temperature change the operating pressure. Second, as reactants are consumed, the average concentration of these species decreases. This may change the system pressure, and similarly affect the film growth rate or morphology. Also, operating the system in

batch without significantly reducing the reactant gas concentration would be akin to operating the system with low utilization of reactants. Even so, the utilization may still be better than the continuous flow system, and such investigation should not be dismissed out of hand. The actual benefits are highly dependent upon the reactor design and the particular kinetics of the CVD chemistry.

1.4 Summary of Following Chapters

The material in each of the following chapters is summarized as follows:

Chapter 2. The nature of a macroscopically modeled CVD batch reactor is described. Numerical methods for incompressible, multicomponent reacting flow are discussed. Stiffness in the system of equations is addressed. Computation of thermodynamic properties, transport coefficients, and chemical reaction rates are outlined. Grid generation techniques are discussed with emphasis on the overset grid method. The OVERTURE object-oriented framework is introduced.

Chapter 3. The CVD batch model is formally derived. In the first section, the quantities used in multicomponent gas flows are defined. Next, the conservation equations in a multicomponent reacting fluid are given in coordinate free notation. Next, assumptions are made with regard to simplification of the CVD model. The rigorous multicomponent transport constitutive relations are listed. The constitutive equation for the diffusion flux is then cast into a form more suitable for implicit integration of the species conservation equations. The governing equations are then written in their final form after substituting the assumptions and constitutive equations. The thermodynamic properties of multicomponent ideal gas mixtures and homogeneous reaction kinetics are computed by the CHEMKIN software package. The methodology used in this package is summarized. A similar discussion is presented for the SURFACE CHEMKIN software package, which is used to compute the hetero-

geneous reaction rates and the CHEMKIN TRANSPORT software package, which is used to compute the multicomponent transport properties. Finally the initial and boundary conditions of the model are discussed.

Chapter 4. A dimensional analysis of the governing equations is presented. It is shown that the nature of the momentum equation is controlled by the Grashof number, Gr. The divergence of velocity, which appears in the continuity and energy equations, can be scaled locally, or on a volume average basis. The volume basis scaling depends on the rate of reaction at the reactor surfaces due to heterogeneous reaction kinetics. The normalized species continuity equations are functions of the Grashof number; the Schmidt number, Sc; and the homogeneous Damköhler number, Da. The normalized energy equation is a function of the Grashof number; the Prandtl number, Pr, the Schmidt number; and the Energy Generation number, E.

Chapter 5. The numerical solution of the model is discussed. The discretization procedure for solving each of the model equations is presented. First, the species energy equations are solved using a stiff splitting procedure. The non-stiff solves are solved using a linearized implicit method for the diffusive terms and an explicit method on the convective terms. Thermal diffusion is computed explicitly. The energy equation is solved in a similar manner. The species and energy equation terms due to chemical reactions form a spatially decoupled stiff system of equations at each grid point. A stiff solver is used to solve this system. The solution to this system is used to compute the deposition rates. The system pressure is recomputed, and then the momentum equations are solved using a projection method for variable density flows on a collocated grid. The convective and diffusive terms are treated implicitly, while a few terms were treated explicitly.

Chapter 6. The methods by which the solver was validated are discussed. The results of several validation studies are presented. In the first study, natural convection in a thermally driven cavity is compared against a benchmark solution from the

literature. In the second study, CVD in a low-pressure reactor is compared against a model of CVD in a perfectly stirred reactor. After the validation studies, several natural convection problems in a two-dimensional (2-D) domain are investigated, including convection in a box heated on its bottom surface and in a tilted reactor. Several CVD systems are modeled next. The first system is a three-dimensional (3-D) domain with a simple CVD mechanism in which homogeneous kinetics are negligible. Velocity, temperature, gas composition profiles are presented. In addition, uniformity issues at the deposition surface are discussed. In the second system, a CVD system with homogeneous and heterogeneous reaction mechanisms are studied in a 2-D reactor. Finally, the solver CPU requirements are assessed on a CVD system with large and complicated homogeneous and heterogeneous reaction mechanisms.

Chapter 7. The results of the simulations are discussed. Conclusions are then presented. Recommendations for further work are then listed. Finally, the changes necessary to convert the CVD batch solver code to a continuous flow reactor code are discussed.

Chapter 2

THE CVD BATCH MODEL: ASSUMPTIONS AND EQUATIONS

In this chapter, the equations of the CVD batch reactor model are given. The model equations consist of the following:

1. A set of differential equations, boundary conditions, and constraints to determine the local density, temperature, velocity, and composition fields in the reactor domain.

2. Equations to determine quantities such as thermodynamic properties, transport properties, and chemical reaction rates.

The chapter begins with a definition of the CVD batch system. Next, the fundamental quantities relevant to the analysis of multicomponent gas mixtures are defined. A set of assumptions is then made with regard to the model to simplify the resulting governing equations. Each of these assumptions is justified, and the bounds on their validity is discussed. Constitutive equations for the stress tensor, heat flux vector, and diffusion flux vector are presented, and the diffusion flux vector is recast into a more useful form using a transformation. The governing equations are then listed in coordinate-free notation, in completely general form insofar as the assumptions allow. Next, the details of the computations performed by the suite of chemical kinetics and transport packages are presented. Finally, the initial and boundary conditions are discussed.

2.1 Definition of the CVD Batch System

A schematic of a CVD batch reactor is shown in Fig. (2.1). The reactor walls are some solid material that encloses the reactive gas mixture. The walls may be heated, cooled, or insulated, depending on the desired temperature profile of the interior surfaces in the reactor. The susceptor may be actively heated or cooled.

The CVD batch system is defined as the region consisting of the bulk gas of the reactor bounded by the interior surfaces of the reactor. The system for the reactor in Fig. (2.1) is shown in Fig. (2.2). Even though the boundary of the system is shown as a thick line, it actually represents the interior surface of the reactor. The dark black line indicates that the susceptor temperature may be different than the other surfaces of the reactor. In actuality, the temperature distribution of the interior surfaces are coupled to the energy transport processes in the interior. As a simplification, it is assumed that the interior surface temperature distribution is known. It may possibly be computed from a heat transfer model or measured from experimental data. It is also assumed that the physical location of the surface is unaffected by the growth of the deposited film.

2.2 Multicomponent Gas Mixtures

2.2.1 Gas Mixture Quantities

This section describes some of the basic quantities relevant to an analysis of a multicomponent mixture and how these quantities are related. These quantities are the density of the mth species in the mixture, the total density, the concentration of the mth species in the mixture, the total concentration, the mass and mole fraction of the mth species, the molecular weight of the mth species, and the mean molecular weight of the mixture.

The CVD batch reactor contains a mixture of M different gas species. The partial

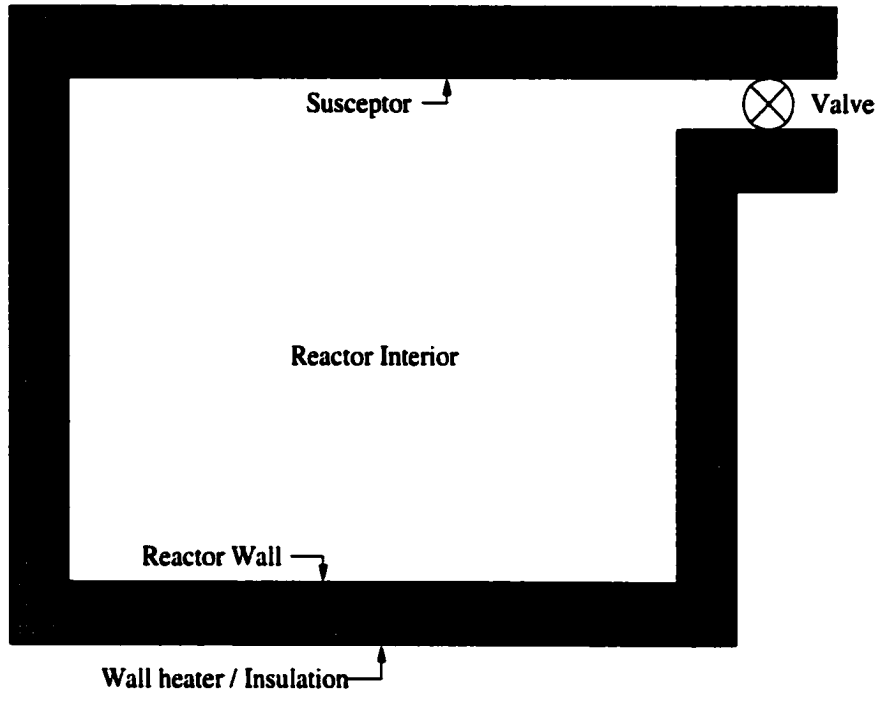

Figure 2.1: Schematic representation of a CVD batch system.

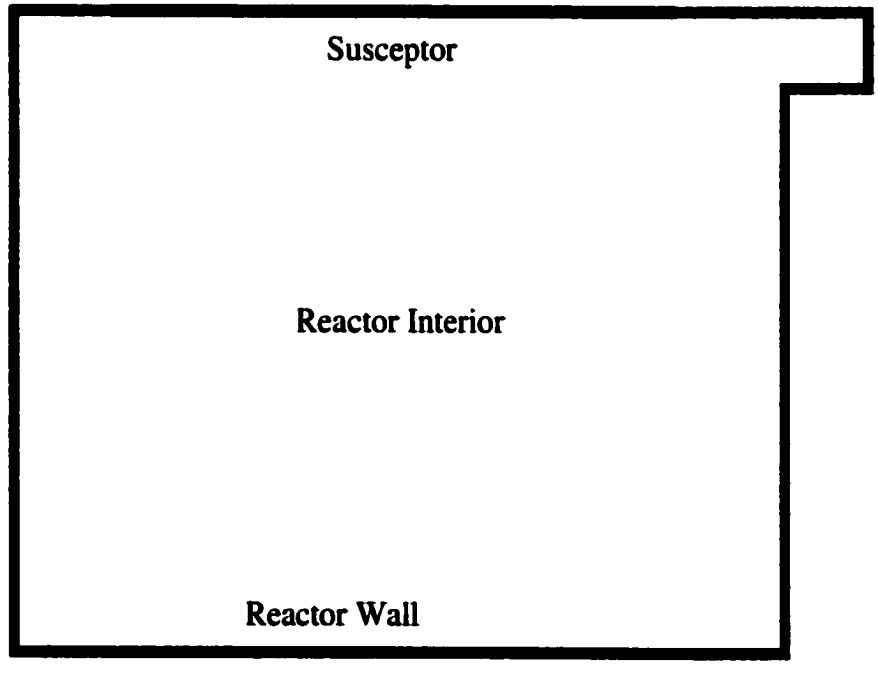

Figure 2.2: A sketch of the CVD batch model system for the reactor schematic shown in Fig. (2.1).

density of the mth species in the mixture, ρ_m, is the mass of the mth species per unit volume. The total density (or just density) of the gas, ρ, is given by

$$\rho = \sum_{m=1}^{M} \rho_m. \tag{2.1}$$

The mass fraction of the mth species, ψ_m, is as follows:

$$\psi_m = \frac{\rho_m}{\rho}. \tag{2.2}$$

The partial concentration of the mth species in the mixture, c_m, is the number of moles of the mth species per unit volume. The total concentration (or just concentration), of the gas, c, is given by

$$c = \sum_{m=1}^{M} c_m. \tag{2.3}$$

The mole fraction of the mth species, χ_m, is as follows:

$$\chi_m = \frac{c_m}{c}. \tag{2.4}$$

Summing Eqns.(2.4) and (2.2) yields the constraint on the mole and mass fractions:

$$\sum_{m=1}^{M} \chi_m = \sum_{m=1}^{M} \psi_m = 1. \tag{2.5}$$

The ratio of a species' density and concentration is equal to its molecular weight:

$$w_m = \frac{\rho_m}{c_m}. \tag{2.6}$$

The mean molecular weight is equal to the ratio of the total density and the total concentration:

$$\bar{w} = \frac{\rho}{c}. \tag{2.7}$$

The ratio of the mass and mole fraction is given by

$$\frac{\psi_m}{\chi_m} = \frac{w_m}{\bar{w}}. \tag{2.8}$$

The mean molecular weight can be computed from the mole fractions or the mass fractions. In terms of the mole fractions,

$$\tilde{w} = \sum_{m=1}^{M} \chi_m w_m. \tag{2.9}$$

This expression may be derived using Eqs.(2.7, 2.1, and 2.4) as follows:

$$\begin{aligned} \tilde{w} &= \frac{\rho}{c} \\ &= \frac{1}{c} \sum_{m=1}^{M} \rho_m \\ &= \sum_{m=1}^{M} \frac{\chi_m \rho_m}{c_m} \\ &= \sum_{m=1}^{M} \chi_m w_m. \end{aligned} \tag{2.10}$$

A similar derivation may be used to show that

$$\tilde{w} = \left(\sum_{m=1}^{M} \frac{\psi_m}{w_m} \right)^{-1}. \tag{2.11}$$

2.2.2 Velocity, Diffusion Velocity, and Diffusion Flux

The species velocity, $\boldsymbol{u}_m$, is the local velocity of the mth species in the bulk mixture. The mass-average velocity (or simply velocity), $\boldsymbol{u}$, is computed by weighting the species velocities by the mass fractions:

$$\boldsymbol{u} = \sum_{m=1}^{M} \psi_m \boldsymbol{u}_m. \tag{2.12}$$

The diffusion velocity of the mth species, $\tilde{\boldsymbol{u}}_m$ is defined as the difference between the species velocity and the mass-average velocity:

$$\tilde{\boldsymbol{u}}_m \equiv \boldsymbol{u}_m - \boldsymbol{u}. \tag{2.13}$$

The diffusion flux of the mth species, $\boldsymbol{j}_m$, is given by

$$\boldsymbol{j}_m \equiv \rho_m \tilde{\boldsymbol{u}}_m, \tag{2.14}$$

and it represents the difference between the total flux of species m and the flux of that species due to bulk motion. Multiplying Eq. (2.13) by ρ_m, summing over all species, and using Eq. (2.12), it may be shown that

$$\sum_{m=1}^{M} \boldsymbol{j}_m = 0. \tag{2.15}$$

The phenomena of mass diffusion can be viewed an expression of the second law of thermodynamics. The flux of species results from various driving forces that are present when the system is not in equilibrium. These driving forces, when present, drive the motion of species in such a way that the entropy of the system increases. The driving forces for mass diffusion are gradients in concentration, the natural logarithm of temperature, and the natural logarithm of pressure. An additional driving force is present when body forces are species-specific, such as in a plasma in the presence of an electric field. The relationship between the diffusion flux and the forces can be obtained from the theory of irreversible thermodynamics (Belfiore. 1999; Hirschfelder et al., 1954) or from the rigorous kinetic theory of dilute gas mixtures (Chapman and Cowling, 1939; Hirschfelder et al., 1954). The rigorous kinetic theory is also used to obtain explicit forms for the transport coefficients in terms of a set of collision integrals. which involve the dynamics of a molecular encounter and hence the intermolecular force law.

2.3 Assumptions

Several assumptions and appropriate justifications are now made in order to simplify the problem. They are as follows:

The continuum hypothesis is valid. A fluid consists of a large number of particles moving and colliding with each other — exchanging momentum and energy. The immense number of particles precludes the the possibility of describing the dynamics of the system by tracking the motion of each individual particle.

The continuum hypothesis is an assumption that the physical properties of the fluid are smooth and continuous functions. This hypothesis is considered valid when the mean free path of the molecules in the gas, λ, is much smaller than the characteristic length of the system of interest, l_c. The ratio of these two quantities is called the Knudsen number, Kn:

$$\mathsf{Kn} \equiv \frac{\lambda}{l_c} \tag{2.16}$$

The fluid is considered a continuum when

$$\mathsf{Kn} \lesssim 0.1. \tag{2.17}$$

In Jeans (1925), the mean free path of the mth species, λ_m, in a binary mixture of elastic, spherical, particles is shown to be

$$\lambda_m = \frac{k_B \theta}{\pi p \sum_n \left(\chi_n s_{mn}^2 \sqrt{1 + w_m/w_n} \right)}, \tag{2.18}$$

where k_B is Boltzmann's constant, θ is the temperature, p is the pressure, and

$$s_{mn} \equiv \frac{1}{2} \left(\delta_m + \delta_n \right). \tag{2.19}$$

where δ_m is the molecular diameter of the ith species.

Consider an example problem to determine the pressure for which a binary mixture of gases at known temperature in a reactor with known characteristic length satisfy the continuum hypothesis. A mixture of diatomic hydrogen, H_2, and tungsten hexafluoride, WF_6, used in CVD of tungsten is assumed. Table (2.1) shows the mean free path of each species normalized by $k_B\theta/p$ as a function of composition, as computed with Eq. (2.18). The second and third columns in the table list the molecular weight and collision cross-section for each species, respectively. The remaining columns give the normalized mean free path of the species as a function of the mole fraction of hydrogen, χ_{H_2}. Let $\theta = 600$ K and $l_c = 0.1$ cm. Using the limiting case

Species	$w\,(\mathrm{g\,mol^{-1}})$	$\delta \times 10^8\,(\mathrm{cm})$	$\lambda p/k_B\theta \times 10^{-13}\,(\mathrm{cm^{-2}})$		
			$\chi_{H_2} = 0.01$	$\chi_{H_2} = 0.50$	$\chi_{H_2} = 0.99$
H_2	2.016	2.92	19.4	22.4	26.3
WF_6	297.840	5.16	8.5	2.7	1.6

Table 2.1: Mean free paths of a binary mixture of hydrogen and tungsten hexafluoride computed by Eq. (2.18). Molecular data are from Kee et al. (1986).

of pure hydrogen, $\lambda p/k_B\theta = 26.3 \times 10^{13}\ \mathrm{cm^{-2}}$. If $\mathsf{Kn} \leq 0.1$, then

$$p > 2200\ \mathrm{dyne\,cm^{-2}}$$

$$> 1.6\ \mathrm{Torr}.$$

Thus, at 600 K, the continuum hypothesis for this mixture of gases is reasonable for pressures greater than 1.6 Torr.

The gas in the reactor is ideal. An ideal gas is a mixture of gas molecules that interact with each other only through collisions. There are no other forces between molecules. This assumption simplifies the equation of state and the relationship between energy and temperature.

The ideal gas law is valid in a multicomponent mixture whenever the partial pressure of the mth species, $\chi_m p$, is much less than the critical pressure of that species, and when the temperature is much greater than the critical temperature (Cengel and Boles, 1989). Since these are conditions are true in all cases considered in this work, the ideal gas law is assumed valid.

The equation of state relating pressure, volume, temperature, and composition in a multicomponent ideal gas mixture is as follows:

$$p = \frac{\rho \mathcal{R} \theta}{\bar{w}}, \tag{2.20}$$

where $\mathcal{R}$ is the universal gas constant. This equation is also written

$$p = \rho R \theta, \tag{2.21}$$

where $R \equiv \mathcal{R}/\tilde{w}$. The gas constant for the mth species, R_m is given by

$$R_m \equiv \frac{\mathcal{R}}{w_m}. \tag{2.22}$$

The relationship between the internal energy and temperature for a mixture of ideal gases is simple. The specific internal energy of pure ideal gas component m, e_m, is a function of temperature alone:

$$e_m(\theta) = e_{f_m} + \int_0^\theta c_{vm}(\theta')\, d\theta', \tag{2.23}$$

where e_{f_m} is the specific energy of formation of the mth species, and c_{v_m} is the specific heat capacity at constant volume of the mth species. The specific energy of formation is the energy released when species m is formed from its elements at the standard state.

The internal energy of a mixture of ideal gases is additive. Thus, the specific internal energy of the mixture is given by

$$e = \sum_{m=1}^{M} \psi_m e_m. \tag{2.24}$$

Differentiating this expression yields

$$\frac{De}{Dt} = c_v \frac{D\theta}{Dt} + \sum_{m=1}^{M} e_m \frac{D\psi_m}{Dt}, \tag{2.25}$$

where the mean specific heat capacity at constant volume, c_v, is defined by

$$c_v \equiv \sum_{m=1}^{M} \psi_m c_{vm}. \tag{2.26}$$

The gas is transparent to radiation. At low pressures and temperatures, the energy transport due to radiative exchange in gases is negligible compared to the energy transport due to either convection or conduction. This assumption is considered reasonable for temperatures less than 2500 K and pressures of 1 atmosphere or less (Siegel and Howell, 1981). Radiative heat exchange between interior surfaces of the CVD walls is not negligible, and must be included in an analysis to determine interior wall temperatures. However, in this work, all interior surface temperatures are assumed to be known.

The gas is Newtonian. This assumption is valid for gases, and most low- to moderate-weight liquids. A general indication of the validity of the Newtonian model for fluids is based on the ratio of two time scales: (1) the time scale representative of the rate at which the fluid can respond to achieve a new flow state when subjected to transient forces, and (2) the characteristic time represented by the rate of change of the strain tensor. If the first time scale is much smaller than the second, then the fluid essentially responds instantaneously to transient forces on the fluid, and the fluid stresses are always in local equilibrium. While this condition is valid for gases and low- to moderate-molecular weight liquids, it is rarely true for high-molecular weight liquids and in any fluid subject to extremely rapid changes in strain rates (Leal, 1992). In thermal CVD, the Newtonian model is considered valid under all circumstances normally encountered (Kleijn, 1991).

Gravity is the only body force. It is assumed that the body force is the same for all gas species, $\boldsymbol{g}_m = \boldsymbol{g}$. This assumption simplifies the momentum and energy equations and causes forced mass diffusion (Bird et al., 1960; Hirschfelder et al., 1954) to vanish identically. This assumption is not valid if the gas contains charged species in the presence of electric and/or magnetic fields.

Ionization is negligible. Due to the previous assumption, the dynamics of the system cannot include charged gas species. This assumption is valid for CVD systems in which the equilibrium constant for dissociation is small. Some CVD processes, such as plasma-enhanced CVD, specifically depend on the dynamics and chemical reactions of ionic species (Morosanu, 1990), but these systems are not considered in this work.

The Dufour effect is negligible. The heat flux resulting from concentration gradients, commonly called the DuFour effect, results from the complex intermolecular collisions in a multicomponent gas (Hirschfelder et al., 1954). It has been shown to be negligible under nearly all operating conditions (Holstein, 1988; Jenkinson and

Pollard, 1984). The DuFour effect is often several orders of magnitude than that of ordinary heat conduction. It is considered negligible in this work.

The bulk viscosity is negligible. In the constitutive equation for fluid stress, the bulk viscosity is considered negligible, since it is identically zero for monatomic gases, and usually considered unimportant unless the fluid is undergoing processes with extreme dilatation, such as in ultrasonic vibratory flows (Panton, 1990).

Pressure diffusion is negligible. The mass diffusion flux resulting from pressure gradients is proportional to $\nabla \ln p$ (Hirschfelder et al., 1954), which is vanishingly small in systems considered in this work.

Viscous dissipation is negligible. Viscous dissipation is the irreversible conversion of kinetic energy to thermal energy (Leal, 1992; Panton, 1990; Bird et al., 1960). This assumption is reasonable in all CVD batch systems.

2.4 Constitutive Equations

Macroscopically observable phenomena such as fluid stress, heat flux, and mass diffusion, arise from molecular level phenomena. Constitutive equations describe these phenomena in terms of macroscopically observable quantities, such as composition, velocity, and temperature. The constitutive equations for a multicomponent ideal gas mixture at low density (Hirschfelder et al., 1954), simplified by the previous assumptions, are as follows:

Fluid stress:

$$\boldsymbol{S} = -\mu\left(\nabla \boldsymbol{u} + \nabla \boldsymbol{u}^T\right) + \frac{2}{3}\mu \nabla \cdot \boldsymbol{u}\boldsymbol{I} + p\boldsymbol{I}. \tag{2.27}$$

Heat flux:

$$\boldsymbol{q} = -k\nabla\theta + \sum_{m=1}^{M} h_m \boldsymbol{j}_m. \tag{2.28}$$

Mass diffusion flux:

$$\boldsymbol{j}_m = \rho \frac{w_m}{\tilde{w}^2} \sum_{n=1}^{M} w_n D_{mn} \nabla \chi_n - d_m^T \frac{\nabla \theta}{\theta}. \tag{2.29}$$

In the above equations, $\boldsymbol{S}$ is the total fluid stress, μ is the dynamic viscosity, p is the pressure, $\boldsymbol{I}$ is the unit tensor, h_m is the specific enthalpy of mth species, D_{mn} is the mnth element of $\boldsymbol{D}$, the matrix of ordinary multicomponent diffusion coefficients ($D_{mm} \equiv 0$) and d_m^T is the thermal diffusion coefficient of the mth species. By Eq. (2.15),

$$\sum_{m=1}^{M} d_m^T = 0. \tag{2.30}$$

2.5 Diffusion Flux

The diffusion flux given by Eq. (2.29) is written in terms of the gradients of the mole fractions. This is not convenient because the species conservation equations are usually written in terms of mass fractions (or species densities). In Cartesian coordinates, Eq. (2.29) can be written in matrix form as follows:

$$\begin{pmatrix} j_{x1} \\ \vdots \\ j_{xM} \\ j_{y1} \\ \vdots \\ j_{yM} \\ j_{z1} \\ \vdots \\ j_{zM} \end{pmatrix} = \begin{bmatrix} \boldsymbol{WDW} & 0 & 0 \\ 0 & \boldsymbol{WDW} & 0 \\ 0 & 0 & \boldsymbol{WDW} \end{bmatrix} \begin{pmatrix} \frac{\partial \chi_1}{\partial x} \\ \vdots \\ \frac{\partial \chi_M}{\partial x} \\ \frac{\partial \chi_1}{\partial y} \\ \vdots \\ \frac{\partial \chi_M}{\partial y} \\ \frac{\partial \chi_1}{\partial z} \\ \vdots \\ \frac{\partial \chi_M}{\partial z} \end{pmatrix} - \begin{pmatrix} \frac{\partial \ln \theta}{\partial x} d_1^T \\ \vdots \\ \frac{\partial \ln \theta}{\partial x} d_M^T \\ \frac{\partial \ln \theta}{\partial y} d_1^T \\ \vdots \\ \frac{\partial \ln \theta}{\partial y} d_M^T \\ \frac{\partial \ln \theta}{\partial z} d_1^T \\ \vdots \\ \frac{\partial \ln \theta}{\partial z} d_M^T \end{pmatrix}, \tag{2.31}$$

where $\boldsymbol{W} = \mathrm{diag}[w_1, \ldots, w_M]$. Note that the vectors are of length $3M$, where M is the number of species. Since the matrix $\boldsymbol{WDW}$ acts on each spatial component independently, a shorthand notation for the above equation is introduced:

$$\boldsymbol{j} = \frac{\rho}{\tilde{w}^2} \boldsymbol{WDW} \nabla \boldsymbol{\chi} - \frac{\nabla \theta}{\theta} \boldsymbol{d^T}, \tag{2.32}$$

where the vector $\boldsymbol{j}$ is of length M, but it is implied that this same equation applies to each spatial dimension. Hereafter, this notation will be used for operations of this type.

The gradients in mole fraction of mth species can be written in terms of the gradients of the mass fractions of mth species using the following:

$$\boldsymbol{\nabla}\chi_m = \sum_{n=1}^{M} C_{mn}\boldsymbol{\nabla}\psi_n, \tag{2.33}$$

where

$$C_{mn} \equiv \frac{\partial \chi_m}{\partial \psi_n}. \tag{2.34}$$

Differentiating the conversion formula between mole fraction and mass fraction, Eq. (2.8), yields

$$C_{mn} = \left(\delta_{mn} - \psi_m \frac{\tilde{w}}{w_n}\right)\frac{\tilde{w}}{w_m}, \tag{2.35}$$

where δ_{mn} is the Kronecker delta. Thus,

$$\boldsymbol{\nabla\chi} = \boldsymbol{C\nabla\psi}. \tag{2.36}$$

It can be shown that $\boldsymbol{C}$ is singular, since its columns sum to zero. This is proven as follows:

$$\begin{aligned}
\sum_{i=1}^{M} C_{mn} &= \sum_{i=1}^{M}\left(\delta_{mn} - \psi_m \frac{\tilde{w}}{w_n}\right)\frac{\tilde{w}}{w_m}, \\
&= \frac{\tilde{w}}{w_n} - \sum_{m=1}^{M}\psi_m \frac{\tilde{w}}{w_m}\frac{\tilde{w}}{w_n}. \\
&= \frac{\tilde{w}}{w_n}\left(1 - \sum_{m=1}^{M}\psi_m \frac{\tilde{w}}{w_m}\right), \\
&= \frac{\tilde{w}}{w_n}\left(1 - \sum_{m=1}^{M}\chi_m\right), \\
&= 0.
\end{aligned} \tag{2.37}$$

Thus, we can write the diffusion flux as follows:

$$\boldsymbol{j} = -\rho\boldsymbol{\Gamma}\boldsymbol{\nabla}\boldsymbol{\psi} - \frac{\boldsymbol{\nabla}\theta}{\theta}\boldsymbol{d}^{\boldsymbol{T}}, \tag{2.38}$$

where

$$\boldsymbol{\Gamma} \equiv -\frac{1}{\tilde{w}^2}\boldsymbol{WDWC}. \tag{2.39}$$

Eq. (2.38) is the formulation for the multicomponent diffusion flux used in the numerical model. It has the same general appearance as the diffusion flux used for binary mixtures (Bird et al., 1960).

It is now shown that Eq. (2.38) is equivalent to the expression for diffusion flux in binary mixtures. Consider the case of $M = 2$. The diffusion flux of each species is given by

$$\begin{aligned} \boldsymbol{j}_1 &= -\rho\Gamma_{11}\boldsymbol{\nabla}\psi_1 - \rho\Gamma_{12}\boldsymbol{\nabla}\psi_2, \\ \boldsymbol{j}_2 &= -\rho\Gamma_{21}\boldsymbol{\nabla}\psi_1 - \rho\Gamma_{22}\boldsymbol{\nabla}\psi_2. \end{aligned} \tag{2.40}$$

From the constraint given by Eq. (2.5), $\boldsymbol{\nabla}\psi_1 = -\boldsymbol{\nabla}\psi_2$. Thus, the above two equations may be written

$$\boldsymbol{j}_1 = -\rho\left(\Gamma_{11} - \Gamma_{12}\right)\boldsymbol{\nabla}\psi_1, \tag{2.41}$$

$$\boldsymbol{j}_2 = -\rho\left(\Gamma_{22} - \Gamma_{21}\right)\boldsymbol{\nabla}\psi_2. \tag{2.42}$$

It can be shown that $\Gamma_{11} - \Gamma_{12} = D_{12}$. First expanding Eq. (2.39) and using $D_{mm} = 0$,

$$\begin{aligned} \boldsymbol{\Gamma} &= -\frac{1}{\tilde{w}^2}\boldsymbol{WDWC}. \\ &= -\frac{1}{\tilde{w}^2}\begin{bmatrix} C_{21}w_1D_{12}w_2 & C_{22}w_1D_{12}w_2 \\ C_{11}w_2D_{21}w_1 & C_{12}w_2D_{21}w_1 \end{bmatrix}. \end{aligned} \tag{2.43}$$

Thus,

$$\begin{aligned}
\Gamma_{11} - \Gamma_{12} &= -\frac{w_1 D_{12} w_2}{\tilde{w}^2}\left(C_{21} - C_{22}\right), \\
&= -\frac{w_1 D_{12} w_2}{\tilde{w}^2}\left[\frac{\tilde{w}}{w_2}\left(-\psi_2\frac{\tilde{w}}{w_1}\right) - \frac{\tilde{w}}{w_2}\left(1 - \psi_2\frac{\tilde{w}}{w_2}\right)\right], \\
&= -\frac{w_1 D_{12} w_2}{\tilde{w}^2}\left[-\chi_2\frac{\tilde{w}}{w_1} - \frac{\tilde{w}}{w_2}x_1\right], \\
&= \frac{D_{12}}{\tilde{w}}\left[\chi_2 w_2 + \chi_1 w_1\right], \\
&= D_{12},
\end{aligned}$$

and by switching subscripts, it is easy to show that $\Gamma_{22} - \Gamma_{21} = D_{21}$.

2.6 Governing Equations

The governing equations are written for a general multicomponent ideal gas using the assumptions and constitutive equations previously discussed. They are as follows:

Continuity: The equation of mass conservation, or continuity equation, is

$$\frac{1}{\rho}\frac{D\rho}{Dt} + \nabla \cdot \boldsymbol{u} = 0. \tag{2.44}$$

Species Continuity: The conservation statement for the mth species in the mixture, or species continuity equation, is

$$\frac{\partial \rho \psi_m}{\partial t} + \nabla \cdot (\rho \boldsymbol{u} \psi_m) = r_m + \nabla \cdot \sum_{n=1}^{M} \rho \Gamma_{mn} \nabla \psi_n + \nabla \cdot \left(\frac{d_m^T}{\theta}\nabla\theta\right) \qquad (m = 1, 2, \ldots, M), \tag{2.45}$$

where r_m is the volumetric mass generation rate of the mth species in the mixture due to homogeneous chemical reaction. Even though this equation is written for all M species, there are only $M - 1$ independent species continuity equations. This is due to the constraint given by Eq. (2.5), namely that the species equations must sum to the total continuity equation.

Momentum: The momentum balance is given by

$$\rho\frac{D\boldsymbol{u}}{Dt} = -\nabla p + \rho\boldsymbol{g} + \nabla\cdot\left(\mu\left(\nabla\boldsymbol{u} + \nabla\boldsymbol{u}^T\right) - \frac{2}{3}\mu\left(\nabla\cdot\boldsymbol{u}\right)\boldsymbol{I}\right). \tag{2.46}$$

Thermal Energy: The conservation of thermal energy is derived by subtracting the mechanical energy equation from the conservation of total energy. The result is as follows:

$$\rho c_v\frac{D\theta}{Dt} = \nabla\cdot\left(k\nabla\theta\right) - p\left(\nabla\cdot\boldsymbol{u}\right) - \sum_{m=1}^{M}\left(e_m r_m + c_{p_m}\left(\boldsymbol{j}_m\cdot\nabla\theta\right) + R_m\theta\nabla\cdot\boldsymbol{j}_m\right). \tag{2.47}$$

2.7 Surface Flux Due to Heterogeneous Chemical Kinetics

During a CVD process, chemical reactions occur at the interfacial surface between the gas and the substrate that result in the formation of a solid film. The net molar production rate per unit area of species m due to heterogeneous chemical reaction, s_m, may be a complicated function of the surface temperature, pressure, the composition of the gas, and the composition of site-specific species on the surface. These reaction rates are computed by SURFACE CHEMKIN (Coltrin et al., 1996). A brief overview of SURFACE CHEMKIN is presented later in this chapter.

The net mass generation rate per unit area is thus

$$\sigma_m = \frac{s_m}{w_m}. \tag{2.48}$$

By convention, $\sigma_m < 0$ for reactants, and $\sigma_m > 0$ for products of the chemical reaction. Mass conservation requires that the flux of gas phase species must be equal to the net mass generation rate per unit area of the gas phase species. Hence,

$$\sigma_m = -\rho_m\boldsymbol{u}_m\cdot\boldsymbol{n}, \tag{2.49}$$

where $\boldsymbol{n}$ is the unit vector normal to the wall that points into the wall.

2.8 Chemical Kinetics and Transport Properties

This section summarizes the computations performed by the CHEMKIN, SURFACE CHEMKIN, and CHEMKIN TRANSPORT packages. The CHEMKIN package (Kee et al., 1996) is used to compute the thermodynamic properties of multicomponent gas mixtures, such as c_v, h_m, e, etc., and it is also used to compute the chemical reaction rates of the gas phase species due to homogeneous chemical reaction, r_m. The SURFACE CHEMKIN package (Coltrin et al., 1996) is used to compute the reaction rates of the gas phase, surface phase, and bulk phase species due to heterogeneous chemical reaction, σ_m. The CHEMKIN TRANSPORT package (Kee et al., 1986) is used to compute the transport properties such as μ and k.

2.8.1 Homogeneous Reaction Rates

Consider a mixture of M gas phase species undergoing a total of I reversible or irreversible chemical reactions. A general expression for this set of reactions can be written

$$\sum_{m=1}^{M} A'_{mi}\xi_m \rightleftharpoons \sum_{m=1}^{M} A''_{mi}\xi_m \quad (i = 1, 2, \ldots, I). \tag{2.50}$$

The stoichiometric coefficients A_{mi} represent the coefficient of the mth species in the ith reaction equation and ξ_m is the symbol for the mth species. The superscripts $'$ and $''$ represent forward and reverse stoichiometric coefficients, respectively. By convention, $A'_{mi} > 0$ and $A''_{mi} > 0$. Since each elementary reaction usually involves only a few species, the stoichiometric coefficient matrix is quite sparse for a large set of reactions.

The net production rate of the mth species, r_m ($\mathrm{g\,cm^{-3}\,s^{-1}}$), is written as follows:

$$r_m = w_m \sum_{i=1}^{I} A_{mi} q_i \quad (m = 1, 2, \ldots, M), \tag{2.51}$$

where $\boldsymbol{A} \equiv \boldsymbol{A}'' - \boldsymbol{A}'$. The rate of progress variable for the ith reaction, q_i, is given

by the difference of the forward and reverse reaction rates.

$$q_i = k_{f_i} \prod_{m=1}^{M} c_m^{F_{mi}} - k_{r_i} \prod_{m=1}^{M} c_m^{R_{mi}}, \tag{2.52}$$

where c_m is the molar concentration of the mth species and k_{f_i} and k_{r_i} are the forward and reverse rate constants of the ith reaction. F_{mi} are the forward reaction orders which normally equal the forward stoichiometric coefficients A'_{mi}, and R_{mi} are reverse reaction orders which normally equal the reverse stoichiometric coefficients A''_{mi}. Both F_{mi} and R_{mi} may take non-integer values to simulate reactions of arbitrary order, but the law of mass action will not be satisfied unless

$$F_{mi} - R_{mi} = A_{mi}. \tag{2.53}$$

The forward rate constants for the I reactions may take the form

$$k_{f_i} = A_i \theta^{\beta_i} \exp\left(-\frac{\hat{E}_i}{\mathcal{R}\theta} + \frac{B_i}{\theta^{1/3}} + \frac{C_i}{\theta^{2/3}}\right), \tag{2.54}$$

where A_i is the pre-exponential factor, β_i is the temperature exponent, and $\hat{E}_i$ is the activation energy of the ith reaction. The additional terms B_i and C_i are used when the reaction follows a Landau-Teller type rate law (Coltrin et al., 1996).

From thermodynamics, the forward and reverse rate constants of the mth reaction are related to each other by

$$\frac{k_{f_i}}{k_{r_i}} = k_{p_i} \left(\frac{p_{atm}}{\mathcal{R}\theta}\right)^{\sum_{n=1}^{M} A_{nm}}. \tag{2.55}$$

where the equilibrium constant of the mth reaction, k_{p_i}, is defined by

$$k_{p_i} \equiv e^{-\Delta \hat{g}_i^0 / \mathcal{R}\theta}. \tag{2.56}$$

The quantity $\Delta \hat{g}_i^0$ is the change in the standard Gibbs free energy of the ith reaction when changing the reactants to products:

$$\Delta \hat{g}_i^0 = \sum_{k=1}^{M} A_{ki} \hat{g}_k^0, \tag{2.57}$$

where $\hat{g}_k^0$ is computed from the identity

$$\hat{g}_k^0 = \hat{h}_k^0 - \theta \hat{s}_k^0, \tag{2.58}$$

and $\hat{h}_k$ and $\hat{s}_k$ are the molar enthalpy and entropy of pure species k at temperature θ.

The molar specific heat capacities at constant pressure, enthalpy, and entropy are evaluated by CHEMKIN from polynomial curve fits for several temperature ranges. The polynomials are computed by regression from the actual values computed by methods of statistical mechanics (Kee et al., 1996). All other thermodynamic properties may be computed from these three.

CHEMKIN also has features to allow for more complex reaction mechanisms, including third-body reactions, unimolecular/recombination fall-off reactions, chemically activated bimolecular reactions. and several types of plasma reactions (Kee et al., 1996).

2.8.2 Heterogeneous Reaction Rates

Consider the region consisting of substrate, the surface of the substrate, and the gas mixture near the surface. The formalism of SURFACE CHEMKIN describes this region as a collection of several types of "phases": gas, surface, and bulk.

The gas phase consists of the mixture of gases above the surface. SURFACE CHEMKIN allows only one gas phase in any one reaction mechanism. The number of species in the gas phase is K_g.

The surface phases consist of the different types of morphological structures that exist at the physical boundary between the solid and the gas. Such phases may be used to describe "ledge" sites, "planar" sites, or any number of features which exist at the surface. In each mechanism, it is assumed that there are N_s surface phases. Each phase contains $K_s(n)$ species in phase n, where $1 \leq n \leq N_s$. It is assumed that surfaces species on one phase are distinct from surface species of the

same composition on a different phase. For example, a hydrogen atom adsorbed onto a ledge site is not necessarily the same as a hydrogen atom adsorbed onto a planar site.

The site fraction of the kth species on the nth phase, $z_k(n)$, is the fraction of the total number of available sites in the nth phase which are occupied by the kth species. The site may also be vacant. Thus for each phase,

$$\sum_{k \in K_s(n)} z_k(n) = 1, \tag{2.59}$$

where the notation $k \in K_s(n)$ implies a summation over all of the species in the nth surface phase.

The areal concentration of the kth surface species, η_k ($\mathrm{mol\,cm^{-2}}$), is given by

$$\eta_k = \frac{z_k(n)\gamma_n}{\upsilon_k(n)}, \tag{2.60}$$

where γ_n is the density of sites of phase n ($\mathrm{mol\,cm^{-2}}$) and $\upsilon_k(n)$ is the number of sites that each species k occupies on the nth phase.

Consider a set of I reversible or irreversible surface reactions involving K chemical species. A general form for these reactions is identical to that in the previous section:

$$\sum_{k=1}^{K} B'_{ki}\xi_k \rightleftharpoons \sum_{k=1}^{K} B''_{ki}\xi_k \quad (i = 1, 2, \ldots, I), \tag{2.61}$$

where B_{ki} are the stoichiometric coefficients and ξ_k is the chemical symbol for the kth species. As with homogeneous kinetics, the stoichiometric matrices are often sparse for large sets of reactions.

The production rate of the kth species per unit area, s_k ($\mathrm{mol\,cm^{-2}\,s^{-1}}$) is given by

$$s_k = \sum_{i=1}^{I} B_{ki} q_i, \tag{2.62}$$

where $\boldsymbol{B} \equiv \boldsymbol{B''} - \boldsymbol{B'}$.

The rate of progress of the ith reaction, q_i is given by the difference between the forward and reverse reaction rates:

$$q_i = k_{f_i} \prod_{k=1}^{K} b_k^{B'_{ki}} - k_{r_i} \prod_{k=1}^{K} b_k^{B''_{ki}}, \tag{2.63}$$

where b_k represents the molar concentration (c_k) for gas phase species, the areal molar concentration (η_k) for surface species, and the activities (a_k) for solid bulk species. The activities of the bulk species normally sum to unity (for ideal solid solutions). See Coltrin et al. (1996) for more details.

A relationship between the forward and reverse rate constants may be determined by considering the system at equilibrium. The result is

$$\frac{k_{f_i}}{k_{r_i}} = k_{p_i} \left(\frac{p_{atm}}{\mathcal{R}\theta}\right)^{\sum_{k\in K_g} B_{ki}} \prod_{n\in N_s} \gamma_n^{0\sum_{k\in K_s(n)} B_{ki}} \prod_{k\in K_s(n)} \upsilon_k^{-B_{ki}}, \tag{2.64}$$

where γ_n^0 is the standard-state surface site density of site type n. For clarity, it is noted that the first sum is taken over all gas phase species, the first product is taken over all surface phases, the second sum is taken over all species in the nth surface phase, and the second product is taken over all species in the nth surface phase. The equilibrium constant of the ith reaction, k_{p_i}, is given by

$$k_{p_i} \equiv e^{-\Delta\hat{g}_i^0/\mathcal{R}\theta}, \tag{2.65}$$

where $\Delta\hat{g}_i^0$ is the change in the Gibbs free energy of the ith reaction by changing the reactants to products at the temperature θ, and at 1 atmosphere pressure:

$$\Delta\hat{g}_i^0 = \sum_{k=1}^{M} B_{ki}\hat{g}_k^0. \tag{2.66}$$

The Gibbs free energies of the species are determined from the enthalpy and entropy, which are computed by interpolation of polynomial curve fits to data generated by methods of statistical mechanics.

In addition, SURFACE CHEMKIN allows for non-integer stoichiometry coefficient, site coverage modification of the rate expression, ion-energy dependent rate expres-

sions, sticking coefficient mechanisms, Bohm rate expressions for ionic reactions, and other methods for simulating heterogeneous kinetics (Coltrin et al., 1996).

2.8.3 Transport Properties

The CHEMKIN TRANSPORT package is used to compute the transport properties needed by the CVD batch model. These properties are the viscosity, μ; the conductivity, k; the thermal diffusion coefficients, $\boldsymbol{d}^T$; and the matrix of ordinary multicomponent diffusion coefficients, $\boldsymbol{D}$.

The mixture viscosity is determined using the Wilke mixture-averaged formula from Wilke (1950):

$$\mu = \sum_{m=1}^{M} \frac{\chi_m \mu_m}{\sum_{n=1}^{M} \chi_n \Phi_{mn}}, \tag{2.67}$$

where

$$\Phi_{mn} = \frac{1}{\sqrt{8}} \left(1 + \frac{w_m}{w_n}\right)^{-1/2} \left(1 + \left(\frac{\mu_m}{\mu_n}\right)^{1/2} \left(\frac{w_n}{w_m}\right)^{1/4}\right)^2, \tag{2.68}$$

and the pure species viscosity is given by

$$\mu_m = \frac{5}{16} \frac{\sqrt{\pi w_m \mathcal{R}\theta}}{\pi \mathcal{N} \delta_m^2 \Omega^{(2,2)*}}. \tag{2.69}$$

In this equation, $\mathcal{N}$ is Avogadro's number and δ_m is the Lennard-Jones collision diameter. The collision integral, $\Omega^{(2,2)*}$, is a function of the reduced temperature

$$\theta_m^* = \frac{k_B \theta}{\epsilon_m} \tag{2.70}$$

and the reduced dipole moment

$$\delta_m^* = \frac{1}{2} \frac{\zeta_m^2}{\epsilon_m \sigma_m^3}. \tag{2.71}$$

where ϵ_m is the Lennard-Jones potential well depth and ζ_m is the dipole moment. This (and other) collision integrals are determined by interpolation from tabulated Stockmayer potentials (Monchick and Mason, 1961).

The thermal conductivity, multicomponent thermal diffusion coefficients and ordinary multicomponent diffusion coefficients are determined from a $3M \times 3M$ block system of equations given by

$$\begin{pmatrix} \boldsymbol{L}^{00,00} & \boldsymbol{L}^{00,10} & 0 \\ \boldsymbol{L}^{10,00} & \boldsymbol{L}^{10,10} & \boldsymbol{L}^{10,01} \\ 0 & \boldsymbol{L}^{01,10} & \boldsymbol{L}^{00,00} \end{pmatrix} \begin{pmatrix} \varsigma_{00} \\ \varsigma_{10} \\ \varsigma_{01} \end{pmatrix} = \begin{pmatrix} 0 \\ \boldsymbol{\chi} \\ \boldsymbol{\chi} \end{pmatrix}, \tag{2.72}$$

where $\boldsymbol{\chi}$ is the vector containing the mole fractions, and ς_{mn} are solution vectors of length M, where M is the number of gas species. The components of the $\boldsymbol{L}$-matrices are functions of the binary diffusion coefficients, the temperature, pressure, the mole fractions, several collision integral ratios, and rotational and vibration contributions of the molecular specific heat capacities. For brevity, they are omitted. Explicit formulae are given in (Kee et al., 1986).

The ordinary multicomponent diffusion coefficients are determined from the inverse of the $\boldsymbol{L}^{00,00}$ matrix. Defining $\boldsymbol{P} \equiv (\boldsymbol{L}^{00,00})^{-1}$,

$$D_{mn} = \frac{16\tilde{w}\theta\chi_m}{25w_n p}\left(P_{mn} - P_{mm}\right). \tag{2.73}$$

Hence, the computational cost for computing the $\boldsymbol{D}$ involves the inversion of an $M \times M$ matrix, in addition to the computation of $\boldsymbol{L}^{00,00}$.

The thermal conductivity and thermal diffusion coefficients are determined by solving Eq. (2.72). Then,

$$k = -\sum_{m=1}^{M} \chi_m \left(\varsigma_{10_m} + \varsigma_{01_m}\right) \tag{2.74}$$

$$d_m^T = \frac{8w_m\chi_m}{5\mathcal{R}}\varsigma_{00_m}. \tag{2.75}$$

2.9 Initial and Boundary Conditions

2.9.1 Initial Conditions

The CVD batch system is assumed to be in thermal and static equilibrium at the moment the reactor is turned on. The system pressure, temperature and com-

position (specified as mole or mass fractions) completely describe the state of the gas. In addition, initial site fractions of the surface species are given. These may be computed beforehand using a package to determine equilibrium site fractions at a surface for a given temperature, pressure and composition, such as SURFKIN (Coltrin et al., 2000).

2.9.2 Boundary Conditions

Boundary Conditions on Temperature

The temperature of the susceptor and other reactor surfaces are assumed to be known functions of position and time:

$$\theta = \theta_w(x, y, z, t) \quad \text{(on interior surfaces)}. \tag{2.76}$$

At symmetry boundaries, the normal component of the gradient of all scalar quantities is zero, thus,

$$\boldsymbol{n} \cdot \nabla\theta = 0 \quad \text{(on symmetry surfaces)}, \tag{2.77}$$

where $\boldsymbol{n}$ is a vector normal to the symmetry surface.

The boundary conditions are numerically approximated using the ghost line method. In this approach, an extra row of points is added just outside the discretization and boundary points that lie within the physical domain of the system. The value of the unknown function at the ghost point is determined by the type of boundary condition on that boundary. In the case of a Dirichlet boundary condition, the value at the boundary point is specified, and value at the ghost point is determined by extrapolation. For a Neumann boundary condition, the discretization of the boundary condition includes the value of the ghost point; its value floats to satisfy the Neumann condition. The details of the implementation of this method in the solver is discussed in the next chapter.

Boundary Conditions on Velocity

On all surfaces, the no-slip condition is used:

$$\boldsymbol{u} \cdot \boldsymbol{t} = 0. \tag{2.78}$$

where $\boldsymbol{t}$ is a tangential vector(s) on the boundary surface. In two dimensions, a surface has one tangential vector, while in three dimensions, a surface has two tangential vectors.

At a reacting surface, the normal component of velocity, called the Stefan velocity, is determined by summing the fluxes of the gaseous species at the wall. By SURFACE CHEMKIN convention,

$$\sigma_m = \begin{cases} < 0 & \text{(for reactant species)}, \\ > 0 & \text{(for product species)}. \end{cases} \tag{2.79}$$

The total flux at the wall is obtained by summing the species fluxes at the surface. The Stefan velocity, u_s, is the total flux at the wall divided by the gas density. If $\boldsymbol{n}$ is the unit-vector pointing toward the surface from the reactor interior, then

$$u_s = \boldsymbol{u} \cdot \boldsymbol{n} = -\frac{1}{\rho} \sum_{m=1}^{M} \sigma_m, \tag{2.80}$$

Boundary Conditions on the Mass Fractions

At all non-reacting surfaces,

$$\boldsymbol{j}_m \cdot \boldsymbol{n} = 0 \quad (m = 1, 2, \ldots, M). \tag{2.81}$$

The flux of species due to heterogeneous chemistry is included as an additional term in the governing equations. As will be discussed in the chapter on the numerical methodology, the species equations are split into two parts: a non-stiff solve followed by a stiff solve. The reaction terms are only included in the stiff solve, in which case the species continuity equation is written in a form which includes boundary flux terms. The non-stiff solves use a zero flux boundary condition on all walls.

2.10 Deposition and Etch Rates

The net creation rate of the bth bulk solid species (in $\mathrm{g\,cm^{-2}\,s^{-1}}$) is given by σ_b. The sign of σ_b determines whether that species is being deposited or etched from the surface. If $\sigma_b > 0$, then the species is being deposited at the surface. If $\sigma_b < 0$, then the species is being etched from the surface. It is possible that some species are deposited at the same time other species are etched. The deposition (or etch) rate, $\dot{D}$, of the solid film is given by the following:

$$\dot{D} = \sum_{b \in N_b} \sigma_b, \tag{2.82}$$

where the summation is taken over all bulk solid species.

The rate of change of the thickness of the film, or the film growth rate, $\dot{G}$, is computed as follows:

$$\dot{G} = \sum_{b \in N_b} \frac{\sigma_b}{\rho_b}, \tag{2.83}$$

where ρ_b is the density of the bth solid bulk species. Since both etching and deposition process may occur, $\dot{G}$ may be positive, negative, or zero.

Chapter 3

REVIEW OF NUMERICAL MODELING ISSUES IN CVD BATCH SYSTEMS AND GRID GENERATION METHODS

The nature of the transport processes inside a macroscopically modeled CVD batch reactor can be described as that of incompressible flow of a reacting, multicomponent gas mixture with chemical reactions at the flowfield boundaries. This chapter outlines the most important issues regarding the numerical solution of this type of system: the nature of incompressible flow; the stiffness in the model equations due to source terms; computation of thermodynamic and transport properties; and computation of homogeneous and heterogeneous reaction rates. A discussion of grid generation is presented with emphasis on the overset grid method. Finally, the OVERTURE framework, which forms the foundation of this work, is introduced, and its functionality is illustrated by an example problem.

3.1 Definition of Incompressible Flow

The mass conservation (or continuity) equation for a general fluid is given by

$$\frac{1}{\rho}\frac{D\rho}{Dt} + \nabla \cdot \boldsymbol{u} = 0, \tag{3.1}$$

where ρ is the fluid density, $\boldsymbol{u}$ is the fluid velocity, and D/Dt is the substantial, or material, derivative operator which "follows the motion" of the fluid (White, 1979).

A flow is defined as incompressible when

$$\frac{1}{\rho}\frac{D\rho}{Dt} = 0. \tag{3.2}$$

This condition is true if the fluid density is constant and uniform. This condition is very nearly true in flows of isothermal liquids, since the density is a very weak function of the pressure in liquids. In flows of gases, this condition prevails when the Mach number, **Ma**, is less than 0.3. The Mach number is defined as the ratio of the local speed to the sound speed in the fluid. Under these conditions, changes in density due to the motion are less than 5% (Anderson, 1989).

The incompressibility condition changes the nature of the mass conservation (or continuity) equation. In compressible flow, the continuity equation is differential equation that predicts the evolution of the fluid density (White, 1979). In incompressible flow, the continuity equation is a constraint equation on the fluid velocity (Ferziger and Peric, 1996). The flow velocities in the case studies considered in this work are consistent with the condition $\mathbf{Ma} \ll 1$, and thus incompressible fluid flow is assumed.

3.2 Numerical Methods for Incompressible Flow Problems

There are many techniques for solving incompressible flow problems. These include the artificial incompressibility method, the stream-function vorticity method, the velocity-vorticity method, the pressure-Poisson method, and projection methods.

The artificial compressibility method is applicable only to the solution of steady state flows (Chorin, 1967). In this approach, an artificial equation of state through a compressibility parameter is introduced. The method is devised such that the steady state solution obtained is independent of the compressibility parameter. This method is valid only for steady flow systems. Since the CVD batch system is unsteady, this method cannot be used.

The streamfunction-vorticity method is usually used for two-dimensional and

axisymmetric flows. There are many references for this method, including Hirsch (1988), White (1979), and Panton (1990). In this approach, the curl of the momentum equations is taken, which eliminates pressure as an unknown. This method reduces the two momentum equations into a single equation in terms of a single component of the vorticity.

The vorticity-velocity formulation has been used to model steady-state, three-dimensional flows. In this approach, the momentum and continuity equations are written in terms of a vector equation of vorticity transport and a Laplacian equation for each velocity component in terms of the vorticity (Ern and Giovangigli, 1995). The advantage of this method is the pressure is eliminated as an unknown. The disadvantages are that additional differential equations on the vorticity must be solved, and that boundary conditions on these equations are determined in terms of the unknown velocity field.

The pressure-Poisson method is useful for constant density steady or unsteady flows. In this approach, the divergence of the momentum equations is taken. The continuity equation is then substituted into this result to yield a Poisson equation on the pressure. The momentum equations and the Poisson equation on the pressure are then solved to obtain the velocity and pressure fields. This method is not as easily implemented in fields with time varying density (Henshaw et al., 1994).

The projection methods are commonly used for steady and unsteady incompressible flows (How and Wetton, 1991; Huang and Wu, 1994; Bell et al., 1994; Majda and Sethian, 1985; Pember et al., 1999). In this method the momentum equations are integrated with the pressure term treated explicitly. The solution to the velocity field does not, in general, satisfy the continuity equation. A projection operator is defined to project the velocity onto the space of vector functions that satisfies the constraint imposed by the continuity equation. In practical application, the projection operator is the Laplacian operator. The solution to this projection is a pressure

correction function. The pressure correction function is then used to compute a velocity correction function. These correction functions are then applied to pressure and velocity to obtain a solutions which are consistent with the continuity equation. Special care must be taken when considering the boundary conditions on the projection operator (Gresho and Sani, 1987; Connell and Stow, 1986; von Schubert, 1995). In some investigations, the projection operator has been simplified and the correction function to pressure and velocity computed iteratively (Patankar, 1980; Kleijn, 1991).

In the present work, a variable density projection method is used. The convective and the diffusive terms are treated implicitly. The pressure correction function is obtained by a variable density projection. The Poisson equation is solved with an iterative solver or direct solvers such as PETSc (Balay et al., 1996) or YALE (Chesshire and Henshaw, 1999).

3.3 Multicomponent Reacting Flow Issues

3.3.1 Numerical Solution of Stiff Systems

The energy and species conservation equations contain convective and transport terms and source terms due to homogeneous and heterogeneous chemical reactions. In many types of reacting flow problems, such as in this work, or combustion, air pollution modeling, etc., the system of these equations may be stiff, mainly due to the chemical reaction source terms. Stiffness implies that there is a vast disparity in the various time scales of the solution, and the use of implicit methods for time integration of such systems is recommended (Press et al., 1992; Sportisse, 2000).

Consider a system of M species with a domain discretized into N cells. A fully implicit numerical method would result in matrices of size $M \times N$, which can be very large. Since the source terms cause the strongest coupling between the species

and energy equation, an operator splitting method is used to reduce the dimension of the matrices.

The species and energy equations create a system of equations of the following form:

$$\frac{d\boldsymbol{z}}{dt} = (\boldsymbol{A} + \boldsymbol{B})\boldsymbol{z}, \quad \boldsymbol{z}(0) = \boldsymbol{z}_0, \tag{3.3}$$

where $\boldsymbol{z}$ is the vector of variables, and $\boldsymbol{A}$ and $\boldsymbol{B}$ are the slow and fast operators, respectively. The fast operator, $\boldsymbol{B}$ is the source of the stiffness. The operator $\boldsymbol{A}$ consists of the diffusive and convective terms.

Consider the first-order (slow-fast) splitting scheme given by

$$\frac{d\boldsymbol{z}^*}{dt} = \boldsymbol{A}\boldsymbol{z}^*, \quad \boldsymbol{z}^*(0) = \boldsymbol{z}_0, \tag{3.4}$$

$$\frac{d\boldsymbol{z}^{**}}{dt} = \boldsymbol{B}\boldsymbol{z}^{**}, \quad \boldsymbol{z}^{**}(0) = \boldsymbol{z}^*(\Delta t), \tag{3.5}$$

where

$$\boldsymbol{z}(\Delta t) = \boldsymbol{z}^{**}(\Delta t) + \mathcal{O}(\Delta t). \tag{3.6}$$

A similar splitting (fast-slow) could be performed by integrating the fast operator first. It is shown in Sportisse (2000) that the (slow-fast) splitting scheme is preferable. Second- and higher-order splittings are also available, with significant costs associated with each. A second-order Strang splitting is significantly more expensive, requiring the evaluation of both the (slow-fast) and (fast-slow) splittings integrated over three time intervals between $t = 0$ and $t = \Delta t$ (Sportisse, 2000).

The splitting results in a slow solve and a fast solve. The spatially coupled slow solve consists of a set of M systems of equations, each with matrix size N. The fast (stiff) solves fully decouple (spatially) and thus form a set of N sets of equations, each with matrix size M. Thus, it is apparent that this splitting has reduced the matrix dimension necessary to simulate the system.

Different solvers are used for the fast and slow solves. The fast solves are computed with the CVODE (Cohen and Hindmarsh, 1994) package. CVODE uses a backwards differentiation formula method, and Jacobians are evaluated by numerical differencing. Other stiff solver methods are given in Press et al. (1992). The slow solves are computed by standard iterative or direct solvers such as YALE and PETSc. These solvers are called directly by OVERTURE member functions. A variety of solver methods and preconditioners are available (Chesshire and Henshaw, 1999).

3.4 Numerical Grid Generation

3.4.1 General Methods

The model describing the CVD batch reactor consists of a set of nonlinear partial differential equations which must are solved on the physical domain representing the interior of the reactor up to. and including, the surfaces of the reactor walls. The numerical solution of these equations requires some discretization of the physical domain into a collection of points or cells. This collection of points is called a grid.

There are three general types of grids used in numerical modeling: structured, unstructured. and hybrid grids. Structured grids consist of points have a structure with respect to the local coordinate system of the physical domain. In unstructured grids, there is no built-in structure. A hybrid grid consists of a collection of structured and unstructured grids in the physical domain. Hybrid grids are also called dragon grids.

There are several types of structured grids used to discretize geometrically complex physical domains: orthogonal, nonorthogonal, patched-block, and overset grids. In the first two categories, a single mesh is used to discretize the entire domain. In some cases, a single orthogonal grid is adequate for this purpose. However, a sin-

gle orthogonal mesh may not be feasible for a very complicated three-dimensional domain. A nonorthogonal mesh introduces additional degrees of freedom for the placement of grid lines, which may be necessary to generate a grid with sufficient quality to obtain an accurate solution. Nonorthogonality of the grid lines introduces complexity in the model with additional geometrical terms (Demirdzic and Peric, 1990; Ferziger and Peric, 1996). The truncation error from the discretization of these geometrical terms can pollute the solution for highly nonorthogonal grids (Ferziger and Peric, 1996).

Patched-block and overset grid generation are two classes of multi-block grid generation methods. The common characteristic of the patched-block methods is that the domain is subdivided into a number of smaller domains (subdomains) which are gridded separately by a set of subgrids. In the patched-block method, the boundaries of the subgrids align exactly. The grid lines in each adjacent subgrid do not necessarily need to align. In the overset grid method, the subgrids overlap each other. The boundaries of each overlapping subgrid are determined by interpolation.

3.4.2 The Overset Grid Method

As just discussed, the overset grid method is a multi-block grid generation method used to discretize domains for the solution of differential equations. There are several advantages for using this technique.

First, it can be used to discretize complex geometries. The subgrids are pieced together in a patchwork that fill the domain and sufficient overlap is required to obtain the required accuracy for interpolation. The patched block method may also be used to generate grids for complex geometries, but the subgrids must align exactly, and this introduces constraints which force the subgrids to become nonorthogonal. Unstructured grids are also often used to model complex geometries, but the resulting coefficient matrices are also unstructured.

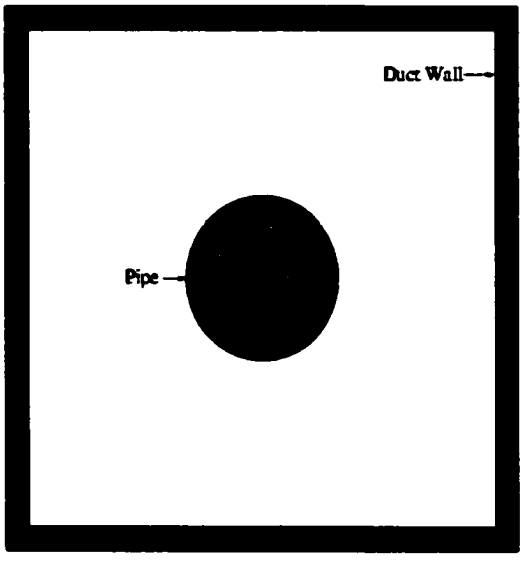

Figure 3.1: Schematic of the cross section of a duct with a square cross section containing a circular pipe at its center.

The overset grid method is also excellent for modeling systems that have moving boundaries, as discussed in Chesshire and Henshaw (1999). However, the CVD systems studied in this work have stationary boundaries.

Lastly, the overset grid method is suited towards implementation on parallel architectures. The processing time for each subgrid could be implemented on a separate processor; hopefully the time spent on communication between processors would make the effort worth it.

3.4.3 Example of an Overset Grid

The overset grid method is now applied to an example of a two-dimensional physical domain. Consider a very long rectangular duct having a square cross section containing a circular pipe at its center. A schematic of this duct is shown in Fig. (3.1). It is desired to solve a differential equation on the domain between the outer surface of the pipe and the inner surface of the duct wall.

An overset grid for the physical domain consisting of the region between the pipe

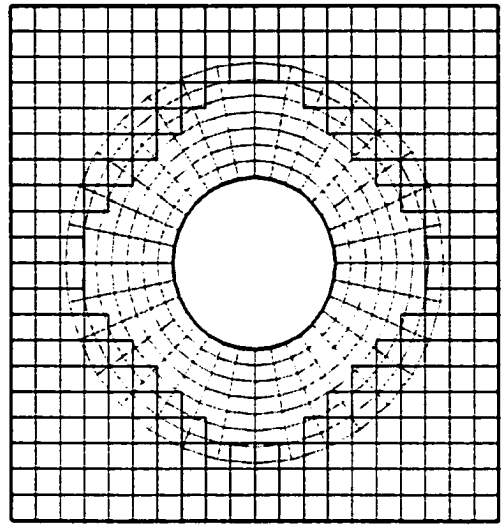

Figure 3.2: An overset grid for the physical domain between the outer wall of the pipe and the inner wall of the rectangular duct shown in Fig. (3.1).

surface and the duct wall is shown in Fig. (3.2). This overset grid, generated with the **ogen** grid generator (Henshaw, 1999a), consists of two orthogonal subgrids. The inner subgrid is an annular grid that maps the domain near the outer surface of the pipe. The background subgrid is Cartesian and maps the region away from the pipe and up to the inner surfaces of the duct wall. The grid points of the subgrids are located at the intersection of the grid lines. Grid points that lie on a boundary are called boundary points. Interior grid points are located in the interior of the domain, but do not lie on the boundary of the subgrids which overlap each other in the interior. The points on the edges of the interior overlapping boundaries are called interpolation points. Ghost points, not shown in the figure, lie outside the physical domain, and are used for numerical computation of boundary conditions.

The numerical model generates an algebraic equation at each point on the grid. The discretization of the differential equation forms an equation that is applied to the discretization (and possibly boundary) points . Boundary conditions form an equation that applies to boundary points (or ghost points if the governing equation

is applied to the boundary points.) Ghost points that are not used are assigned trivial equations. Interpolation equations are applied to each interpolation point. The interpolation equations relate the function value at an interpolation point to the function values of its nearest neighbors on an adjacent subgrid, called interpolee points. As the number of interpolee points increases in the interpolation stencil, so does the accuracy of the interpolation and the required overlap between subgrids.

Another factor that influences grid overlap is the interpolation method. If interpolee points are themselves interpolation points, then the interpolation values are coupled by a sparse system of equations. This is known as implicit interpolation. If the overlap is increased sufficiently, then no interpolee points will be interpolation points, and the interpolation equations for each grid are not coupled. This is known as explicit interpolation. Explicit interpolation simplifies the system of equations, but requires more points in the composite grid. As a comparison, implicitly and explicitly interpolated composite grids are generated for the domain of the previous example. The resulting grids are shown in Fig. (3.3). On the left is the grid generated by implicit interpolation. It contains 507 discretization (and boundary) points and 88 interpolation points. The interpolation points are marked by heavy dots for identification. On the right is the grid generated by explicit interpolation. It contains 588 discretization (and boundary) and 80 interpolation points. Note the difference in the amount of overlap. This amount overlap is consistent with second-order accurate interpolation (Henshaw, 1999a).

There are several factors which motivate the use of overset grids and OVERTURE in this work:

- The ability to discretize complex three-dimensional domains.
- Each subgrid can be orthogonal (or minimally non-orthogonal).
- The OVERTURE class library is built the using A++P++ matrix library

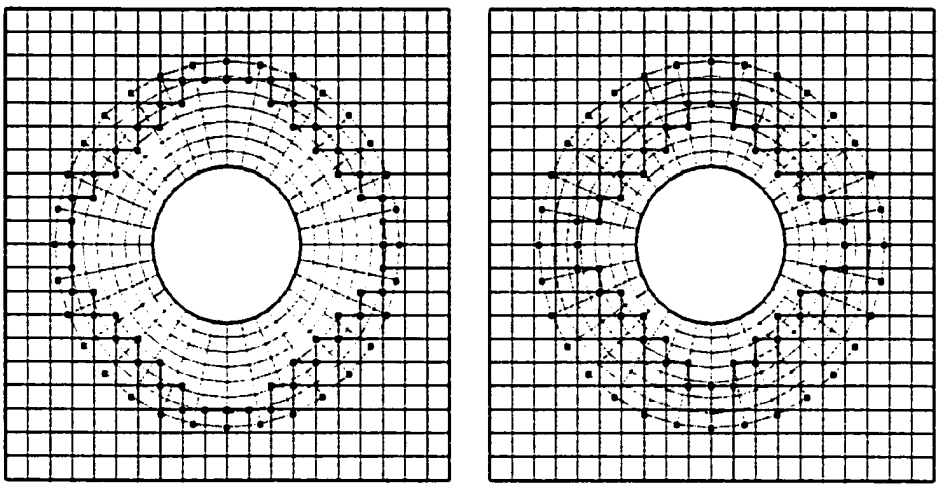

Figure 3.3: A comparison between implicit and explicit interpolation methods used to generate the overset grid for the domain for the region between the outer surface of the circular pipe and the inner surface of the square duct shown in Fig. (3.1). The grid on the left, generated by implicit interpolation, contains 507 discretization and boundary points and 88 interpolation points. The grid on the right, generated by explicit interpolation, contains 563 discretization and boundary points and 80 interpolation points.

(Quinlan, 1999), which is implementable in parallel computing environments.

- The OVERTURE suite performs a large number of tasks needed to solve differential equations on overset grids. The object-oriented nature of this suite of class libraries simplifies the entire code development process.

Finally, it is noted that OVERTURE is an incomplete research tool. Part of the present work involved adding features to the OVERTURE suite which were needed, but not yet implemented. These features included the following:

- Addition of several finite difference operators,
- Classes to link OVERTURE to the CHEMKIN suite,
- Classes to solve the stiff chemical reaction equations.

The finite difference operators added to the OVERTURE suite will be identified in the section on finite difference operators in chapter 5. Details of the class written to link OVERTURE to CHEMKIN are not particularly relevant to this work, since it consists of mechanism to call CHEMKIN functions for various points on a grid. The details relating to the stiff solver are described only in terms of the stiff equations actually being solved. Since CVODE was used for the stiff solver package, the author refers the reader to Cohen and Hindmarsh (1994).

3.5 Introduction to OVERTURE

The OVERTURE framework (Chesshire and Henshaw, 1999) consists of a library of C++ classes for the discretization and solution of partial differential equations on complex domains using overset boundary-fitted curvilinear grids. It also has executable programs for grid generation (Henshaw, 1999a) and visualization (Henshaw, 1999b). The framework is primarily used for finite-difference and finite-volume methods on such grids, although support for other types of grids and methods (such as hybrid grids and finite element methods) may be added in the future.

3.5.1 Grid Generation with OVERTURE

The grid generator **ogen** is used to create overlapping grids that can be used with the OVERTURE class library to solve partial differential equations. An overlapping grid is generated by first defining a collection of **Mappings** that completely fill the physical domain and have a sufficient degree of overlap for the algorithm to succeed. The class **Mapping** is a transformation that maps a portion of the physical space to the unit square (or cube). A **Mapping** can also transform a physical space to another physical space, e.g., a coordinate stretch, rotation, etc. The physical and (to be) interpolated boundaries on the **Mappings** are also identified.

From the list of **Mappings**, individual **Mappings** are selected from lowest to highest priority. The **Mapping** with the lowest priority will have as few points as possible in the final grid. If the overlapping grid algorithm succeeds, a **CompositeGrid** is created. The class **CompositeGrid** contains a collection of objects which define the various components of the overlapping grid including interpolation information. The **CompositeGrid** object also contains arrays to store a large amount of geometric data associated with a grid, but many of these arrays are null by default in order to reduce the size of the data file in which the **CompositeGrid** is saved.

3.5.2 Numerical Solution of Partial Differential Equations with OVERTURE

OVERTURE is designed to solve partial differential equations on overset grids. It is written in object-oriented C++, and its structure simplifies many of the time consuming tasks that arise when writing a code to solve a particular set of PDEs. A complete list of the class definitions, member functions, and inheritance structure can be found in the OVERTURE reference manuals (Chesshire and Henshaw, 1999).

The salient features of OVERTURE are now illustrated by means of an example. Consider the two- or three-dimensional partial differential equation given by

$$\nabla^2 u = 1, \quad u = 2 \text{ (on boundary.)} \tag{3.7}$$

It is desired to solve this with a finite difference method. The system of equations representing the discretization of this differential equation, the boundary conditions, and the interpolation equations is given by

$$\boldsymbol{A}\boldsymbol{u} = \boldsymbol{f}. \tag{3.8}$$

It is assumed that the OVERTURE grid generator **ogen** has been used to create a composite overlapping grid and save it to a file called **fileName**.

In the source code for the executable, the **CompositeGrid** is read from **fileName**:

```
..
  CompositeGrid cg;
  getFromADataBase (fileName, cg);
  cg.update();
..
```

A **CompositeGrid** is instantiated and read from **filename**. The **cg.update()** function is used to compute geometric data for the grid such as cell volumes, etc. A variable u and the coefficient matrix $\boldsymbol{A}$ are represented by **CompositeGridFunctions**. The stencil size of the coefficient matrix depends on the number of dimensions of the **CompositeGrid**:

```
..
  int stencilSize=pow(3,cg.numberOfDimensions())+1;
  realCompositeGridFunction u(cg), A(cg,stencilSize,all,all,all);
..
```

The coefficient matrix representing the finite difference approximation of the Laplacian operator and the boundary conditions is specified by the following:

```
..
  CompositeGridOperators op(cg);
  A = op.laplacianCoefficients();
  A.applyBoundaryConditionCoefficients (0,0, dirichlet, allBoundaries);
  A.applyBoundaryConditionCoefficients (0,0,extrapolate,allBoundaries);
  A.finishBoundaryConditions();
..
```

In the first statement, **CompositeGridOperators op(cg)** defines an object which is used to compute finite differences and finite difference operators for **realCompositeGridFunctions**. The next statement, **A=op.laplacianCoefficients()** computes the coefficients of the Laplacian operator (in 1-, 2-, or 3-D) and copies them into $\boldsymbol{A}$. The next two lines fill in entries to the coefficient matrix corresponding to the boundary conditions. The last line adds entries for interpolation equations, periodic edges, and ghost line corners (which occur at the intersection of ghost lines in 2-D and 3-D grids only).

Now consider, in detail, what occurs in the previous statements. Take for example, a simple, 1-D grid corresponding to the unit line interval with uniform grid

spacing, h, and a single ghost point at each boundary. After `A = op.laplacianCoefficients()` is executed, $\boldsymbol{A}$ is filled in at all interior and boundary points with the discrete approximation to the Laplacian operator, resulting in a (sparse) representation of the coefficient matrix:

$$\boldsymbol{A} = \begin{bmatrix} 0 & 0 & 0 & \dots & & & \\ \frac{1}{h^2} & \frac{-2}{h^2} & \frac{1}{h^2} & 0 & \dots & & \\ 0 & \frac{1}{h^2} & \frac{-2}{h^2} & \frac{1}{h^2} & 0 & \dots & \\ 0 & 0 & \frac{1}{h^2} & \frac{-2}{h^2} & \frac{1}{h^2} & 0 & \\ \vdots & \vdots & & \ddots & \ddots & \ddots & \\ & & & 0 & \frac{1}{h^2} & \frac{-2}{h^2} & \frac{1}{h^2} \\ & & & \dots & 0 & 0 & 0 \end{bmatrix} \begin{array}{ll} i = -1 & \text{(ghost point)} \\ i = 0 & \text{(boundary point)} \\ i = 1 & \text{(interior point)} \\ i = 2 & \text{(interior point)} \\ \vdots & \vdots \\ i = N & \text{(boundary point)} \\ i = N+1 & \text{(ghost point)} \end{array}$$

At this point in time, no equation has been applied at the ghost points, which correspond to the first and last rows of $\boldsymbol{A}$. The boundary conditions of the test problem are applied by `A.applyBoundaryConditionCoefficients(0,0,dirichlet,allBoundaries)`, which replaces the rows corresponding to the boundary points with the identity operator, as follows:

$$\boldsymbol{A} = \begin{bmatrix} 0 & 0 & 0 & \dots & & & \\ 0 & 1 & 0 & 0 & \dots & & \\ 0 & \frac{1}{h^2} & \frac{-2}{h^2} & \frac{1}{h^2} & 0 & \dots & \\ 0 & 0 & \frac{1}{h^2} & \frac{-2}{h^2} & \frac{1}{h^2} & 0 & \\ \vdots & \vdots & & \ddots & \ddots & \ddots & \\ & & & 0 & 0 & 1 & 0 \\ & & & \dots & 0 & 0 & 0 \end{bmatrix} \begin{array}{ll} i = -1 & \text{(ghost point)} \\ i = 0 & \text{(boundary point)} \\ i = 1 & \text{(interior point)} \\ i = 2 & \text{(interior point)} \\ \vdots & \vdots \\ i = N & \text{(boundary point)} \\ i = N+1 & \text{(ghost point)} \end{array} \tag{3.9}$$

Extrapolation equations are applied to the ghost point rows using `A.applyBoundaryConditionCoefficients(0,0,extrapolate,allBoundaries)`. The coefficient matrix is now given by

$$\boldsymbol{A} = \begin{bmatrix} 1 & -3 & 3 & -1 & 0 & \dots & \\ 0 & 1 & 0 & 0 & \dots & & \\ 0 & \frac{1}{h^2} & \frac{-2}{h^2} & \frac{1}{h^2} & 0 & \dots & \\ 0 & 0 & \frac{1}{h^2} & \frac{-2}{h^2} & \frac{1}{h^2} & 0 & \\ \vdots & \vdots & & \ddots & \ddots & \ddots & \\ & & & 0 & 0 & 1 & 0 \\ & \dots & 0 & -1 & 3 & -3 & 1 \end{bmatrix} \begin{array}{ll} i = -1 & \text{(ghost point)} \\ i = 0 & \text{(boundary point)} \\ i = 1 & \text{(interior point)} \\ i = 2 & \text{(interior point)} \\ \vdots & \vdots \\ i = N & \text{(boundary point)} \\ i = N+1 & \text{(ghost point)} \end{array} \tag{3.10}$$

The last statement, `A.finishBoundaryConditions()`, is used to supply interpolation equation coefficients, and extrapolation coefficients at ghost line corners. In this simple example, no interpolation points or ghost line points are present.

Next, an **Oges** object is created, which is used to solve the system of equations. The **Oges** class contains information about which software package, i.e., YALE, HARWELL, etc., is used to solved the equation system; the type of preconditioner used (if any); convergence criteria; and other information (Henshaw, 1999a).

```
..
  Oges solver( cg );
..
```

The **Oges** requires specification of the coefficient matrix. This is done by the statement

```
..
  solver.setCoefficientArray( A );
..
```

Now that the left-hand side is completely specified, it is necessary to fill in the right-hand side at all points. For the Dirichlet boundary condition test problem, the right-hand side of the differential equation is filled in at all interior points. The boundary points are filled in with the values corresponding to the boundary conditions. By default, **Oges** fills in zero values at extrapolation and interpolation points. The statements used to fill in the right-hand side for the test problem are as follows:

```
..
  // ASSIGN THE RIGHT-HAND SIDE:  Laplacian u = 1; (u = 2  on boundary)
  for( int grid=0; grid<cg.numberOfComponentGrids(); grid++ )
  {
    getIndex(cg[grid].indexRange(),I1,I2,I3);

    // INTERIOR POINTS
    f[grid](I1,I2,I3) = 1.;

    // BOUNDARY POINTS
    for( int side=Start; side<=End; side++ )
    for( int axis=axis1; axis<cg.numberOfDimensions(); axis++ )
    {
      if( cg[grid].boundaryCondition()(side,axis) > 0 )
```

```
    {
      getBoundaryIndex(cg[grid].indexRange(),side,axis,Ib1,Ib2,Ib3);
      f[grid](Ib1,Ib2,Ib3) = 2.;
    }
  }
}
..
```

The complete linear system which represents the finite difference approximation to the test problem is thus

$$\begin{bmatrix} 1 & -3 & 3 & -1 & 0 & \dots & \\ 0 & 1 & 0 & 0 & \dots & & \\ 0 & \frac{1}{h^2} & \frac{-2}{h^2} & \frac{1}{h^2} & 0 & \dots & \\ 0 & 0 & \frac{1}{h^2} & \frac{-2}{h^2} & \frac{1}{h^2} & 0 & \\ \vdots & \vdots & & \ddots & \ddots & \ddots & \\ & & & 0 & 0 & 1 & 0 \\ & \dots & 0 & -1 & 3 & -3 & 1 \end{bmatrix} \begin{Bmatrix} u_{-1} \\ u_0 \\ u_1 \\ u_2 \\ \vdots \\ u_N \\ u_{N+1} \end{Bmatrix} = \begin{Bmatrix} 0 \\ 2 \\ 1 \\ 1 \\ \vdots \\ 2 \\ 0 \end{Bmatrix} \tag{3.11}$$

The solution, u, is obtained by the statement

```
..
  solver.solve(u, f);
..
```

In this example, it is clear that the C++ classes are doing a lot of computations "behind the scenes." These computations are built in to the class definitions, and are intended to streamline the process of code design. Details of the computations, such as interpolation, are not intended to be manipulated directly by the user, and are thus hidden. Note that in these sets of code snippets there was no reference to how interpolation is being done. The default interpolation is based on the amount of overlap in the grids. It is assumed, by default, that there must be enough overlap for implementation of second-order interpolation equations. If higher-order interpolation is specified (in the grid generation process), then that information will be included in the **CompositeGrid**, and interpolation equations will be constructed at higher-order. Of course, the order of the interpolation is dependent on the amount of overlap. The OVERTURE user manuals contain a great deal more information regarding the

details of the classes; including, member variables, member functions, inheritance, etc. (Chesshire and Henshaw, 1999).

Chapter 4

DIMENSIONAL ANALYSIS

In this chapter, a dimensional analysis is performed on the governing equations of the model presented in chapter 2. The purpose of dimensional analysis in this work is to gain insight as to which terms in the governing equations, under which circumstances, might be considered negligible and make the equations easier to solve. Dimensional analysis is a technique in which each of the variables and parameters in an equation is normalized with respect to a characteristic value, or scaling factor, of that variable or parameter. The scaling factors are chosen such that the normalized variables are order of magnitude unity. The scaling factors are collected together to form dimensionless groups. The magnitudes of these dimensionless groups then serve as parameters which govern the basic nature of the equation.

4.1 The Momentum Equation

The dimensional analysis of the momentum equation cannot begin until the nature of the flow inside a CVD batch reactor is better understood.

In a CVD batch reactor, there are no gas inlets or outlets, and the temperature distribution inside the reactor may not be uniform. Through the ideal gas law, the density distribution may be variable as well. Variations in the density field may induce fluid motion. In other words, the flow inside a CVD batch reactor is driven by natural convection.

Recalling the momentum equation, Eq. (2.46),

$$\rho\left(\frac{\partial \boldsymbol{u}}{\partial t}+\boldsymbol{u}\cdot\boldsymbol{\nabla}\boldsymbol{u}\right)+\boldsymbol{\nabla}p=\rho\boldsymbol{g}+\boldsymbol{\nabla}\cdot\left(\mu\left(\boldsymbol{\nabla}\boldsymbol{u}+\boldsymbol{\nabla}\boldsymbol{u}^{T}\right)-\frac{2}{3}\mu\left(\boldsymbol{\nabla}\cdot\boldsymbol{u}\right)\boldsymbol{I}\right). \quad (4.1)$$

Note that density differences do not appear. However, there is a component to the pressure field which balances gravitational forces exactly in the absence of motion. This is called the static pressure field, p_s. The static pressure field is the solution to

$$\nabla p_s = \rho_s \boldsymbol{g}, \tag{4.2}$$

where ρ_s is the density field in the static fluid field. It is not necessarily the same as ρ. Subtracting Eq. (4.2) from Eq. (4.1) yields the dynamic momentum equation, which clearly shows how density variations in the fluid field influence motion. Defining $\tilde{\rho} \equiv \rho - \rho_s$, the dynamic equation is as follows:

$$\rho\left(\frac{\partial \boldsymbol{u}}{\partial t} + \boldsymbol{u}\cdot\nabla\boldsymbol{u}\right) + \nabla p_d = \tilde{\rho}\boldsymbol{g} + \nabla\cdot\left(\mu\left(\nabla\boldsymbol{u} + \nabla\boldsymbol{u}^T\right) - \frac{2}{3}\mu\left(\nabla\cdot\boldsymbol{u}\right)\boldsymbol{I}\right), \tag{4.3}$$

where p_d is the dynamic pressure defined by

$$\nabla p \equiv \nabla p_d + \nabla p_s. \tag{4.4}$$

The following characteristic quantities are used for the normalization of the various terms appearing in the momentum equation:

$$\rho^* \equiv \rho/\rho_c, \qquad \mu^* \equiv \mu/\mu_c,$$
$$\tilde{\rho}^* \equiv \tilde{\rho}/\Delta_c\rho, \qquad p_d^* \equiv p_d/\Delta_c p,$$
$$\boldsymbol{u}^* \equiv \boldsymbol{u}/u_c, \qquad \nabla^* \equiv l_c\nabla,$$
$$t^* \equiv tu_c/l_c, \qquad \boldsymbol{e_g} \equiv \boldsymbol{g}/g.$$

The quantities with $*$ superscripts are dimensionless. Terms with c subscripts are characteristic of the behavior of the system. The characteristic density and viscosity are chosen from some reference state, perhaps the initial condition. Δ_c scalings refer to a characteristic change of that quantity in the system. This distinction is made for the pressure and density terms because they do not vary from zero to some characteristic value. They vary slightly about some mean characteristic

value. The velocity, on the other hand, varies from zero at all non-reacting walls to some maximum value in the reactor. Thus the characteristic value of velocity is also characteristic of the change in velocity. As in other natural convection flows, there is no directly obvious choice for the characteristic velocity. There is also no obvious choice for the characteristic length; note that the characteristic length is not necessarily the length of the reactor! It is the distance over which the velocity changes from minimum to maximum. It is assumed that characteristic time is equal to the ratio of the characteristic length of the flowfield and the characteristic velocity.

Even though the characteristic length, velocity, or pressure variation is not precisely known, it is assumed that the scalings presented above are perfectly valid. Making the appropriate substitutions yields the following:

$$\left(\frac{\rho_c u_c^2}{l_c}\right)\rho^*\frac{D^*\boldsymbol{u}^*}{D^*t^*}+\left(\frac{\Delta_c p}{l_c}\right)\boldsymbol{\nabla}^* p_d^*=(\Delta_c\rho g)\,\tilde{\rho}^*\boldsymbol{e}_g+\left(\frac{\mu_c u_c}{l_c^2}\right)\boldsymbol{\nabla}^*\cdot\boldsymbol{T}^*, \tag{4.5}$$

where

$$\frac{D^*\boldsymbol{u}^*}{D^*t^*}=\frac{\partial\boldsymbol{u}^*}{\partial t^*}+\boldsymbol{u}^*\cdot\boldsymbol{\nabla}^*\boldsymbol{u}^*$$

$$\boldsymbol{T}^*=\mu^*\left(\boldsymbol{\nabla}^*\boldsymbol{u}^*+\boldsymbol{\nabla}^*\boldsymbol{u}^{*T}\right)-\frac{2}{3}\mu^*\left(\boldsymbol{\nabla}^*\cdot\boldsymbol{u}^*\right)\boldsymbol{I}.$$

At this point, a few assumptions are made regarding some of the characteristic quantities. Since buoyancy is the responsible for the fluid motion, it must be as large as any of the other terms in the equation. Dividing the momentum equation by the characteristic buoyancy terms yields

$$\left(\frac{\rho_c u_c^2}{\Delta_c\rho g l_c}\right)\rho^*\frac{D^*\boldsymbol{u}^*}{D^*t^*}+\left(\frac{\Delta_c p}{\Delta_c\rho g l_c}\right)\boldsymbol{\nabla}^* p_d^*=\tilde{\rho}^*\boldsymbol{e}_g+\left(\frac{\mu_c u_c}{\Delta_c\rho g l_c^2}\right)\boldsymbol{\nabla}^*\cdot\boldsymbol{T}^*. \tag{4.6}$$

It is assumed that the characteristic pressure term (in parentheses) is of the same order of magnitude as either the characteristic convective or stress terms. If the former is assumed, then

$$\left(\frac{\rho_c u_c^2}{\Delta_c\rho g l_c}\right)\left(\rho^*\frac{D^*\boldsymbol{u}^*}{D^*t^*}+\boldsymbol{\nabla}^* p_d^*\right)=\tilde{\rho}^*\boldsymbol{e}_g+\left(\frac{\mu_c u_c}{\Delta_c\rho g l_c^2}\right)\boldsymbol{\nabla}^*\cdot\boldsymbol{T}^*. \tag{4.7}$$

The quantities in parentheses are dimensionless groups. However, they include the characteristic velocity, which is unknown. If it is assumed that the convective (and pressure) term is of the same order as the buoyancy term, then

$$\frac{\rho_c u_c^2}{\Delta_c \rho g l_c} \approx \mathcal{O}(1). \tag{4.8}$$

Solving this equation for u_c and substituting the result into Eq. (4.7) yields

$$\rho^* \frac{D^* \boldsymbol{u}^*}{D^* t^*} + \boldsymbol{\nabla}^* p_d^* = \tilde{\rho}^* \boldsymbol{e}_g + \frac{1}{\sqrt{\mathsf{Gr}}} \boldsymbol{\nabla}^* \cdot \boldsymbol{T}^*, \tag{4.9}$$

where Gr is the Grashof number defined by

$$\mathsf{Gr} \equiv \frac{\rho g \Delta_c \rho l_c^3}{\mu_c^2}. \tag{4.10}$$

The scaling given by Eq. (4.9) is appropriate for large Grashof numbers, since the stress term cannot be larger than the buoyancy term.

The scaling appropriate for low Grashof numbers is obtained by assuming the characteristic pressure term is on the same order as the stress term. In this case,

$$\left(\frac{\rho_c u_c^2}{\Delta_c \rho g l_c}\right) \rho^* \frac{D^* \boldsymbol{u}^*}{D^* t^*} = \tilde{\rho}^* \boldsymbol{e}_g + \left(\frac{\mu_c u_c}{\Delta_c \rho g l_c^2}\right) (\boldsymbol{\nabla}^* \cdot \boldsymbol{T}^* - \boldsymbol{\nabla}^* p_d^*). \tag{4.11}$$

If it is assumed that the stress (and pressure) term is of the same order as buoyancy, then the characteristic velocity can be eliminated from the momentum equation to yield the following:

$$\mathsf{Gr}\, \rho^* \frac{D^* \boldsymbol{u}^*}{D^* t^*} = \tilde{\rho}^* \boldsymbol{e}_g + \boldsymbol{\nabla}^* \cdot \boldsymbol{T}^* - \boldsymbol{\nabla}^* p_d^*. \tag{4.12}$$

For moderate values of the Grashof number, neither Eq. (4.9) nor Eq. (4.12) is appropriate. The dimensionless equation reduces to the original dynamic momentum equation given by Eq. (4.3), with all quantities in dimensionless form. The magnitude of the Grashof number depends on quantities that are known for a given CVD batch system, *except* for the characteristic length. Since l_c is unknown, the Grashof number is also unknown. However, the dimensional analysis was not done in vain. For a

given problem, the fully dimensional form of the equations can be solved for the flowfield. From the solution, the characteristic length may be determined directly, and from this, the Grashof number may be computed. If the magnitude of the Grashof number corresponds to one of the above cases — high or low Grashof number — then subsequent computations may be modified (simplified) by this additional information.

4.2 Static Pressure

The static pressure equation is given by

$$\nabla p_s = \rho_s \boldsymbol{g}. \tag{4.13}$$

If $p_s \gg p_d$, then

$$\nabla p \cong \rho_s \boldsymbol{g}. \tag{4.14}$$

Since, $p = \rho_s R\theta$, and $\boldsymbol{g} = -g\boldsymbol{e}_z$, the z-component of this equation is

$$\frac{d}{dz} \ln p = -\frac{g}{R\theta}. \tag{4.15}$$

Assuming the temperature is constant, this equation may be integrated to yield

$$p = p_0 \exp\left(-\frac{gz}{R\theta}\right), \tag{4.16}$$

where p_0 is the pressure at $z = 0$. For small values of the argument $gz/R\theta$, the exponential term can be expanded in a Taylor series. Truncating the series after the second term yields the following:

$$p = p_0 \left(1 - \frac{gz}{R\theta}\right). \tag{4.17}$$

The pressure field consists of a spatially constant pressure and a linearly varying field. The spatially constant term p_0 is called the background pressure.

The magnitude of the background pressure is equal to the pressure consistent with the ideal gas law for the entire reactor. That is,

$$p_0 V = mR\theta, \tag{4.18}$$

where V is the total volume of the reactor. This is proven by integrating the density over the volume:

$$m = \int_V \rho_s \, dV.$$

Assuming a constant temperature and constant cross-sectional area, A, this equation may be integrated to yield

$$m = \frac{p_0 A}{g}\left[1 - \exp\left(-\frac{gH}{R\theta}\right)\right], \tag{4.19}$$

Expanding the exponential in a Taylor series and truncating all terms higher than second order yields

$$m = \frac{p_o AH}{R\theta}, \tag{4.20}$$

which is the same as Eq. (4.18), since $V = AH$.

The magnitude of the background pressure is usually several orders of magnitude greater than the linear variation in the static pressure. Consider a CVD reactor with height 10 cm containing a binary mixture of WF_6 and H_2 at 300 K and 1 Torr, each species equally present in terms of moles. The mean molecular weight of the mixture is 150 $\mathrm{g\,mol^{-2}}$. The change in the static pressure is given by $p_0 gH\tilde{w}/\mathcal{R}\theta$, or 5.9×10^{-5} Torr. Hence, whenever the pressure is needed for computation of the thermophysical quantities, the background pressure is used.

4.3 The Divergence of Velocity

The continuity equation is used to appropriately scale the divergence of velocity, which appears in the energy equation. In dimensional form, the continuity equation

is given by

$$\nabla \cdot \boldsymbol{u} = -\frac{1}{\rho}\frac{D\rho}{Dt}, \tag{4.21}$$

One might choose u_c/l_c for the scaling of the divergence of velocity. However, if the flow were constant density, then the divergence would be identically zero, from the right-hand side of the equation. A better scaling for local the divergence is based on the characteristic value of $(1/\rho)D\rho/Dt$. Using the ideal gas law and the chain rule,

$$\frac{1}{\rho}\frac{D\rho}{Dt} = \frac{1}{p}\frac{Dp}{Dt} - \frac{1}{\theta}\frac{D\theta}{Dt} + \frac{1}{\tilde{w}}\frac{D\tilde{w}}{Dt}. \tag{4.22}$$

The last term on the right-hand side, which results from the change in the composition field, is considered negligible. The dimensionless form of this equation may be given as follows:

$$\frac{1}{\rho}\frac{D\rho}{Dt} = \frac{u_c}{l_c}\left(\frac{\Delta_c p}{\rho_c c_{vc}\theta_c}\frac{1}{p^*}\frac{D^*p^*}{D^*t^*} - \frac{\Delta_c\theta}{\theta_c}\frac{1}{\theta^*}\frac{D^*\theta^*}{D^*t^*}\right), \tag{4.23}$$

where

$$\Delta^*p^* \equiv \Delta p/\Delta_c p,$$

$$p^* \equiv p/\rho_c c_{vc}\theta_c,$$

$$\Delta^*\theta^* \equiv \Delta\theta/\Delta_c\theta,$$

$$\theta^* \equiv \theta/\theta_c.$$

Note that the use of c_{vc} in the scaling of the pressure is acceptable since $c_v = \mathcal{O}(R)$ for an ideal gas.

The pressure term is negligible, because the ratio $\Delta_c\theta/\theta_c$ may be order unity, while $\Delta_c p/\rho_c c_{vc}\theta_c \ll 1$. Thus,

$$\nabla^* \cdot \boldsymbol{u}^* = \left(\frac{l_c\theta_c}{u_c\Delta_c\theta}\right)\nabla \cdot \boldsymbol{u} \tag{4.24}$$

The divergence can also be scaled on a global average basis. The volume average of the divergence is given by

$$\overline{\nabla \cdot \boldsymbol{u}} = \frac{1}{V}\int_V \nabla \cdot \boldsymbol{u}\, dV. \tag{4.25}$$

Using Stokes' theorem,

$$\overline{\nabla \cdot \boldsymbol{u}} = \frac{1}{V}\int_A \boldsymbol{u} \cdot \boldsymbol{n}\, dA, \tag{4.26}$$

where the boundary velocities are computed from the reaction rates by

$$\boldsymbol{u} \cdot \boldsymbol{n} = -\frac{1}{\rho}\sum_m \sigma_m \quad \text{(on boundary)}. \tag{4.27}$$

Thus, an appropriate scaling for the global divergence is given by

$$\overline{\nabla^* \cdot \boldsymbol{u}^*} \equiv \left(\frac{A_c \sigma_c}{\rho_c V_c}\right) \overline{\nabla \cdot \boldsymbol{u}}. \tag{4.28}$$

where A_c is the characteristic surface area of the reacting walls, V_c is the volume of the reactor, and σ_c is a characteristic reaction rate for the gas species due to heterogeneous reaction. The term in parentheses is the ratio of the mass flow rate out of the gas phase (and being deposited by heterogeneous chemical reaction) and the total mass in the reactor. Thus, if there are no surface reactions, the global divergence is zero.

In the momentum equation, part of the stress tensor contains the divergence of velocity. This term could be rescaled by the local or the global divergence as given in this section; however, this is probably not necessary since the divergence term in the stress tensor is generally smaller than the velocity gradient terms.

4.4 The Species Continuity Equations

The species continuity equations are normalized using the following scalings:

$$t^* \equiv tD_c/l_c^2,$$

$$\boldsymbol{j}_m^* \equiv \boldsymbol{j}_m l_c/\rho_c D_c,$$

$$r_m^* \equiv r_m/r_c,$$

where D_c is a characteristic diffusion coefficient, and r_c is a characteristic reaction rate due to homogeneous kinetics. It is assumed that the characteristic time is based on a scale related to mass diffusion.

As with the momentum equations, there are two possible scalings for the characteristic velocity, consistent with either a low or high Grashof number limit. The characteristic velocity in the high Grashof number limit is given by

$$u_c = \sqrt{\frac{\Delta_c \rho g l_c}{\rho_c}}. \tag{4.29}$$

Making the appropriate substitutions,

$$\frac{\partial \rho^* y_m}{\partial t^*} + \sqrt{\mathsf{Gr}}\mathsf{Sc}\,\nabla \cdot (\rho \boldsymbol{u} y_m) + \nabla \cdot \boldsymbol{j}_m^* = \mathsf{Da}\, r_m^* \quad (m = 1, 2, \ldots, M). \tag{4.30}$$

where Sc is the Schmidt number and Da is the homogeneous reaction Damköhler number defined by

$$\mathsf{Sc} \equiv \frac{\mu_c}{\rho_c D_c}, \tag{4.31}$$

$$\mathsf{Da} \equiv \frac{r_c l_c^2}{\rho_c D_c}. \tag{4.32}$$

The characteristic velocity in the low Grashof number limit is given by

$$u_c = \frac{\Delta_c \rho g l_c^2}{\mu_c}. \tag{4.33}$$

and the resulting dimensionless equation is

$$\frac{\partial \rho^* y_m}{\partial t^*} + \mathsf{GrSc}\,\nabla \cdot (\rho \boldsymbol{u} y_m) + \nabla \cdot \boldsymbol{j}_m^* = \mathsf{Da}\, r_m^* \quad (m = 1, 2, \ldots, M). \tag{4.34}$$

4.5 The Energy Equation

The energy equation is normalized with the following scalings:

$$t^* \equiv k_c t/\rho_c c_{vc} l_c^2, \qquad c_v^* \equiv c_v/c_{vc},$$

$$\Delta^*\theta^* \equiv \Delta\theta/\Delta_c\theta, \qquad p^* \equiv p/\rho_c c_{vc}\theta_c,$$

$$c_{p_m}^* \equiv c_{p_m}/c_{vc}, \qquad \nabla^* \cdot \boldsymbol{u}^* \equiv (l_c\theta_c/u_c\Delta_c\theta)\,\nabla \cdot \boldsymbol{u},$$

$$R_m^* \equiv R_m/c_{vc}, \qquad R^* \equiv R/c_{vc},$$

$$e_m^* \equiv e_m/e_c, \qquad k^* \equiv k/k_c,$$

where k_c is a characteristic thermal conductivity, c_{vc} is the characteristic specific heat, and e_c is the characteristic specific internal energy.

As with the momentum equations, there are two possible scalings for the characteristic velocity, consistent with either a low or high Grashof number limit. The dimensionless energy equation for high Grashof numbers is given by

$$\rho^* c_v^* \frac{\partial\theta^*}{\partial t^*} + \sqrt{\mathsf{Gr}}\mathsf{Pr}\,(\rho^* c_v^* \boldsymbol{u}^* \cdot \nabla^*\theta^* + p^*\nabla^* \cdot \boldsymbol{u}^*) = \nabla^* \cdot (k^*\nabla^*\theta^*)$$
$$- \mathsf{E}\sum_{m=1}^{M} e_m^* r_m^* - \frac{\mathsf{Pr}}{\mathsf{Sc}}\sum_{m=1}^{M}\left(c_{p_m}^* \boldsymbol{j}_m^* \cdot \nabla^*\theta^* + \frac{1}{\mathsf{Ga}} R_m^*\theta^*\nabla^* \cdot \boldsymbol{j}_m^*\right), \quad (4.35)$$

where Pr is the Prandtl number, E is the Energy Generation number, and Ga is the Gay-Lussac number defined by

$$\mathsf{Pr} = \mu_c c_{vc}/k_c, \quad (4.36)$$

$$\mathsf{E} = e_c r_c l_c^2/k_c\Delta_c\theta, \quad (4.37)$$

$$\mathsf{Ga} = \Delta_c\theta/\theta_c. \quad (4.38)$$

The dimensionless energy equation for the low Grashof number limit is

$$\rho^* c_v^* \frac{\partial\theta^*}{\partial t^*} + \mathsf{GrPr}\,(\rho^* c_v^* \boldsymbol{u}^* \cdot \nabla^*\theta^* + p^*\nabla^* \cdot \boldsymbol{u}^*) = \nabla^* \cdot (k^*\nabla^*\theta^*)$$
$$- \mathsf{E}\sum_{m=1}^{M} e_m^* r_m^* - \frac{\mathsf{Pr}}{\mathsf{Sc}}\sum_{m=1}^{M}\left(c_{p_m}^* \boldsymbol{j}_m^* \cdot \nabla^*\theta^* + \frac{1}{\mathsf{Ga}} R_m^*\theta^*\nabla^* \cdot \boldsymbol{j}_m^*\right), \quad (4.39)$$

4.6 Closure

The behavior of the momentum equation in the closed batch system is governed by a single dimensionless group, the Grashof number. Unfortunately, the Grashof number cannot be computed directly from the geometry and operating conditions of the system because the characteristic length of the flow field is not known. The characteristic length is not necessarily the length of the reactor, although one could assume that it is a reasonable choice. If one did choose to use the length of the reactor as the characteristic length, and this choice was in error by an order of magnitude, then the computed Grashof number would be in error by three orders of magnitude. If it were decided to ignore terms based on the magnitude of such an inappropriately computed dimensionless group could render the solution meaningless. Instead of choosing a length scale based on convenience, the appropriate procedure in this case is to solve the equations in dimensional form for a given system and measure the characteristic length from the solution. From this measurement, the Grashof number can be rigorously computed, and appropriate simplifications can be made when performing subsequent computations. As an example, consider the flow field in a CVD system at very low pressure. Suppose that, as measured from the computed flow field, the quantities $GrSc$ and $GrPr$ are both much less than unity. Under these conditions, the convective terms in the energy and species equations could be neglected. Thus, in all subsequent computations, the momentum equation would not need to be solved at all.

The source term in the species continuity equation is controlled by the magnitude of the gas phase Damköhler number, Da, which is representative of the ratio of gas phase reaction rate to the mass diffusion rate. Due to the large variability in reaction and diffusion rates, the magnitude of the Damköhler number is also highly variable.

The source terms in the energy equation are controlled by the Energy Generation number, E, and the ratio of the Prandtl number to the Schmidt number, also known

as the Lewis number, Le. The Energy Generation number is the ratio of the energy released by gas phase chemical reaction to the energy transport due to conduction. Due to the variability in the reaction rates and magnitudes of the energy of formation of the species, E is also highly variable. The ratio of the Prandtl number and the Schmidt number is typically order unity for gases.

Chapter 5

THE NUMERICAL METHOD

5.1 Introduction

In this chapter, the implementation of the numerical solution strategy for the model is discussed.

First, a summary of the steps of the numerical method is presented. In the next section, temporal discretization of the differential equations is discussed. The energy and species equations are solved with a slow-fast splitting technique as discussed in Sportisse (2000) to handle the stiffness arising from the chemical reaction terms. The fast solves are performed with the CVODEstiff differential equation solver for dense systems. The slow solve contains the convective and diffusive terms. The diffusion term is solved with a diagonally implicit approach. The convective terms are also treated implicitly. The off-diagonal terms in the diffusion matrix are treated explicitly.

In the next section, the discretization of the momentum equation is presented. The momentum equation is solved with a variable density projection method. In this approach, the momentum equations are integrated. The resulting velocity field will not, in general, satisfy continuity. A Poisson equation is solved for a function which projects the velocity onto the space of functions that satisfies the constraint imposed by the continuity.

Next, the spatial discretization of several of the finite difference operators is discussed, such as the divergence, Laplacian, and $\nabla \cdot (s\nabla)$ operators, where s is a scalar function. All operators are computed using conservative finite differences in two- and three-dimensional curvilinear coordinates.

5.2 Numerical discretization

5.2.1 Notation

The time level of variables is indicated by a superscript. That is,

$$p^0 = p(\boldsymbol{x}, t = 0) \tag{5.1}$$

represents the pressure at time zero. As the solution is integrated to the next time step, Δt_1,

$$p^1 = p(\boldsymbol{x}, t = \Delta t_1). \tag{5.2}$$

The next time interval for the integration may be different than Δt_1. In general we refer to the time step for the ith integration step as Δt_i. Then

$$p^n = p(\boldsymbol{x}, t = \sum_{i=1}^{n} \Delta t_i). \tag{5.3}$$

5.3 Summary of the Numerical Method

A flowchart of the CVD batch solver numerical procedure is shown in Fig. (5.1). A summary of the steps are as follows:

1. The initial conditions on velocity, temperature, background pressure, gas phase mass fractions, and site fractions are specified.

2. Thermodynamic and transport properties are computed.

3. A first-order splitting is used on the species-energy system.

   The fast part of the species and energy equations are solved on the interior and boundary nodes.

   The Stefan velocity and bulk deposition at reactive surfaces are computed.

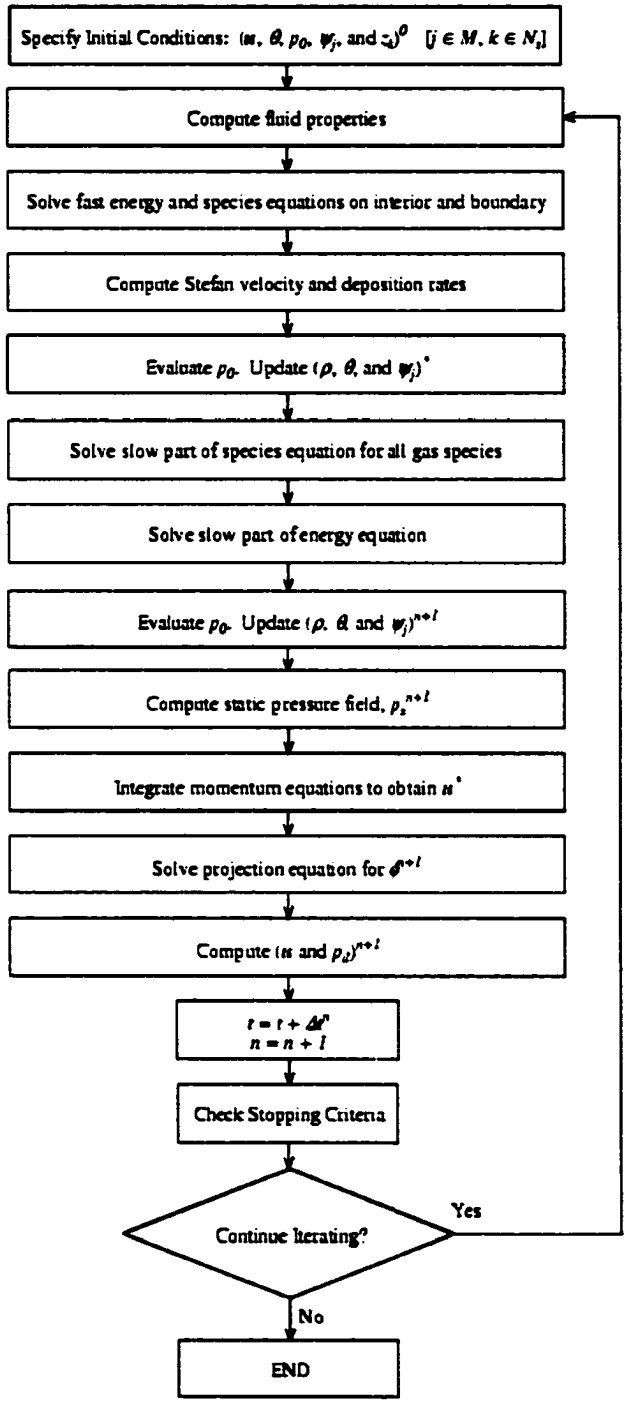

Figure 5.1: Flowchart of computations performed by the CVD batch solver.

The background pressure is computed to adjust for changes in gas composition and temperature.

The slow part of the species and energy equations are solved on the interior and boundary nodes.

The background pressure is again computed to adjust for changes in gas composition and temperature. p_o^{n+1}, θ^{n+1}, ρ^{n+1}, and ψ_m^{n+1} are now known.

4. The static pressure field is computed.

5. Each component of the momentum equation is integrated to obtain $\boldsymbol{u}^*$.

6. A variable-density projection to enforce continuity on a global basis.

7. The velocity and dynamic pressure are then computed to obtain $\boldsymbol{u}^{n+1}$ and p_d^{n+1}.

8. Stopping criteria are checked. If not satisfied, return to step (2). Otherwise stop.

5.3.1 Initialization

The initial conditions for the system completely specify the state of the gas in the reactor and the site fractions of surface species on all reactive surfaces. The initial conditions for the gas phase are specified by the pressure, temperature, and mass (or mole) fractions. The surface site fractions may be arbitrarily guessed, but it was found that that estimating the site fractions from an equilibrium computation of the surface species with a known surface temperature, pressure, and gas phase composition, with a code such as SURFKIN (Coltrin et al., 2000), yielded improved convergence of the solver. The density, viscosity, and other remaining fluid properties are then computed. The initial fluid velocity is zero.

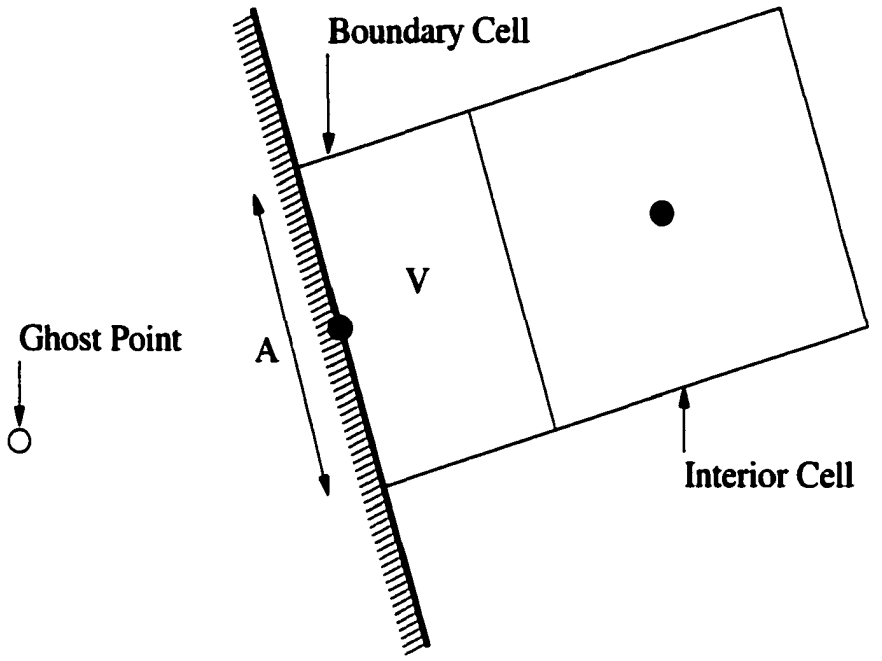

Figure 5.2: Schematic representation of a boundary and interior node.

5.3.2 The Species and Energy Equation Stiff-Splitting

The species and energy equations form a coupled system of equations that can be represented by the following equation:

$$\frac{\partial \boldsymbol{z}}{\partial t} = \boldsymbol{A}\boldsymbol{z} + \boldsymbol{B}\boldsymbol{z}. \tag{5.4}$$

The vector $\boldsymbol{z}$ is defined differently for interior and boundary nodes. A schematic of the grid near the reactor surface is shown in Fig. (5.2). In this figure the control volumes are shown for a boundary node and an adjacent interior node. On the interior node, all chemical reactions are homogeneous. On the surface node, gas phase reactions can occur throughout the cell volume, V, and surface reactions may cause a flux of gas species at the surface, which has area A. The site fractions of the surface species and mass bulk species deposited by CVD is also stored at the boundary node. The stiff equations at the surface node include the homogeneous reactions in the gas cell, and the conservation equations for the site fractions of the

surface species.

Consider each of the following systems of equations: (1) the fast species and energy equations in the interior, (2) the fast species and energy equations on the boundary, (3) the slow (non-stiff) species equations in the interior and on the boundary, and (4) the slow energy equation in the interior and on the boundary.

The Fast Part of the Species and Energy Equations in the Interior

At the interior nodes, the fast part of the species equation is

$$\frac{\partial \rho \psi_m}{\partial t} = r_m, \tag{5.5}$$

or

$$\rho \frac{\partial \psi_m}{\partial t} + y_m \frac{\partial \rho}{\partial t} = r_m. \tag{5.6}$$

Summing the the species equations and using $\sum_m r_m = 0$ yields

$$\frac{\partial \rho}{\partial t} = 0. \tag{5.7}$$

Substituting this result into Eq. (5.6) yields

$$\frac{\partial \psi_m}{\partial t} = \frac{r_m}{\rho} \qquad (m = 1, 2, \ldots, M). \tag{5.8}$$

The fast part of the energy equation is

$$\frac{\partial \theta}{\partial t} = -\frac{1}{\rho c_v} \sum_m e_m r_m. \tag{5.9}$$

Hence, the fast equation system at interior nodes is given by Eqns. (5.7), (5.8), and (5.9).

The Fast Part of the Species and Energy Equations on the Boundary

The fast part of the species equation at the boundary cells is derived by rewriting the species continuity equation in integral form:

$$\int_V \left(\frac{\partial \rho \psi_m}{\partial t} - r_m \right) dV = -\int_A \boldsymbol{n} \cdot (\rho \boldsymbol{u} \psi_m + \boldsymbol{j}_m)\, dA \qquad (m = 1, 2, \ldots, M). \tag{5.10}$$

For the boundary node, this equation is approximated by

$$V\left(\frac{\partial \rho \psi_m}{\partial t} - r_m\right) = -A\boldsymbol{n} \cdot (\rho \boldsymbol{u} \psi_m + \boldsymbol{j}_m) \qquad (m = 1, 2, \ldots, M), \tag{5.11}$$

where A is the area of the reactive surface and V is the volume of the boundary cell. It is assumed that the flux between the boundary cell and other cells is zero, since it is treated in the slow solve.

From the definition of the species flux, that is,

$$\sigma_n \equiv -\boldsymbol{n} \cdot (\rho \boldsymbol{u} \psi_m + \boldsymbol{j}_m), \tag{5.12}$$

Eq. (5.11) may be written as follows:

$$\left(\frac{\partial \rho \psi_m}{\partial t} - r_m\right) = \frac{A}{V}\sigma_m \qquad (m = 1, 2, \ldots, M). \tag{5.13}$$

Summing this equation over all species yields

$$\frac{\partial \rho}{\partial t} = \frac{A}{V}\sum_m \sigma_m. \tag{5.14}$$

Thus, the fast species equation on the boundary is

$$\frac{\partial \psi_m}{\partial t} = \frac{A}{\rho V}\left(\sigma_m - \psi_m \sum_i \sigma_i\right) + \frac{r_m}{\rho} \qquad (m = 1, 2, \ldots, M). \tag{5.15}$$

It is assumed that the reactive surfaces have Dirichlet boundary conditions on the temperature:

$$\theta = T_s(t) \quad \text{(on boundary)} \tag{5.16}$$

The Stefan velocity is computed from the following differential equation:

$$\frac{\partial \phi}{\partial t} = \frac{1}{\rho}\sum_m \sigma_m = u_s. \tag{5.17}$$

with $\phi(0) = 0$. Integrating from time t^n to t^{n+1} yields

$$\phi^{n+1} - \phi^n = \overline{u}_s \Delta t_n, \tag{5.18}$$

where $\overline{u}_s$ is the mean Stefan velocity during the integration step.

The time rate of change of the areal concentration of the kth surface species is given by is given by

$$\frac{d\eta_k}{dt} = \frac{\sigma_k}{w_k} \quad \text{for all surface species.} \tag{5.19}$$

The rate of change of the site fractions, $dz_k(n)/dt$, is obtained by differentiating Eq. (2.60) with respect to time and using Eq. (5.19) to eliminate $d\eta_k/dt$. The result is as follows:

$$\frac{dz_k(n)}{dt} = \frac{\sigma_k \upsilon_k(n)}{w_k \gamma_k} - \frac{z_k(n)}{\gamma_k}\frac{d\gamma_k}{dt} \quad \text{(for all surface species).} \tag{5.20}$$

The solid mass deposited per unit area per unit time, $\dot{m}''$, is given by

$$\dot{m}'' = \frac{dm''}{dt} = \sum_{k \in N_b} \sigma_k, \tag{5.21}$$

where $k \in N_b$ implies a summation over all solid bulk species. In this analysis, it is assumed that the CVD growth at the control volume surface is uniform and planar. Hence, variations in the computation of film growth are limited by the grid resolution at the surface.

The time rate of change of the surface site densities is given by

$$\frac{d\gamma_k}{dt} = g(t), \tag{5.22}$$

where $g(t) = 0$ if the site densities are constant.

Hence, the fast equation system at the boundary cells is given by Eqs. (5.14), (5.15), (5.16), (5.17), (5.20), (5.21) and (5.22).

The Slow Part of the Species Equations in the Interior and on the Boundary

The slow part of the species equations is given by

$$\frac{\partial \rho \psi_m}{\partial t} + \nabla \cdot (\rho \boldsymbol{u} \psi_m) = \nabla \cdot \sum_{n=1}^{M} \rho \Gamma_{mn} \nabla \psi_n + \nabla \cdot \left(\frac{d_m^T}{\theta} \nabla \theta \right)$$
$$(m = 1, 2, \ldots, M), \tag{5.23}$$

which is obtained by setting $r_m = 0$ in Eq. (2.45). The discretization of this equation is implicit on the diagonal component, Γ_{mm}, of the diffusion coefficients and explicit on the convective term and off-diagonal diffusion terms. The density is held fixed. The discretization formula is as follows:

$$\left[\frac{\rho^n}{\Delta t}\boldsymbol{I} - \boldsymbol{\nabla}\cdot(\rho^n\Gamma^n_{mm}\boldsymbol{\nabla})\right]\psi^{n+1}_m = \frac{\rho^n}{\Delta t}\psi^n_m - \boldsymbol{\nabla}\cdot(\rho^n\boldsymbol{u}^n\psi^n_m) + \sum_{\substack{i=1\\ i\neq m}}\boldsymbol{\nabla}\cdot(\rho^n\Gamma^n_{mi}\boldsymbol{\nabla}\psi^n_i) + \boldsymbol{\nabla}\cdot\left(\left(\frac{d^{\Gamma^n}_m}{\theta^n}\right)\boldsymbol{\nabla}\theta^n\right), \quad (m = 1,2,\ldots,M), \quad (5.24)$$

where $\boldsymbol{I}$ is the identity matrix. This discretization decouples the species equations, resulting in M distinct matrix problems. The constraint given by Eq. (2.5) requires the solution of $M-1$ species equations. However, all M equations are solved in order to determine the error in conservation of the mass fractions.

The boundary condition on the equation is a zero flux of all species at all surfaces. The flux of gas species due to heterogeneous chemical reaction is taken care of by the fast solve on the boundary nodes. The zero flux boundary condition applied by setting the scalar values Γ_{mn} and d^{Γ}_m to zero at the faces of the control volumes at the boundary surface. This zeros out the contribution to the flux on the boundary faces of the control cells when computing the various divergence operators. The ghost point values of the mass fractions are obtained by extrapolation.

The Slow Part of the Energy Equation in the Interior and on the Boundary

The slow part of the species equations is obtained by setting $\sum_m e_m r_m = 0$ in the energy equation. The discretization is is fully implicit, as follows:

$$\left[\rho^n c^n_v\left(\frac{1}{\Delta t}\boldsymbol{I} - \boldsymbol{u}^n\cdot\boldsymbol{\nabla}\right) - \boldsymbol{\nabla}\cdot(k^n\boldsymbol{\nabla}) + \rho^n\frac{\mathcal{R}}{\bar{w}^n}(\boldsymbol{\nabla}\cdot\boldsymbol{u}^n)\boldsymbol{I} + \sum_m\frac{\mathcal{R}}{w^n_m}(\boldsymbol{\nabla}\cdot\boldsymbol{j}^n_m)\boldsymbol{I} + \sum_m c^n_{p_m}\boldsymbol{j}^n_m\cdot\boldsymbol{\nabla}\right]\theta^{n+1} = \frac{\rho^n c^n_v}{\Delta t}\theta^n. \quad (5.25)$$

Dirichlet boundary conditions are applied to all boundary nodes, and the ghost point values are obtained by extrapolation.

5.3.3 Update of the Background Pressure

The fast and slow solves can result in changes in composition, temperature and density. The pressure field computed by the ideal gas law using these quantities will not, in general, be spatially uniform. A smoothing procedure is performed after the fast and slow solves to adjust the background pressure consistent with the ideal gas law.

The background pressure smoothing step after the fast solve is as follows. First, the average change in the species concentrations is computed using

$$\Delta c_m = \frac{1}{V_{sys}} \int_V \left(\frac{\chi_m^* \rho^*}{\tilde{w}^*} - \frac{\chi_m^n \rho^n}{\tilde{w}^n} \right) dV \qquad (m = 1, 2, \ldots, M), \tag{5.26}$$

where the states before and after the fast solve are represented by n and $*$, respectively. The integrand represents the local change in the concentration of the mth species. The integral of this quantity is the global change in the number of moles of the mth species. Dividing this result by the system volume, V_{sys}, yields the average global change in the concentration of that species. This change is added to the local species concentration prior to the stiff solve.

$$c_m^{**} = c_m^n + \Delta c_m, \tag{5.27}$$

where $**$ represents the system state after the pressure smoothing step. This procedure conserves the total number of moles of each species, and therefore mass. The total concentration after the smoothing step is given by

$$c^{**} = \sum_{m=1}^{M} c_m^{**}. \tag{5.28}$$

Using, Eq. (2.4), the mole fractions are

$$\chi_m^{**} = \frac{c_m^{**}}{c^{**}}, \tag{5.29}$$

From Eq. (2.9), the mean molecular weight is given by

$$\tilde{w}^{**} = \sum_{m=1}^{M} \chi_m^{**} w_m. \tag{5.30}$$

The density is computed from Eq. (2.7):

$$\rho^{**} = c^{**}\tilde{w}^{**}. \tag{5.31}$$

The background pressure is then determined as follows:

$$p_o^{**} = \frac{1}{V_{sys}} \int_V \frac{\rho^{**}\mathcal{R}\theta^*}{\tilde{w}^{**}}\, dV. \tag{5.32}$$

Using the ideal gas law, the local temperature after the smoothing step is given by

$$\theta^{**} = \frac{p_o^{**}\tilde{w}^{**}}{\rho^{**}\mathcal{R}}. \tag{5.33}$$

The smoothing procedure following the slow energy and species equation solve is simpler, since there is no net change in mass (or moles) of the system. Thus,

$$m^{n+1} = m^{**}, \tag{5.34}$$

where

$$m^{**} = \int_V \rho^{**}\, dV, \tag{5.35}$$

can be computed directly. Also,

$$m^{n+1} = \int_V \frac{p^{n+1}\tilde{w}^{n+1}}{\mathcal{R}\theta^{n+1}}\, dV, \tag{5.36}$$

where θ^{n+1} and $\tilde{w}^{n+1}$ are the temperature and mean molecular weight after the slow species and energy solves.

Equating Eqs. (5.35), (5.36), and recognizing that $p_o \approx p$, the background pressure is determined as follows:

$$p_o^{n+1} = \frac{m^{**}}{\int_V \tilde{w}^{n+1}/\left(\mathcal{R}\theta^{n+1}\right)\, dV}. \tag{5.37}$$

The density field at the $n+1$ state is then computed by

$$\rho^{n+1} = \frac{p_o^{n+1}}{\tilde{w}^{n+1}}\mathcal{R}\theta^{n+1}. \tag{5.38}$$

Hence, the density, composition, temperature, and background pressure are consistent with the ideal gas law at the $n+1$ time step.

5.3.4 Momentum Equation

The Static Pressure Distribution

The static pressure distribution is computed by solving

$$\frac{1}{\rho^{n+1}}\nabla p_s^{n+1} = \boldsymbol{g}, \tag{5.39}$$

which is obtained by setting $\boldsymbol{u} = 0$ in the momentum equation. The divergence of the hydrostatic equation is given by

$$\nabla \cdot \left(\frac{1}{\rho^{n+1}}\nabla p_s^{n+1}\right) = 0. \tag{5.40}$$

This equation is solved with the boundary condition specified by taking the normal component of Eq. (5.39):

$$\boldsymbol{n} \cdot \frac{1}{\rho^{n+1}}\nabla p_s^{n+1} = \boldsymbol{n} \cdot \boldsymbol{g}. \tag{5.41}$$

In matrix form, the differential equation and boundary conditions may be written as follows:

$$\boldsymbol{A}\boldsymbol{p}_s = \boldsymbol{f}. \tag{5.42}$$

This system of equations is singular, since a constant added to the solution satisfies both the differential equation and the boundary conditions. The singularity is removed by augmenting the system as follows:

$$\begin{aligned} \boldsymbol{A}\boldsymbol{p}_s + \alpha \boldsymbol{r} &= \boldsymbol{f} \\ \boldsymbol{r}^T \boldsymbol{p}_s &= \beta, \end{aligned} \tag{5.43}$$

where α is a constant and β is a real number, $\boldsymbol{r}$ is a vector which makes the system of equations non-singular. It is easily verified that

$$\alpha = \frac{\boldsymbol{l}^T \boldsymbol{f}}{\boldsymbol{l}^T \boldsymbol{r}}, \tag{5.44}$$

where $\boldsymbol{l}^T$ is the null vector of $\boldsymbol{A}$.

From Eq. (5.40), $\boldsymbol{f} = 0$. If $\boldsymbol{r}$ is chosen such that $\boldsymbol{l}^T\boldsymbol{r} \neq 0$, then $\alpha = 0$. Thus, the solution to the augmented system yields the same solution to $\boldsymbol{p}_s$ as the original system. The vector $\boldsymbol{r}$ is arbitrarily chosen to be a column of ones. This has been found to make the system of equations nonsingular in all case studies encountered.

Integration of the Momentum Equation

The momentum equation is given by

$$\frac{\partial \boldsymbol{u}}{\partial t} + \frac{1}{\rho}\nabla(p_d + p_s) = \boldsymbol{g} + \frac{1}{\rho}\nabla \cdot \boldsymbol{T} - \boldsymbol{u} \cdot \nabla \boldsymbol{u}, \tag{5.45}$$

where $\boldsymbol{T}$ is the stress tensor.

The following discretization is used to obtain the velocity at the new time step:

$$\frac{\boldsymbol{u}^{n+1} - \boldsymbol{u}^* + \boldsymbol{u}^* - \boldsymbol{u}^n}{\Delta t} + \frac{1}{\rho^{n+1}}\nabla(p_d + p_s)^{n+1} = \boldsymbol{g} + \frac{1}{\rho^{n+1}}\nabla \cdot \boldsymbol{T}^{n*} - \boldsymbol{u}^n \cdot \nabla \boldsymbol{u}^*, \tag{5.46}$$

where

$$\boldsymbol{T}^{n*} = \mu^n \left[\nabla \boldsymbol{u}^* + (\nabla \boldsymbol{u}^n)^T - \frac{2}{3}\mu^n (\nabla \cdot \boldsymbol{u}^n) \boldsymbol{I} \right], \tag{5.47}$$

and

$$\nabla(p_d + p_s)^{n+1} \equiv \nabla \left(p_d^n + p_s^{n+1} \right) + \nabla\phi. \tag{5.48}$$

The velocity at the intermediate state, designated by $\boldsymbol{u}^*$ determined from

$$\frac{\boldsymbol{u}^* - \boldsymbol{u}^n}{\Delta t} + \frac{1}{\rho^{n+1}}\nabla \left(p_d^n + p_s^{n+1} \right) = \boldsymbol{g} + \frac{1}{\rho^{n+1}}\nabla \cdot \boldsymbol{T}^{n*} - \boldsymbol{u}^n \cdot \nabla \boldsymbol{u}^*, \tag{5.49}$$

with the boundary conditions as follows:

$$\boldsymbol{u} \cdot \boldsymbol{t} = 0 \quad \text{on all surfaces} \tag{5.50}$$

$$\boldsymbol{u} \cdot \boldsymbol{n} = \begin{cases} 0 & \text{on all surfaces} \\ u_s & \text{on reactive surfaces} \end{cases} \tag{5.51}$$

The solution for $\boldsymbol{u}^*$ will not, in general, satisfy continuity. The projection step is

$$\frac{\boldsymbol{u}^{n+1} - \boldsymbol{u}^*}{\Delta t} + \frac{1}{\rho^{n+1}}\nabla\phi = 0. \tag{5.52}$$

The projection equation is obtained by taking the divergence of this equation:

$$\nabla \cdot \frac{1}{\rho^{n+1}} \nabla \phi = \frac{1}{\Delta t} \left(\nabla \cdot \boldsymbol{u}^* - \nabla \cdot u^{n+1} \right). \tag{5.53}$$

A volume average divergence is used in the source term to eliminate the propagation of density waves. Defining $Q \equiv \nabla \cdot \boldsymbol{u}$, the average divergence is obtained by by integrating the divergence over the volume:

$$\begin{aligned} \overline{Q} &= \frac{1}{V_{sys}} \int_V Q \, dV, \\ &= \frac{1}{V_{sys}} \int_A \boldsymbol{u} \cdot \boldsymbol{n} \, dA, \\ &= \frac{1}{V_{sys}} \int_A u_s \, dA, \end{aligned} \tag{5.54}$$

where u_s is the Stefan velocity on the reactive surfaces.

The local divergence, from the continuity equation, is given by

$$Q = -\frac{D \ln \rho}{Dt}. \tag{5.55}$$

The local divergence is not used in this model, since it adds a term into the projection of the form $\partial^2 \rho / \partial t^2$. The integral formulation of the projection smoothes out the density waves and still enforces continuity globally. Furthermore, the integral formulation directly yields the result that

$$\overline{Q} = 0, \tag{5.56}$$

when there is no heterogeneous chemistry. This result is consistent with the theory of compressible flow in the zero Mach number limit (Pember et al., 1999).

Thus, the projection equation is

$$\nabla \cdot \frac{1}{\rho^{n+1}} \nabla \phi = \frac{1}{\Delta t} \left(\nabla \cdot \boldsymbol{u}^* - \overline{Q} \right), \tag{5.57}$$

and boundary conditions on this equation are

$$a\phi + b\boldsymbol{n} \cdot \nabla \phi = 0 \quad \text{on all walls}, \tag{5.58}$$

where a and b where $a = 0$ and $b = 1$ for reactive walls, non-reactive walls, and inflow boundaries. At an outflow boundary, $a = 1$ and $b = 0$. In a CVD batch system there are, however, no inflow or outflow boundaries. Thus, the system of equations for the projection equation is singular, and the solution is obtained by the same technique as that for the static pressure distribution.

The velocity and pressure corrections are as follows:

$$\boldsymbol{u}^{n+1} = \boldsymbol{u}^n - \frac{\Delta t}{\rho^{n+1}} \nabla \phi. \tag{5.59}$$

$$p_d^{n+1} = p_d^n + \phi. \tag{5.60}$$

The projection method has one main limitation. The projected velocity field cannot satisfy the boundary conditions on both components of velocity specified by Eqs. (5.50) and (5.51). This is because the boundary condition on the projection equation, Eq. (5.58), is defined in terms of the vector normal to the surface. In this case, only the boundary condition on the normal component of velocity is preserved. The tangential component will, in general, change after the velocity correction. Fortunately this is not of major consequence because the tangential component of velocity is enforced the next time the momentum equation, Eq. (5.49), is integrated.

5.4 Spatial Discretization of Differential Operators

The OVERTURE framework for the solution of differential equations employs the overset grid method. In this approach the physical domain is subdivided into a set of logically rectangular subdomains which are allowed to overlap at their boundaries. The physical boundaries of the subdomains lie along the physical boundaries of the original domain.

Each subdomain has a mathematical mapping to a unit square (or cube). This mapping allows the derivatives of the domain to be expressed in terms of derivatives

on the unit square. The derivatives and derivative operators are discretized with second- or fourth-order accurate central differences applied to the equations in the computational (unit cube) coordinates, as will be outlined.

Finite differences are compactly represented using shift and derivative operators (Strikwerda, 1989; Henshaw, 2000). The shift operator in the mth coordinate direction is defined as follows:

$$E_{+m}\boldsymbol{u}_i \equiv \left\{ \begin{array}{ll} \boldsymbol{u}_{i_1+1,i_2,i_3} & \text{if } m=0, \\ \boldsymbol{u}_{i_1,i_2+1,i_3} & \text{if } m=1, \\ \boldsymbol{u}_{i_1,i_2,i_3+1} & \text{if } m=2, \end{array} \right\}, \tag{5.61}$$

and the difference operators are given by

$$D_{+r_m} = \frac{E-1}{\Delta r_m} \tag{5.62}$$

$$D_{-r_m} = \frac{1-E^{-1}}{\Delta r_m} \tag{5.63}$$

$$D_{0r_m} = \frac{E-E^{-1}}{2\Delta r_m} \tag{5.64}$$

$$D_{+m_1,m_2} = \frac{E_{+m1}E_{+m2}-1}{\Delta r_m} \tag{5.65}$$

$$D_{+m} = E_{+m} - 1. \tag{5.66}$$

The inverse shift operator, E^{-1}, is given by

$$E\phi_i = \phi_{i+1} \tag{5.67}$$

$$E^{-1}E\phi_i = E^{-1}\phi_{i+1} \tag{5.68}$$

$$\phi_i = E^{-1}\phi_{i+1}. \tag{5.69}$$

Let D_{2r_m}, $D_{2r_mr_n}$, D_{2x_m}, and $D_{2x_mx_n}$ denote second-order accurate derivatives with respect to $\boldsymbol{r}$ and $\boldsymbol{x}$, where $\boldsymbol{r}$ and $\boldsymbol{x}$ represent the position vectors in computational and physical space, respectively. The derivatives with respect to $\boldsymbol{r}$ are the standard centered difference approximations. For example,

$$\frac{\partial \boldsymbol{u}}{\partial r_m} \approx D_{2r_m}\boldsymbol{u}_i = \frac{\left(E_{+m}-E_{+m}^{-1}\right)\boldsymbol{u}_i}{2\left(\Delta r_m\right)} \tag{5.70}$$

$$\frac{\partial^2 \boldsymbol{u}}{\partial r_m^2} \approx D_{2r_mr_n}\boldsymbol{u}_i = \frac{\left(E_{+m}-2+E_{+m}^{-1}\right)\boldsymbol{u}_i}{\left(\Delta r_m\right)^2} \tag{5.71}$$

where Δr_m is the equal to $1/(N_m - 1)$, where N_m is the number of vertices in the m-direction not including ghost points. Similar expressions, shown in Henshaw (2000), give the finite difference operators for fourth-order accuracy.

The derivatives with respect to $\boldsymbol{x}$ are defined by the chain rule. For the second-order approximations, the first and second derivatives are

$$\frac{\partial \boldsymbol{u}}{\partial x_m} = \sum_n \frac{\partial r_n}{\partial x_m}\frac{\partial \boldsymbol{u}}{\partial r_n} \tag{5.72}$$

$$\approx D_{2x_m}\boldsymbol{u}_i = \sum_n \frac{\partial r_n}{\partial x_m} D_{2r_m}\boldsymbol{u}_i \tag{5.73}$$

$$\frac{\partial^2 \boldsymbol{u}}{\partial r_m^2} = \sum_n \frac{\partial^2 r_n}{\partial x_m^2}\frac{\partial \boldsymbol{u}}{\partial r_n} + \sum_n \sum_l \frac{\partial r_n}{\partial x_m}\frac{\partial r_l}{\partial x_m}\frac{\partial^2 \boldsymbol{u}}{\partial r_n \partial r_l} \tag{5.74}$$

$$\approx D_{2x_m x_m}\boldsymbol{u}_i = \sum_n (D_{2x_m})\frac{\partial r_n}{\partial x_m} D_{2r_n}\boldsymbol{u}_i + \sum_n \sum_l \frac{\partial r_n}{\partial x_m}\frac{\partial r_l}{\partial x_m} D_{2r_m r_l}\boldsymbol{u}_i. \tag{5.75}$$

The elements of the Jacobian matrix, $\partial r_m/\partial x_n$ are known from the geometrical information of the grid, and are computed by OVERTURE functions by member functions from the `CompositeGridOperators` class (Chesshire and Henshaw, 1999).

5.5 Finite Differences in Conservative Form

Conservative finite difference operators are part of OVERTURE's `CompositeGrid-Operators` class. These include the divergence, Laplacian, "divScalarGrad," and "mixed derivative" operators. Defining J to be the determinant of the Jacobian matrix of the transformation derivatives,

$$J = \left|\frac{\partial \boldsymbol{x}}{\partial \boldsymbol{r}}\right|, \tag{5.76}$$

it can be shown that $J d\boldsymbol{r}$ is a measure of the volume in physical space.

The divergence operator is

$$\begin{aligned} \nabla_x \cdot \boldsymbol{u} &= \sum_i \frac{\partial u_i}{\partial x_i} \\ &= \sum_i \sum_j \frac{\partial r_j}{\partial x_i}\frac{\partial u_i}{\partial r_j}. \end{aligned} \tag{5.77}$$

It may be written in conservation form for the computational variables as follows (Henshaw, 2000):

$$\begin{aligned}\nabla_x \cdot \boldsymbol{u} &= \frac{1}{J}\sum_j \frac{\partial}{\partial r_j}\left[\sum_i J\frac{\partial r_j}{\partial x_i}u_i\right]. \\ &= \frac{1}{J}\nabla_r \cdot \boldsymbol{U},\end{aligned} \tag{5.78}$$

where $\boldsymbol{U}$ is the scaled transform of $\boldsymbol{u}$ in the computational space:

$$U_i = J\sum_k \frac{\partial r_i}{\partial x_k}u_k. \tag{5.79}$$

The conservative form of the divergence operator is used in the discretization of Eqs. (5.24), (5.25), (5.49), and (5.57) in a manner described in Section 3.5.2.

The is called conservation form for the computational variables because integrals over $d\boldsymbol{r}$ space can be expressed in a simple form from which the divergence theorem may be applied:

$$\begin{aligned}\int \nabla_x \cdot \boldsymbol{u}\, d\boldsymbol{x} &= \int \nabla_x \cdot \boldsymbol{u}\, J\, d\boldsymbol{r}. \\ &= \int \nabla_r \cdot \boldsymbol{U}\, d\boldsymbol{r}.\end{aligned} \tag{5.80}$$

The Laplacian operator in in conservative form is derived using the divergence of the gradient:

$$\begin{aligned}\nabla^2\phi &= \frac{1}{J}\sum_j \frac{\partial}{\partial r_j}\left[\sum_i J\frac{\partial r_j}{\partial x_i}\frac{\partial \phi}{\partial x_i}\right] \\ &= \frac{1}{J}\sum_j \frac{\partial}{\partial r_j}\left[\sum_i J\frac{\partial r_j}{\partial x_i}\sum_k \frac{\partial r_k}{\partial x_i}\frac{\partial \phi}{\partial x_k}\right].\end{aligned} \tag{5.81}$$

The "divScalarGrad" operator, $\nabla \cdot (a(\boldsymbol{x})\nabla\phi)$ is given in conservation form by

$$\nabla \cdot (a(\boldsymbol{x})\nabla\phi) = \frac{1}{J}\sum_j \frac{\partial}{\partial r_j}\left[\sum_i J\frac{\partial r_j}{\partial x_i}a\sum_k \frac{\partial r_k}{\partial x_i}\frac{\partial \phi}{\partial r_k}\right]. \tag{5.82}$$

For clarity, this expression is written out in full for two dimensions:

$$\begin{aligned}\nabla\cdot(a(\boldsymbol{x})\nabla\phi) = \frac{1}{J}\Bigg\{ & \frac{\partial}{\partial r_1}\left(aJ\left[\left(\frac{\partial r_1}{\partial x_1}\right)^2+\left(\frac{\partial r_1}{\partial x_2}\right)^2\right]\frac{\partial\phi}{\partial r_1}\right)+\\ & \frac{\partial}{\partial r_2}\left(aJ\left[\left(\frac{\partial r_2}{\partial x_1}\right)^2+\left(\frac{\partial r_2}{\partial x_2}\right)^2\right]\frac{\partial\phi}{\partial r_2}\right)+\\ & \frac{\partial}{\partial r_1}\left(aJ\left[\frac{\partial r_1}{\partial x_1}\frac{\partial r_2}{\partial x_1}+\frac{\partial r_1}{\partial x_2}\frac{\partial r_2}{\partial x_2}\right]\frac{\partial\phi}{\partial r_2}\right)+\\ & \frac{\partial}{\partial r_2}\left(aJ\left[\frac{\partial r_1}{\partial x_1}\frac{\partial r_2}{\partial x_1}+\frac{\partial r_1}{\partial x_2}\frac{\partial r_2}{\partial x_2}\right]\frac{\partial\phi}{\partial r_1}\right)\Bigg\}. \end{aligned} \tag{5.83}$$

A slightly modified form of this expression is as follows:

$$\begin{aligned}\nabla\cdot(a(\boldsymbol{x})\nabla\phi) = \frac{1}{J}\Bigg\{ & \frac{\partial}{\partial r_1}\left(A^{11}\frac{\partial\phi}{\partial r_1}\right)+\frac{\partial}{\partial r_1}\left(A^{12}\frac{\partial\phi}{\partial r_2}\right)+\\ & \frac{\partial}{\partial r_2}\left(A^{21}\frac{\partial\phi}{\partial r_1}\right)+\frac{\partial}{\partial r_2}\left(A^{22}\frac{\partial\phi}{\partial r_2}\right)+\Bigg\}, \end{aligned} \tag{5.84}$$

where

$$A^{11} \equiv aJ\left[\left(\frac{\partial r_1}{\partial x_1}\right)^2+\left(\frac{\partial r_1}{\partial x_2}\right)^2\right] \tag{5.85}$$

$$A^{12}=A^{21} \equiv aJ\left[\frac{\partial r_1}{\partial x_1}\frac{\partial r_2}{\partial x_1}+\frac{\partial r_1}{\partial x_2}\frac{\partial r_2}{\partial x_2}\right] \tag{5.86}$$

$$A^{22} \equiv aJ\left[\left(\frac{\partial r_2}{\partial x_1}\right)^2+\left(\frac{\partial r_2}{\partial x_2}\right)^2\right]. \tag{5.87}$$

A second-order accurate compact discretization to this expression at the grid point located at (i_1, i_2) is

$$\begin{aligned}\nabla\cdot(a(\boldsymbol{x})\nabla\phi)_{i_1,i_2} \approx \frac{1}{J}\Big\{ & D_{+r_1}\left(A^{11}_{i_1-1/2,i_2}D_{-r_1}\phi_{i_1,i_2}\right)+\\ & D_{+r_2}\left(A^{22}_{i_1,i_2-1/2}D_{-r_2}\phi_{i_1,i_2}\right)+\\ & D_{+r_1}\left(A^{12}_{i_1-1/2,i_2}D_{0r_2}\phi_{i_1,i_2}\right)+\\ & D_{+r_2}\left(A^{21}_{i_1,i_2-1/2}D_{0r_1}\phi_{i_1,i_2}\right)\Big\}. \end{aligned} \tag{5.88}$$

This derivative operator was added to the OVERTURE suite as part of this work and is incorporated into the spatial discretization of Eqns.(5.24), (5.25), (5.49), and (5.57).

The mixed derivative operator $\partial/\partial x_i(s\partial/\partial x_j)$, where i and j represent two independent coordinates, is determined by taking the divergence of

$$s\frac{\partial \phi}{\partial x_j}\boldsymbol{e}_i.$$

The divergence of this vector is

$$\begin{aligned}\boldsymbol{\nabla}_x \cdot \left(s\frac{\partial \phi}{\partial x_j}\boldsymbol{e}_i\right) &= \frac{\partial}{\partial x_i}\left(s\frac{\partial \phi}{\partial x_j}\right) \\ &= \frac{1}{J}\boldsymbol{\nabla}_r \cdot (\boldsymbol{A}\boldsymbol{\nabla}_r \phi),\end{aligned}$$

where the tensor $\boldsymbol{A}$ is given by

$$\boldsymbol{A} = sJ\begin{bmatrix} \frac{\partial r_1}{\partial x_i}\frac{\partial r_1}{\partial x_j} & \frac{\partial r_1}{\partial x_i}\frac{\partial r_2}{\partial x_j} \\ \frac{\partial r_2}{\partial x_i}\frac{\partial r_1}{\partial x_j} & \frac{\partial r_2}{\partial x_i}\frac{\partial r_2}{\partial x_j} \end{bmatrix}.$$

This derivative operator was also added to the OVERTURE suite as part of this work, and is incorporated into the spatial discretization of Eq. (5.49).

Again, it should be noted that these stencils are second-order accurate, and that the transformation derivatives, as well as the Jacobian, at each point in the grid is known. The scalar values A^{11}, A^{12}, etc. must be known at all cell faces, that is, the points between the vertices. The scalar values are determined by a special averaging procedure whereby the geometric terms are arithmetically averaged and the original scalar values are harmonically averaged. The harmonic average of s_i and s_{i+1} is defined by

$$\tilde{s}_{i+1/2} \equiv \frac{2s_i s_{i+1}}{s_i + s_{i+1}}.$$

The arithmetic average of s_i and s_{i+1} is defined by

$$\hat{s}_{i+1/2} \equiv \frac{1}{2}(s_i + s_{i+1}).$$

Recalling that

$$\begin{aligned}A^{11} &= aJ\left[\left(\frac{\partial r_1}{\partial x_1}\right)^2 + \left(\frac{\partial r_1}{\partial x_2}\right)^2\right] \\ &= aF,\end{aligned}$$

the face average value of A^{11} is given by

$$A^{11}_{i+1/2} = \tilde{a}_{i+1/2}\hat{F}_{i+1/2}. \tag{5.89}$$

This averaging procedure is used for two reasons. First, the mapping derivatives may switch sign on the grid, and an arithmetic average is more appropriate. The harmonic average is used on the scalar quantity because one can define a zero scalar face value for a boundary cell by assigning zero to the scalar on the ghost line. The harmonic average average of anything with zero is zero, and thus the zero flux boundary conditions are computed in this manner. Furthermore, it is shown in Patankar (1980) that the harmonic average is preferred in diffusion problems.

5.6 Closure

In this chapter, the temporal and spatial discretization of the differential equations of the CVD batch model is given in detail. A flowchart of the solver, presented at the beginning of the chapter, outlines the general procedure implemented into the user application code. The solver, written using the OVERTURE class library, strictly follows the flow of information presented in this chapter. In the next chapter, the solver is first validated and then used to model several CVD batch systems.

Chapter 6

MODEL VERIFICATION AND SIMULATION RESULTS

6.1 Model Verification

Many verification studies were conducted during the writing of the CVD batch model solver. Each component of the solver, i.e., the species equation slow solve, energy equation slow solve, the energy and species equation fast solve, the momentum solve was verified separately. In these tests, verification implies that the solution for each component was compared against a known analytical solution when available, or the solution was compared against a benchmark solution from another model.

One of the verification tests that merits mention here is the mass conservation study of the slow part of the species continuity equations. In this test, multicomponent diffusion of a mixture of inert gases (initially nonuniform) was allowed to reach a steady state. In this test, the reactor walls were nonreactive and the temperature distribution was nonuniform. At the initial state and at steady state, the quantity of gases was integrated to determine the error in the non-conservation of the integration method. Results indicated that the error in mass conservation on a single grid was on the order of the machine precision, and for a composite grid the conservation error was second-order accurate based on the grid spacing.

After the individual solver components were verified, components were coupled and used to solve more difficult problems. This section presents the results of the coupled component verified studies.

In the first coupled component verified study, the momentum and energy equations are coupled and used to model natural convection in a thermally driven square cavity. The results are compared against a benchmark solution from Ismail and

Scalon (2000). Mixed convection verification studies were not conducted, since it is assumed that the primary driving force behind fluid motion in the batch reactor is natural convection. This assumption would be invalid if there were stirring elements, rotating susceptors, or other devices that would induce a forced convective flow.

In the second study, the fast and slow energy and species solvers are coupled and used to predict the transient deposition of tungsten in a low-pressure batch reactor. The results are compared against a model of a perfectly-stirred isothermal reactor Coltrin et al. (1996).

6.1.1 Natural Convection in a Driven Cavity

A benchmark solution of natural convection in a square cavity with adiabatic top and bottom walls and with the side walls maintained at constant, but different, temperatures was obtained by Ismail and Scalon (2000). The velocity and temperature fields were computed as a function of the Rayleigh number, Ra, where

$$\mathsf{Ra} \equiv \mathsf{PrGr}. \tag{6.1}$$

The Grashof number in that work was defined as follows:

$$\mathsf{Gr} = \frac{\rho_c^2 \beta \Delta_c \theta g l_c^3}{\mu_c^2}, \tag{6.2}$$

where β is the coefficient of thermal expansion, and l_c is the length of the reactor.

The model of this work uses dimensional quantities for its variables. To compare the present simulations with the benchmark solution, the system pressure was computed as a function of the Rayleigh number and the other operating conditions of the system.

The operating pressure of the reactor is given as follows:

$$p_c = \sqrt{\left(\frac{\mathsf{Ra}}{\mathsf{Pr}}\right)\left(\frac{\tilde{\theta}}{\Delta_c \theta}\right)\left(\frac{\mu_c^2}{g l_c^3}\right)\left(\frac{\mathcal{R}^2 \theta_c^2}{\tilde{w}^2}\right)}. \tag{6.3}$$

This equation is derived as follows. First, the Grashof number defined by Eq. (4.10) is equivalent to the Grashof number defined by Eq. (6.2) if

$$\beta = \frac{1}{\tilde{\theta}}, \tag{6.4}$$

where $\tilde{\theta}$ is the harmonic average of the wall temperatures. Also,

$$\rho_c = \frac{p_c \tilde{w}}{\mathcal{R}\theta_c}. \tag{6.5}$$

Eq. (6.3) is obtained by substituting Eqns. (6.2), (6.4), and (6.5) into Eq. (6.1) and solving in terms of p_c.

The simulations were conducted for a system with following set of operating conditions:

$l_c = 10$ cm,	$\theta_{\text{hot}} = 400$ K
$\theta_{\text{cold}} = 300$ K	$\theta_c = 350$ K
$\tilde{\theta} = 342$ K	$\Delta_c\theta = 100$ K
$\mathcal{R} = 8.314 \times 10^7$ erg mol^{-1} K^{-1}	$\tilde{w} = 31.6$ g mol^{-1}.
$\mathsf{Pr} = 0.17$	$\mu_c = 2.0 \times 10^{-4}$ g cm^{-1} s^{-1}

The fluid properties were computed for a 90%/10% mixture (by mole fraction) of H_2 and WF_6 evaluated at θ_c. Inserting these values into Eq. (6.3),

$$p_c = 834\sqrt{\mathsf{Ra}}\ \text{dyne cm}^{-2}. \tag{6.6}$$

Simulations were run for $\mathsf{Ra} = 10^3$ and $\mathsf{Ra} = 10^4$.

The simulations were performed on a uniform 21×21 grid, as were the benchmark computations of Ismail and Scalon (2000). This simulations were run until steady-state solutions were obtained, such that the maximum change in all variables was less than 0.01%. The streamlines and isotherms for these simulations are shown in Figs. (6.1) and (6.2). In each of these figures, the top two plots are from the benchmark solution, and the bottom two plots are those from this work. A quantitative

Ra	p_c	U_{max}	U^*_{max}	%Diff U_{max}	V_{max}	V^*_{max}	%Diff V_{max}
10^3	26,400	14.6	14.7	−1.0%	14.9	14.9	−0.0%
10^4	83,400	21.8	21.0	−3.8%	25.2	25.5	−1.2%

Table 6.1: Comparison between simulations of this work and that of Ismail and Scalon (2000) for the driven cavity problem for several values of Ra. The comparison is made between the maximum value of the components of velocity, U_{max} and V_{max}. The * represents the work of Ismail and Scalon (2000).

comparison of the solutions is shown in Table 6.1. In this table, the maximum value of the components of velocity are compared. The maximum error was less than 4%.

6.1.2 Transient CVD in a Batch Reactor

The batch CVD model of this work was compared against a model of CVD in a perfectly-stirred, constant volume, isothermal reactor (PSR) (Coltrin et al., 1996). The film deposition thickness for both models was computed as a function of time until the reaction was near completion.

The system studied was low pressure CVD of tungsten by H_2 reduction of WF_6. This system consists of a set of 6 gas phase species (1 inert), 10 surface species, 1 bulk species, and 16 heterogeneous chemical reactions. Homogeneous chemical reactions are considered negligible. The reaction mechanism given in Table 6.2 was based on the mechanism originally published by Arora and Pollard (1991); Dandy (2000). The overall reaction mechanism is given by

$$WF_6 + 3H_2 \longrightarrow W(s) + 6HF. \tag{6.7}$$

Note that the total number of moles in the gas phase increases as the reaction proceeds. Thus, for this batch CVD system, the system pressure must increase with time.

The reactor, a 10 cm × 10 cm square chamber, was discretized into a uniform 21 × 21 grid. The reactive surfaces were maintained at 1650 K for all $t > 0$. The

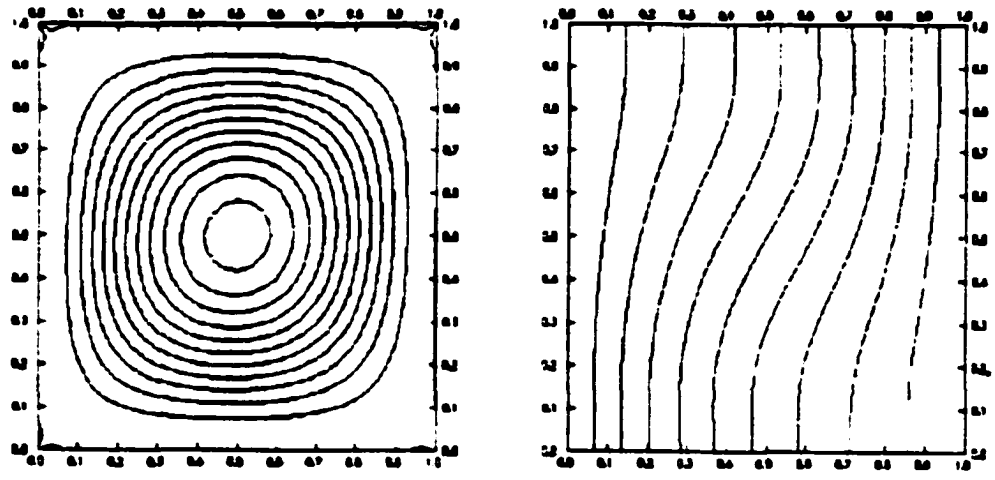

(a) From Ismail and Scalon (2000)

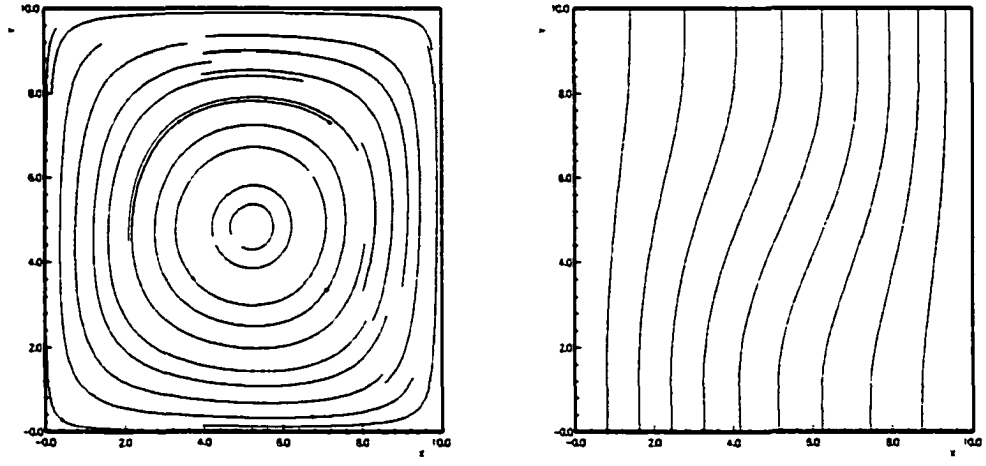

(b) This work

Figure 6.1: Streamlines and isotherms in a square cavity with side walls maintained at two different temperatures and adiabatic walls on the top and bottom, for $\mathbf{Ra} = 10^3$.

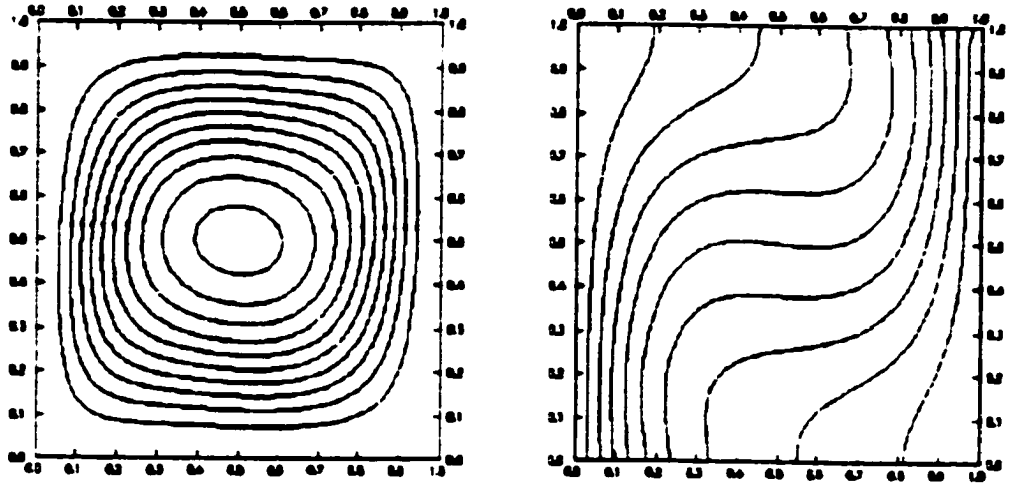

(a) From Ismail and Scalon (2000)

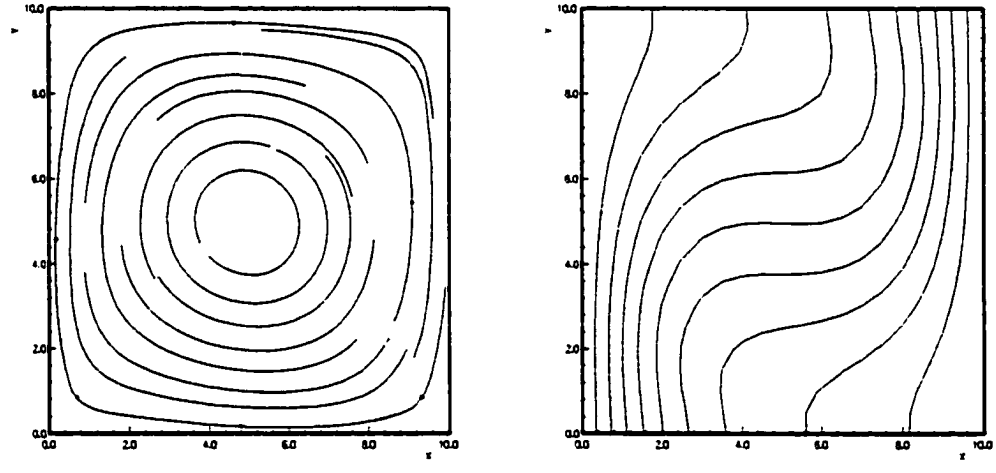

(b) This work

Figure 6.2: Streamlines and isotherms in a square cavity with side walls maintained at two different temperatures and adiabatic walls on the top and bottom, for Ra = 10^4.

	REACTION	A	b	E
1.	H2+4VW<=>2H(2)(S)	7.13E+34	0.0	3974
2.	WF6(2)(S)<=>WF6+2VW	1.58E+15	0.7	33385
	Coverage parameters for species VW:	0.0	0.0	2.007E+04
3.	WF5(2)(S)<=>WF5+2VW	1.88E+16	0.1	33385
	Coverage parameters for species VW:	0.0	0.0	2.007E+04
4.	WF4(2)(S)<=>WF4+2VW	2.08E+16	0.0	33385
	Coverage parameters for species VW:	0.0	0.0	2.007E+04
5.	H(1)(S)+F(2)(S)<=>HF+3VW	3.64E+21	0.9	4769
	Coverage parameters for species VW:	0.0	0.0	1.172E+04
6.	H(2)(S)+F(1)(S)<=>HF+3VW	5.65E+20	0.5	3974
7.	H(2)(S)+F(4)(S)<=>HF+6VW	1.19E+21	1.1	39347
	Coverage parameters for species VW:	0.0	0.0	1.371E+04
8.	H2+F(2)(S)<=>HF+H(2)(S)	2.36E+11	0.7	3974
9.	WF6(2)(S)+2VW<=>F(2)(S)+WF5(2)(S)	6.87E+26	1.4	26231
10.	WF5(2)(S)+2VW<=>F(2)(S)+WF4(2)(S)	1.92E+26	1.7	10930
11.	WF4(2)(S)+2VW<=>F(2)(S)+WF3(2)(S)	4.14E+26	1.4	24840
	Declared duplicate reaction...			
12.	WF4(2)(S)+2VW<=>F(2)(S)+WF3(2)(S)	2.25E+27	0.9	24840
	Declared duplicate reaction...			
13.	WF3(2)(S)+2VW<=>F(2)(S)+W+2F(1)(S)	6.11E+27	0.8	3974
14.	H(2)(S)<=>H(1)(S)+VW	3.32E+11	0.8	32789
	Coverage parameters for species VW:	0.0	0.0	-4.571E+03
15.	F(2)(S)<=>F(1)(S)+VW	3.17E+11	0.8	36962
16.	F(4)(S)<=>F(2)(S)+2VW	6.71E+11	0.6	16891

Table 6.2: Heterogeneous Reactions in CVD of Tungsten by Hydrogen Reduction of Tungsten Hexafluoride, after Arora and Pollard (1991): $k = A\theta^b \exp(-E/\mathcal{R}\theta)$.

initial conditions of the gas were arbitrarily chosen as follows:

$$\theta = 1650 \text{ K} \qquad p = 10 \text{ Torr}$$

$$\chi_{WF_6} = 0.3 \qquad \chi_{H_2} = 0.7$$

$$\chi_{WF_4} = 0.0 \qquad \chi_{HF} = 0.0$$

$$\chi_{WF_5} = 0.0 \qquad \chi_{Ar} = 0.0.$$

It was found that, at 10 Torr, the transport rates due to diffusion were sufficiently greater than the reaction rates that the assumption that the gas was homogeneous, viz. perfectly stirred, was reasonable. The initial site fractions of the surface species were

$$z_{H(1)(S)} = 2.457 \times 10^{-9} \qquad z_{H(2)(S)} = 5.345 \times 10^{-2}$$

$$z_{WF_6(2)(S)} = 2.110 \times 10^{-3} \qquad z_{WF_5(2)(S)} = 1.798 \times 10^{-7}$$

$$z_{WF_4(2)(S)} = 1.532 \times 10^{-6} \qquad z_{WF_3(2)(S)} = 3.994 \times 10^{-13}$$

$$z_{F(1)(S)} = 6.631 \times 10^{-1} \qquad z_{F(2)(S)} = 2.106 \times 10^{-4}$$

$$z_{F(1)(S)} = 8.966 \times 10^{-14} \qquad z_{VW} = 2.811 \times 10^{-1}.$$

The site fractions were determined from a computer code to determine equilibrium site fractions at a given temperature, pressure, and gas phase composition (Coltrin et al., 2000). The PSR model also requires as an input the ratio of the reactive surface area to the total volume of the reactor, $(A/V)_{sys}$. From the reactor dimensions given above, $(A/V)_{sys} = 0.4$.

Assuming uniform deposition, the areal density of the tungsten film, ρ''_W can be computed from the initial conditions and the stoichiometry of the reaction. The areal density is the mass of the solid film per unit area, and is calculated as follows:

$$\rho''_W = \frac{n_W w_W}{A}, \tag{6.8}$$

where n_W is the number of moles of tungsten deposited. From the ideal gas law, the

total number of moles of WF_6 initially is

$$\begin{aligned} n_{WF_6} &= \chi_{WF_6}\frac{pV}{\mathcal{R}\theta} \\ &= 0.3\frac{(10/760)\,\text{atm}\,(100)(1)\,\text{cm}^3}{(82.06)\,\text{cm atm mol}^{-1}\,\text{K}^{-1}\,(1650)\,\text{K}} \\ &= 2.915\times10^{-6}\ \text{mol (per unit depth).} \end{aligned} \tag{6.9}$$

From the stoichiometry of the overall reaction, it is clear that 1 mole of WF_6 reacts for every 3 moles of H_2. Since the H_2 is present in excess, only $0.7/(3\times0.3) = 77.78\%$, or 2.267×10^{-6} mol of WF_6 is converted to solid tungsten. From the stoichiometry of the reaction, the number of moles of solid tungsten deposited is equal to the number of moles of WF_6 reacted. Thus, the areal density of the tungsten film at the completion of the reaction is

$$\begin{aligned} \rho''_W &= \frac{(2.267\times10^{-6})\,\text{mol}\,(185.83)\,\text{g mol}^{-1}}{(40)(1)\text{cm}^2} \\ &= 1.04\times10^{-5}\,\text{g cm}^{-2} \end{aligned}$$

A comparison of the PSR and CVD batch model numerical solutions is shown in Fig. (6.3). In this figure, the areal density of the tungsten film is plotted versus time. From the figure, the reaction reached near completion at time $t \approx 0.05$ s, by which time 99.9% of the H_2 had disappeared. The film density at $t = 0.05$ s of the PSR and batch CVD models were 1.010×10^{-5} and 1.025×10^{-5} g cm^{-2}, respectively, a difference of only 1.4%. The final pressure in the PSR and CVD batch models was 14.94 and 14.74 Torr, respectively, a difference of 1.3%. The pressure increase was due to the increase in the number of moles as the reaction proceeded, as indicated by the overall reaction.

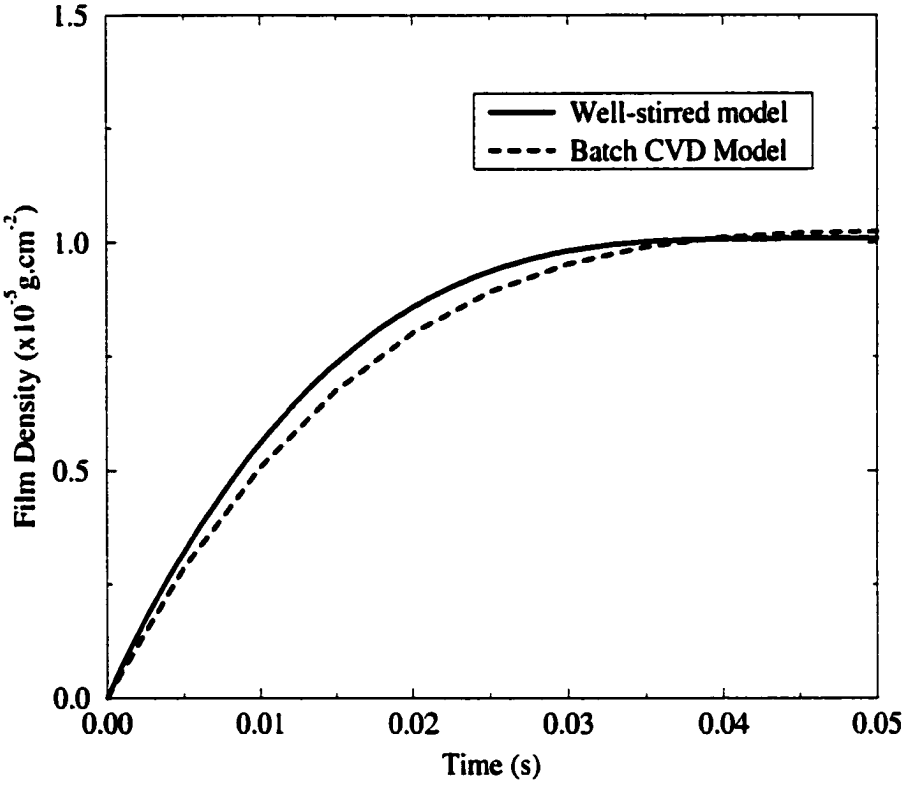

Figure 6.3: Comparison of the batch CVD model of this work and the isothermal well-mixed batch reactor model from Coltrin et al. (1996).

6.2 Natural Convection in Batch Reactors

6.2.1 Transient and Steady-state Natural Convection in a Heated Cavity

Transient Convection in a Cavity Heated from Below

Natural convection was simulated in a 10 cm × 10 cm square cavity, in which the bottom was maintained at a constant temperature and the sides and top were maintained at a constant, but lower temperature. The grid for this domain, shown in Fig. (6.4), consists of 51 × 51 grid lines. An inverse hyperbolic tangent stretching function is used to concentrate grid lines near the walls (Henshaw, 1999a). The grid resolution and stretching was chosen to reduce spatial truncation error and to obtain better solution accuracy near the corners. With this grid resolution, the solutions were grid-independent. That is, that further refinement did not significantly change the solution.

The composition of the gas was a 90%/10% (by mole fraction) mixture of H_2 and WF_6 at 300 K. The temperature of the bottom wall for $t > 0$ was 350 K. The other walls were maintained at 300 K. A simulation was conducted for $0 \leq t \leq 10.0$ s, and the time step was 0.01 s. For these conditions, the Rayleigh number was 98,000.

At this Rayleigh number, the flow is unsteady and oscillatory. The time evolution of the path lines in the flow are shown in Fig. (6.5) and the isotherms are shown in Fig. (6.6). The temperature gradient at the intersection of the hot and cold walls created a buoyancy roll which shed from the corner and moved into the center of the rising plume. The plume then collapsed the cell. The frequency of the shedding of these rolls was approximately 2.4 s. The maximum speed of the plume was approximately 38 $\mathrm{cm\,s^{-1}}$, although it was not constant due to the oscillatory nature of the flow. This example clearly illustrates the importance of solving the unsteady equations of motion.

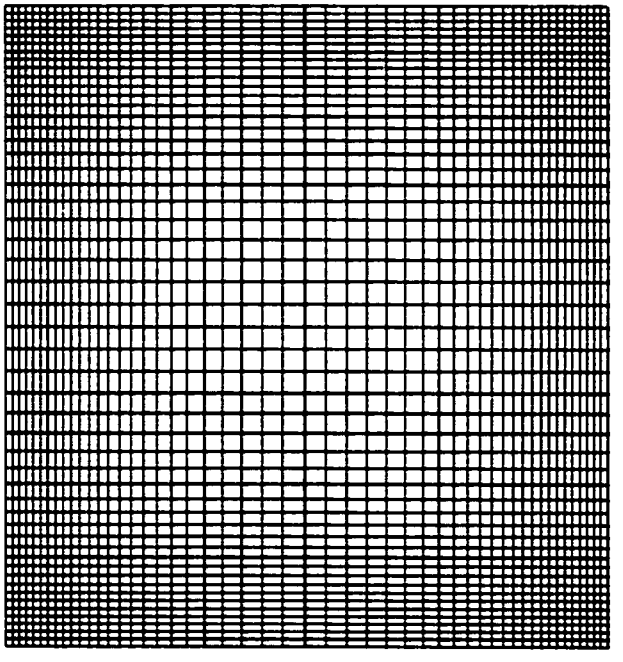

Figure 6.4: The grid used to model natural convection in a heated cavity heated from below. The length of the sides of the square are 10 cm.

Steady-state Convection in a Cavity Heated from Below

Vortex shedding frequency decreased as the Rayleigh number decreased. A simulation at $\mathbf{Ra} = 16,000$, corresponding to a system pressure of 100 Torr, yielded a steady-state solution. The streamlines and isotherms of the flowfield are shown in Fig. (6.7). The maximum speed of the plume was 25 $\mathrm{cm\,s^{-1}}$. The point of maximum speed was near the geometric center of the domain.

The onset of the oscillatory motion was investigated parametrically. The maximum fluid speed was computed for several values of system pressure. The onset of the instability was found to be very gradual. A slight oscillation in the temperature field was noticeable at $p = 75$ Torr, or $\mathbf{Ra} = 9 \times 10^3$. The intensity of the oscillations increased as the pressure increased. The first evidence of vortex shedding was noticeable at $p = 175$ Torr, or $\mathbf{Ra} = 48,000$.

The vortex shedding phenomenon results from the instabilities that evolve from the nonlinear terms in the governing equations. At low Rayleigh numbers, when the solution reaches a steady state, the magnitude of perturbing terms is smaller than the linear contribution to the solution. This solution may not be unique, since the solution depends upon its its trajectory through the solution space. The validity of a solution can be reasonably justified if the same steady state is attained by a variety of equivalent initial conditions which result in different solution trajectories to the same steady state solution. An equivalent initial condition implies that the same total mass, energy, and momentum of the system is the same. At larger Rayleigh numbers, the solution is unsteady, but oscillatory. In addition, the solution may not be unique.

Multicomponent Natural Convection in a Cavity Heated from Below

In the previous two studies, only the energy, momentum, continuity, and pressure update equations were solved. It was assumed that the species composition was uniform. In this next study, the species equations are solved in order to determine

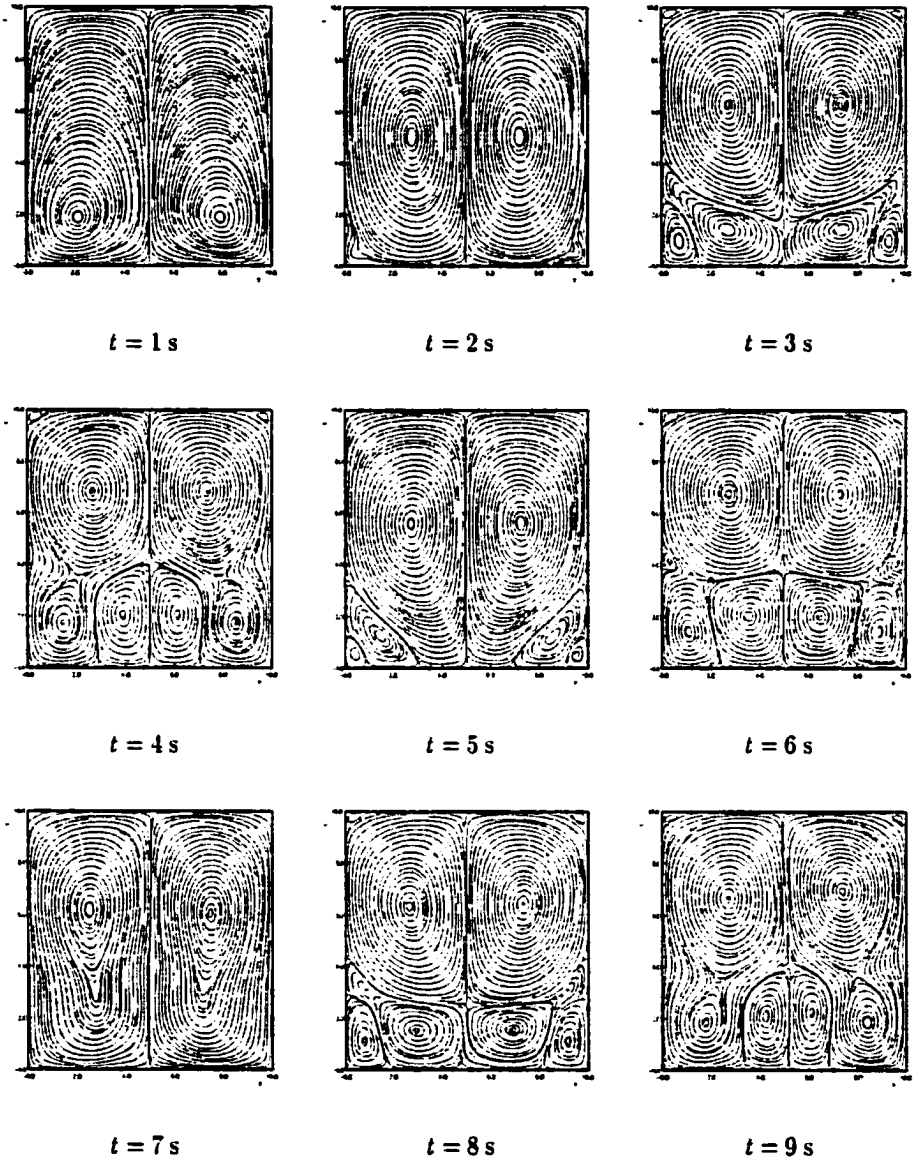

Figure 6.5: Evolution of pathlines in a square cavity heated on the bottom. The temperature of the bottom wall was 350 K and the temperature of the sides and the top was 300 K. The pressure was 250 Torr. The maximum fluid speed was speed was 38 $\mathrm{cm\,s^{-1}}$. The period of the buoyancy rolls was approximately 2.4 s.

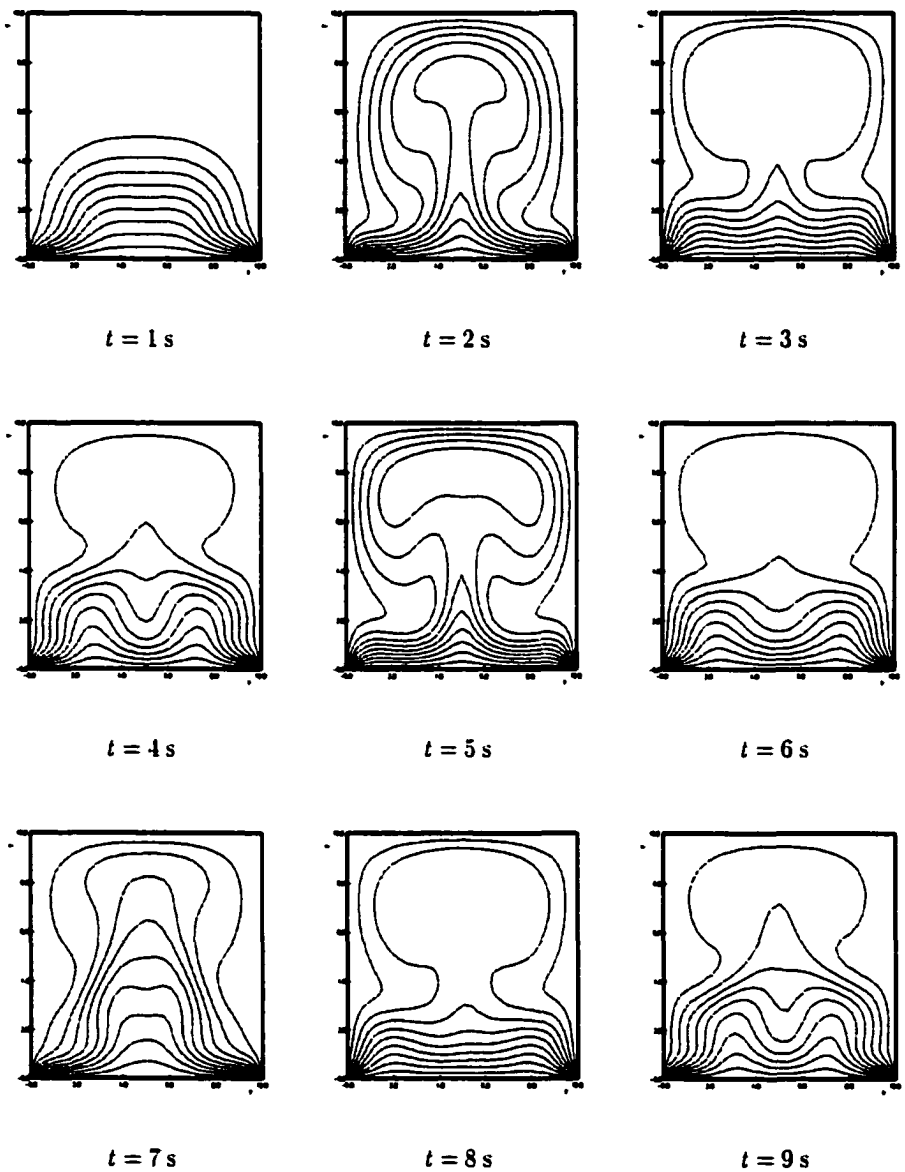

Figure 6.6: Evolution of isotherms in a square cavity heated on the bottom. The temperature of the bottom wall was 350 K and the temperature of the sides and the top was 300 K. The pressure was 250 Torr. The maximum fluid speed was speed was 38 $\mathrm{cm\,s^{-1}}$. The period of the buoyancy rolls was approximately 2.4 s.

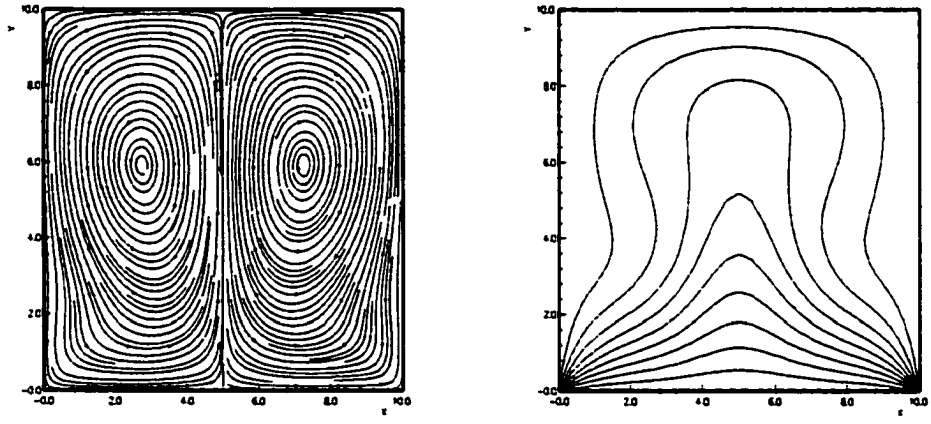

(a) (b)

Figure 6.7: The steady state solution in a square cavity heated on the bottom for $\mathsf{Ra} = 16,000$ shown as (a) streamlines and (b) isotherms. The cold wall temperature was 300 K and the hot wall (bottom) temperature was 350 K. The pressure was 100 Torr. The maximum fluid speed was 24 $\mathrm{cm\,s^{-1}}$.

the effects of varying composition fields, due to phenomena such as thermal diffusion, on the convective flows inside a bottom-heated square cavity.

A study was performed with a 90%-10% mixture (by mole fraction) of H_2 and WF_6 initially at 300 K and 50 Torr. The bottom surface temperature was maintained at 350 K for $t > 0$ and the cold surfaces were maintained at 300 K. These conditions can be used to show that $\mathsf{Ra} = 5,000$. In addition, the temperature discontinuity in the lower corners, which was present in the previous two simulations, was removed by imposing a linear temperature transition at the surfaces where $0 \leq y \leq 2$ cm, with y pointing upward.

The steady-state solution is shown in Fig. (6.8). In this figure, four plots are presented: (a) streamlines, (b) isotherms, and (c-d) lines of constant mass fraction of WF_6. In Fig. (6.8a), the streamlines indicate a general circulation similar to that of the previous example. The maximum fluid speed was 18.3 $\mathrm{cm\,s^{-1}}$ and occurred

near the geometrical center of the domain. The isotherms in Fig. (6.8b) clearly indicate the relative size of the thermal plume. The isotherms are uniformly spaced between 300 K and 350 K. The thermal gradients in the lower left-hand and right-hand corners caused heavy species (WF_6) to diffuse towards the lower portion of the right and left surfaces. In Fig. (6.8c), the mass fraction of WF_6 varied between $0.906 \leq \psi_{WF_6} \leq 0.104$, with the minimum value occurring at the center of the bottom surface. The maximum value occurred at the left and right surfaces at the location $y \approx 2$.

In this case, thermal diffusion enhanced natural convection by driving the heavy species upwards and outwards towards the regions that were already dense due to the temperature variation in the reactor. Since the molecular weight of WF_6 is 147.7 times that of H_2, the local density in these regions is greater than if the thermal diffusion was not present. This study shows that thermal diffusion can significantly affect both the composition and velocity fields, especially in systems with large thermal diffusion coefficients, which result when there is a large disparity in the molecular weights of the species. When this problem was solved neglecting the species equations, the maximum fluid speed was 12.7 $cm\,s^{-1}$, a decrease of 30.6%.

The conditions at the upper surface were nearly uniform. This was a result of the stagnation flow that developed inside the reactor. An exploded view of the mass fraction isocontours near the stagnation point on the upper surface is shown in Fig. (6.8d). The variation in the surface mass fraction of WF_6 was less than one part in ten-thousand. Thus, if deposition rates were computed, they would also be nearly uniform.

In Section 1.3, it was mentioned that this model could be used in the fundamental design process of a batch CVD reactor or as a tool to assess the feasibility of converting a continuous flow CVD reactor to batch mode. In both of these applications, it is important to determine the operating conditions, if any, that yield

uniform conditions at the deposition surface. This study demonstrates that it is possible to generate uniform surface composition conditions in a CVD batch reactor, even when the flowfield is not uniform.

6.2.2 Natural Convection in Tilted Square Cavity

The effect of susceptor orientation was studied by varying the tilt angle of the reactor. The grid from the previous section was used for the simulations, except that the domain was rotated 45 degrees.[1] Two studies were conducted. In the first study, the temperature of the lower-left wall was 400 K and the upper-right wall was 300 K. The other two walls were adiabatic. In the second study, the locations of the hot and cold walls were switched, viz., the hot wall was nearer the top of the reactor. The system pressure was 64 Torr and the initial temperature was 350 K.

By heating the reactor near the top, one would expect that the fluid velocities to be lower in magnitude, since the density field is more dynamically stable. The results of the simulation bear this out. In Fig. (6.9), the evolution of pathlines and isotherms are shown for the case of the tilted reactor heated on the lower-left edge. The steady state maximum fluid speed was 31 $\mathrm{cm\,s^{-1}}$, and the flow direction was clockwise. In Fig. (6.10), the evolution of pathlines and isotherms is shown for the case of the tilted reactor heated on the upper-right edge. The steady state maximum fluid speed was 12 $\mathrm{cm\,s^{-1}}$, and the flow direction was counter-clockwise. When the square cavity (not rotated) with adiabatic sides was heated from the top, the density field was dynamically stable, and the fluid was static. This result is not shown.

[1] An alternative method would have been to rotate $\boldsymbol{g}$.

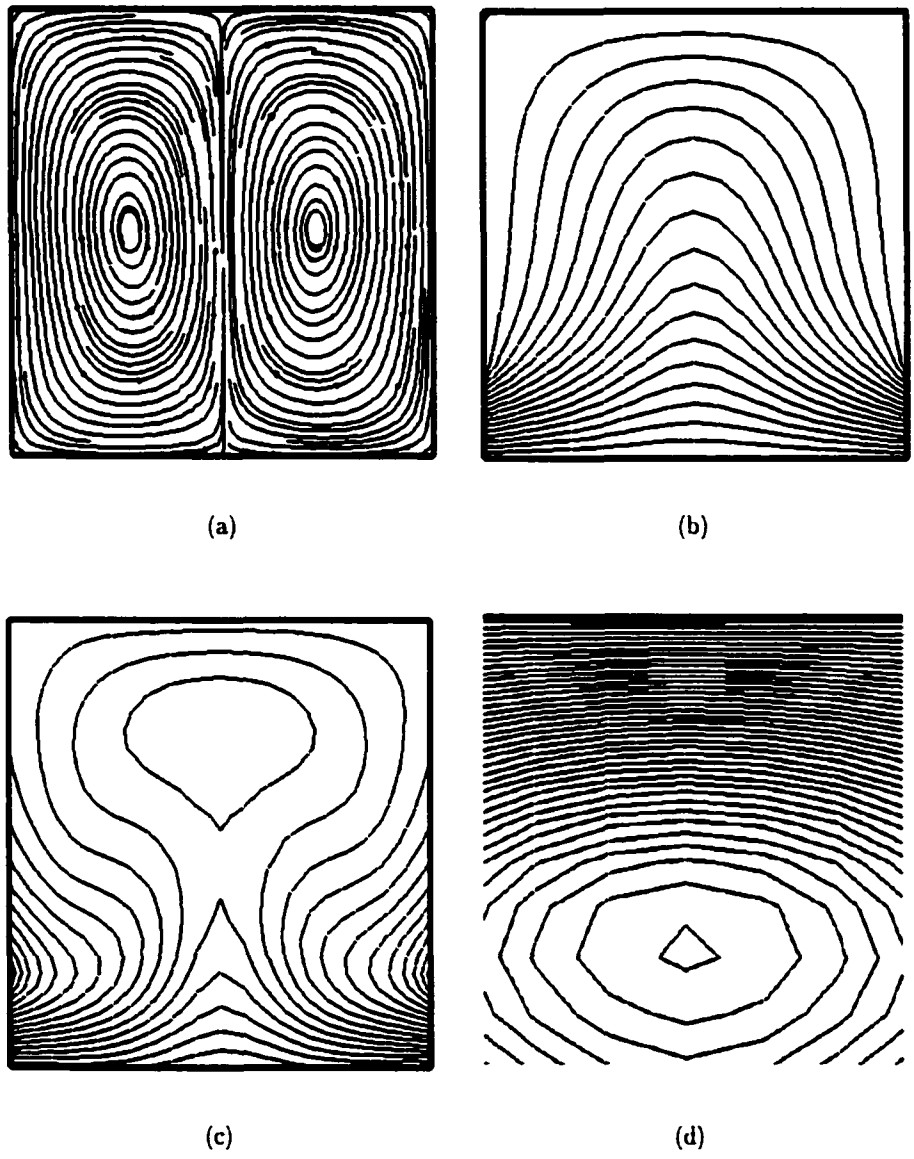

Figure 6.8: Steady-state multicomponent natural convection in a square cavity heated at the bottom. Figures include (a) streamlines, (b) isotherms, and (c-d) lines of constant ψ_{WF_6}. The maximum fluid speed was 18.3 $cm\,s^{-1}$. The lower wall was maintained at 350 K, and the upper edges at 300 K, with a linear transition in the region $0 \leq y \leq 2$ cm, with y pointing upwards. The value of ψ_{WF_6} was $0.906 \leq \psi_{WF_6} \leq 0.104$, with the lowest mass fraction occurring at the center of the bottom surface. In (d), the mass fraction isocontours are shown in an exploded view near the upper stagnation point.

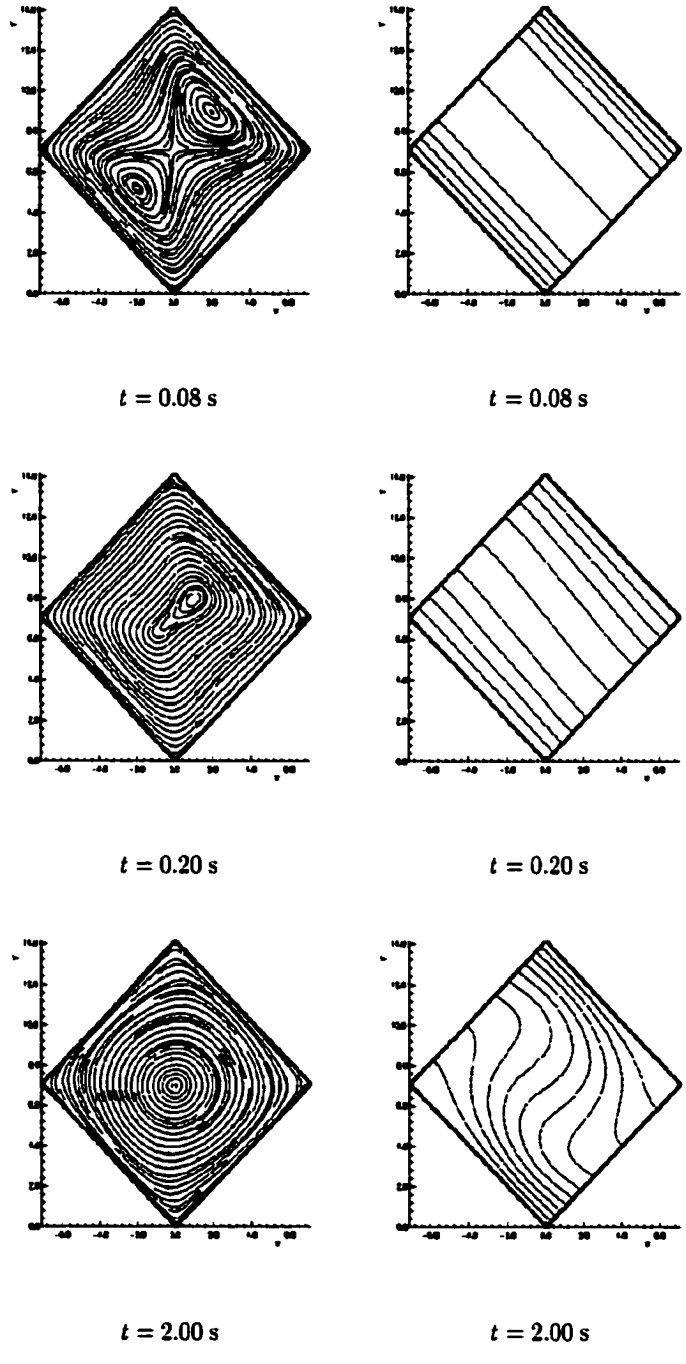

Figure 6.9: Evolution of pathlines and isotherms in a tilted square cavity. The temperature of the lower left edge is 400 K, and the temperature of the upper right edge is 300 K. The other walls are adiabatic. The initial temperature and pressure was 350 K and 64 Torr, respectively. The maximum fluid velocity was 31 $\mathrm{cm\,s^{-1}}$. The flow direction is clockwise.

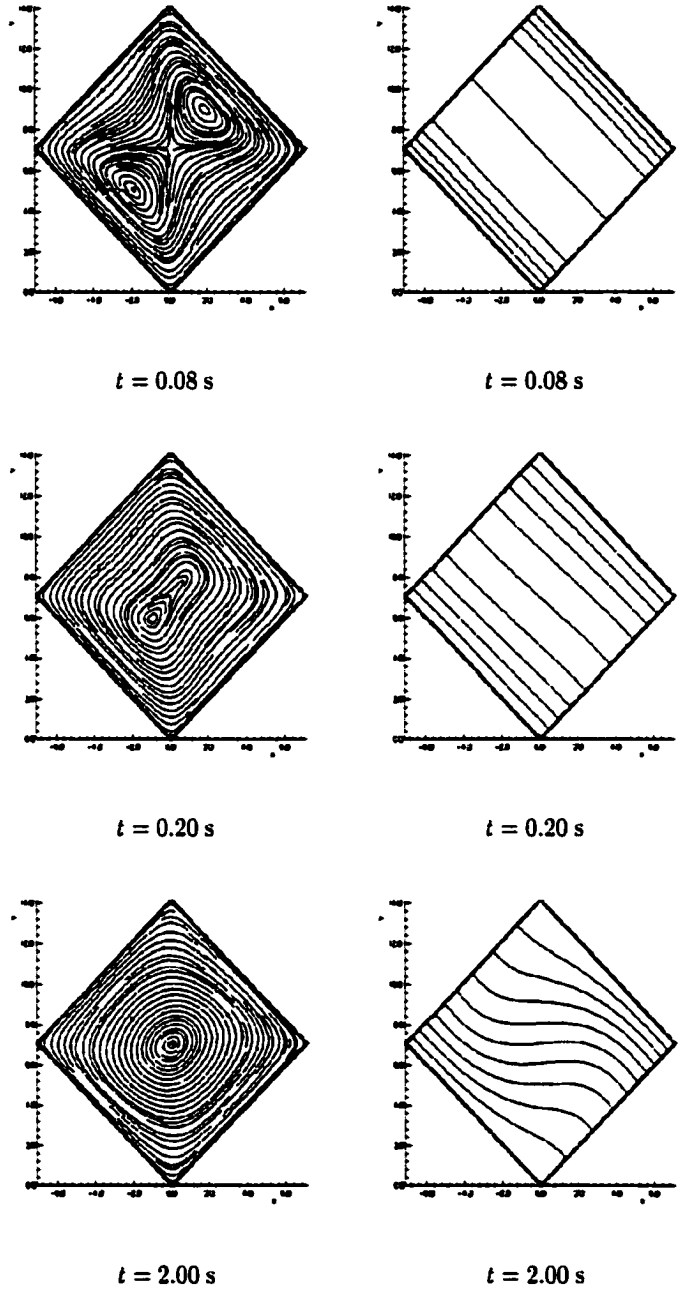

Figure 6.10: Evolution of pathlines and isotherms in a tilted square cavity. The temperature of the upper left edge is 400 K, and the temperature of the lower right edge is 300 K. The other walls are adiabatic. The initial temperature and pressure was 350 K and 64 Torr, respectively. The maximum fluid speed was 12 $\mathrm{cm\,s^{-1}}$. The flow direction is counter-clockwise.

6.2.3 CVD of Tungsten in a 3-D Geometrically Complex Reactor

Problem Description

Tungsten CVD was studied in a cylindrical reactor. A schematic of the reactor is shown in Fig. (6.11). The reactor diameter was 20 cm, and the height was 5 cm. The susceptor was 9 cm in diameter and located on the upper surface of the reactor. The bottom surface of the susceptor was flush with the inner surface of the top of the reactor. In order to make the problem truly three-dimensional, the center of the susceptor was offset from the axis of rotation of the reactor.

The Composite Grid

The composite grid used to discretize the domain consisted of 4 component grids. There were 23,055 discretization points, 4,530 interpolation points, and 9,345 unused points. The unused points, or holes, were points that removed by the interpolation algorithm and not used in the solution of the differential equations. A top view and perspective view of the composite grid is shown in Fig. (6.12). In this figure, the boundaries of the susceptor and nonreactive reactor surfaces are colored dark and light gray, respectively. Also, to illustrate the location of the component grids, the component grid boundaries are highlighted with various colors.

Operating Conditions

The reaction mechanism for this CVD system is the same as in the previous section. The operating conditions were the following:

$$\theta_{\text{susceptor}} = 650 \text{ K}$$

$$\theta_{\text{reactor walls}} = 350 \text{ K}$$

$$p = 10 \text{ Torr.}$$

The initial gas phase mole fractions and surface species site fractions are the same as those given in the previous tungsten CVD study.

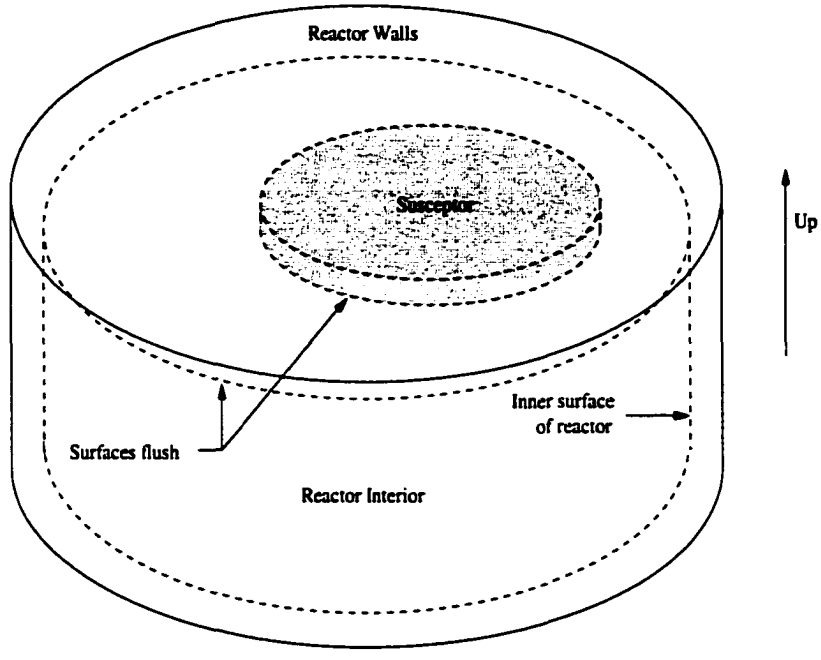

(a)

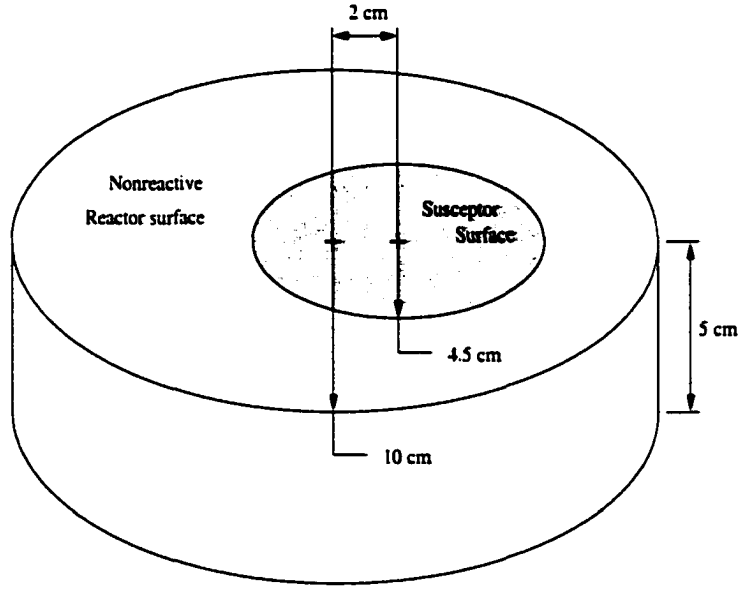

(b)

Figure 6.11: (a) Schematic of a 3-dimensional cylindrical reactor with the center of the susceptor offset from the center of the reactor and (b) a dimensioned drawing of the interior surfaces of the reactor.

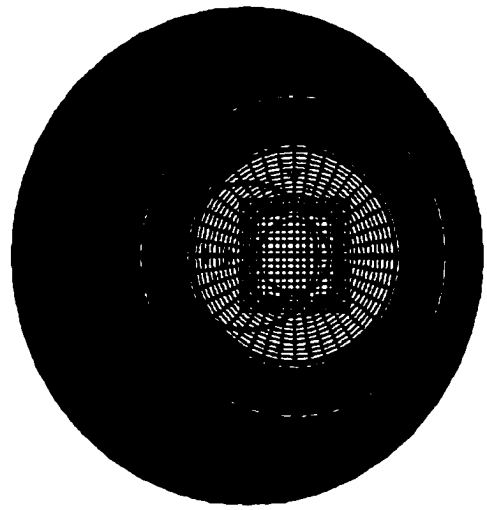

(a)

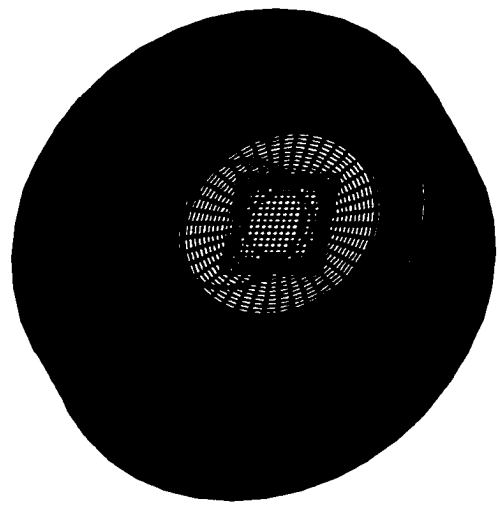

(b)

Figure 6.12: (a) Top view and (b) perspective view of the 3-dimensional composite grid of a CVD batch reactor showing the grid lines on the boundary surfaces. The susceptor and nonreactive wall surfaces are colored dark and light gray, respectively. Boundaries of component grids are colored to indicate the relative position of each component grid.

Results—Temperature, Concentration, Velocity Profiles

The solution at $t = 1$ s is shown in Figs. (6.13)-(6.16). In Fig. (6.13), isotherms are shown on the $x - z$ plane and $y - z$ planes. The steady state temperature distribution was reached at $t \approx 0.2$ s, due to the high thermal diffusivity. Fig. (6.14) shows the contours of the mass fraction of WF_6 in the reactor. Thermal diffusion caused transport of WF_6 towards the cold surfaces of the reactor. Thermal diffusion of H_2 (not shown) caused transport of H_2 towards the susceptor. The contours of dynamic pressure are shown in Fig. (6.15). The absolute value of this quantity is not important, since only its gradient appears in the momentum equation. The maximum value of the dynamic pressure occurred at the substrate surface.

The general circulation of the flowfield in the reactor is illustrated by pathlines shown in Fig. (6.16). The fluid motion in the reactor was directed upwards in the center, radially outward near the upper surface, downward near the outer edges, and radially inward near the bottom surface. The flowfield was symmetric about the $y - z$ plane, but not axisymmetric, due the wafer offset. The maximum fluid speed was $10.8\ \mathrm{cm\,s^{-2}}$. The Grashof number was approximately equal to

$$\mathrm{Gr} = 9.3 l_c^3. \tag{6.10}$$

Therefore, if the characteristic length is based on the height of the reactor, $\mathrm{Gr} = 1200$. If the characteristic length is based on the distance over which the velocity changes from minimum to maximum, then, from Fig. (6.16), $l_c \approx 1$ cm, and $\mathrm{Gr} = 9$. In either case, the magnitude of the Grashof number was not small enough to be considered negligible for the operating conditions in the reactor. The fluid motion resulted from the close proximity of the cold and hot surfaces at the top of the reactor. Considering the region in the gas near the interface between the susceptor and the cold wall, it is evident why the general motion was radially outward at the upper surface. The temperature gradient, and thus the density gradient, in this region was almost purely radial, with the density at a minimum near the susceptor. The hot

fluid in the interfacial region rose and the cold fluid sank, which evolved into a gentle circulation in the interfacial region, which then expanded to encompass the entire physical domain.

Results—Discussion of Transient Film Deposition and Near-Surface Composition

In Section 1.3, it was mentioned that of the industrial applications for this code is as a tool for fundamental CVD batch system design. One important issue in CVD reactor design is film uniformity. While it is not always necessary to have uniform film growth, it is usually necessary to precisely control the film growth as a function of position on the deposition surface. In this section, the transient deposition profiles and near-surface concentrations of one of the reactant gases are plotted at the wafer surface. It is this type of information from the model that could be invaluable to the reactor designer.

The deposition of tungsten on the wafer is shown in Figs. (6.17) and (6.18). In both of these plots, the areal density of tungsten, in $\mathrm{g\,cm^{-2}}$, is plotted along the line generated by the intersection of the wafer surface with the $x-z$ plane. In Fig. (6.17), the tungsten film density is shown for various times. The numbers on the curves are the simulation times. The relative spacing between the film thickness can be used to estimate the average growth rate. From the figure, it is evident that during the simulation, the mean growth rate decreased by approximately 20%. The shape of these curves is shown more clearly in Fig. (6.18). Here, the film density at several times is plotted relative its value at the left edge of the wafer, identified by the coordinates $(-2.5, 0, 5)$ cm, where the location of the axis of symmetry of the reactor is at $x = 0$. Due to the asymmetry of the problem resulting from the wafer placement offset from the axis of symmetry of the reactor, the deposition profile is not symmetric about the axis of symmetry of the wafer. The maximum film uniformity is approximately 1% at the end of the simulation. This small variation is due to the fact that the

(x-z plane)

(y-z plane)

Figure 6.13: Gas temperature in a 3-D cylindrical batch CVD reactor at $t = 1.0$ s.

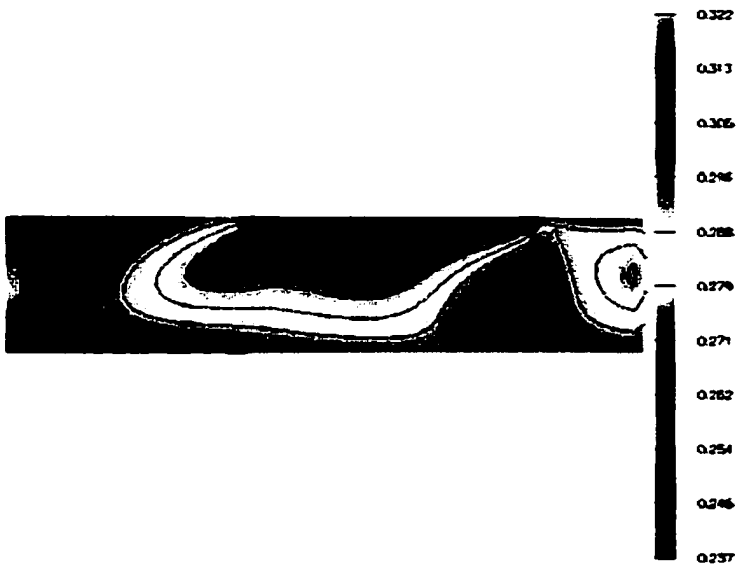

(x-z plane)

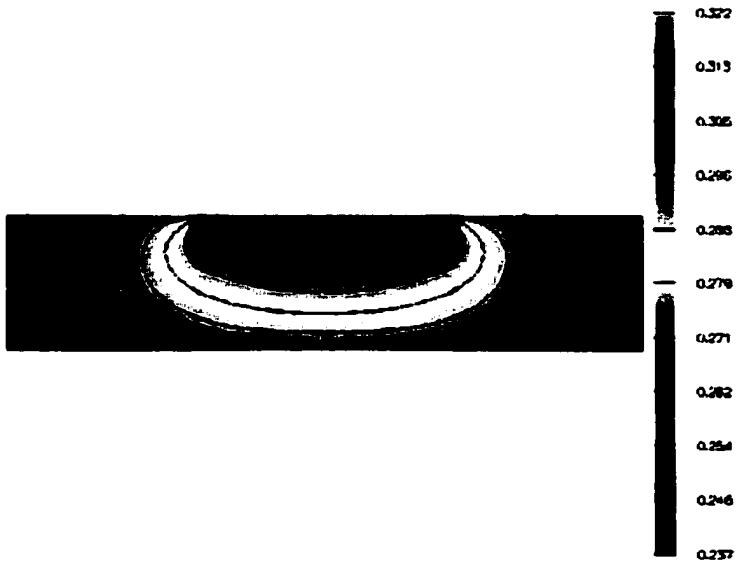

(y-z plane)

Figure 6.14: Mole fraction of WF_6 in a 3-D cylindrical batch CVD reactor at t = 1.0 s.

(x-z plane)

(y-z plane)

Figure 6.15: Dynamic pressure (dyne cm^{-2}) in 3-D cylindrical batch CVD reactor at $t = 1.0$ s.

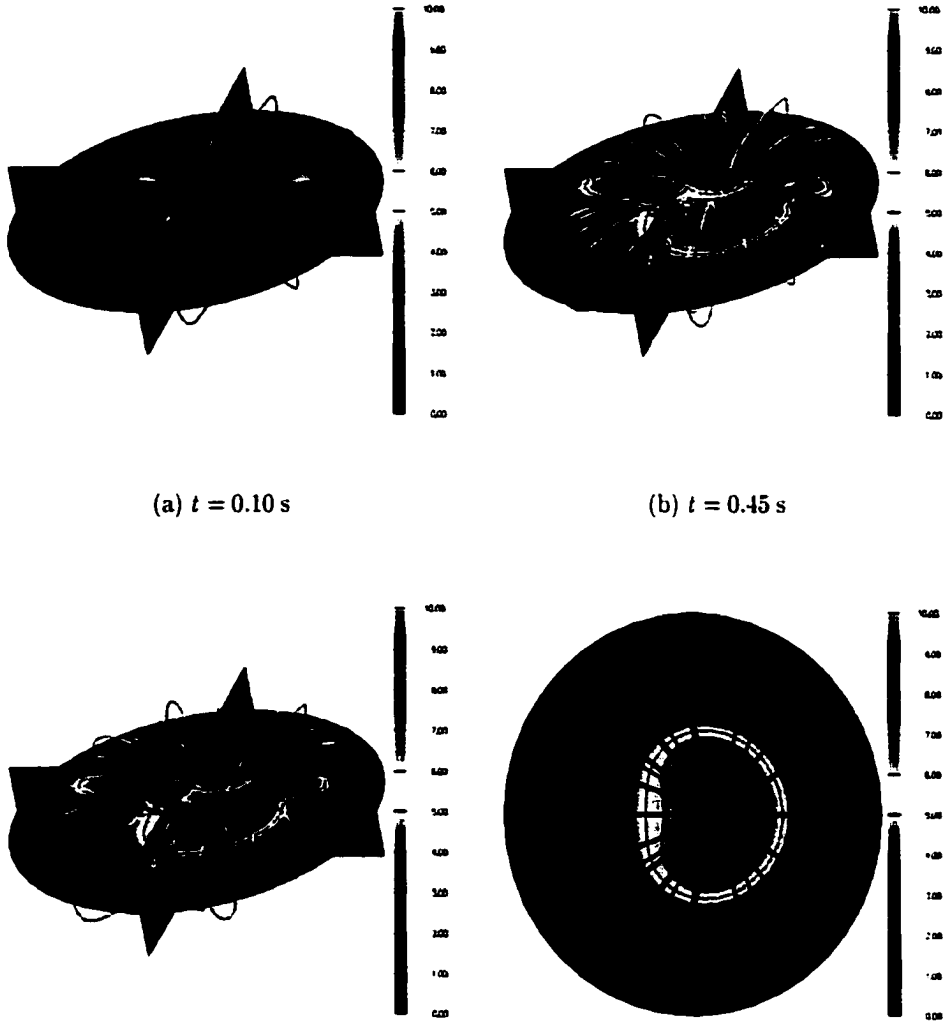

(a) $t = 0.10$ s

(b) $t = 0.45$ s

(c) $t = 1.00$ s

(d) $t = 1.00$ s (top view)

Figure 6.16: Streamlines in a 3-D cylindrical batch CVD reactor at different times in the reactor. The first three figures (a-c) are perspective views showing both the streamlines (colored to indicate fluid speed) and cutting planes with contours of gas speed. The last figure (d) shows streamlines (colored black) and contours of gas speed ($\mathrm{cm\,s^{-2}}$) in the horizontal (x-y) plane through the center of the reactor.

system operating pressure was low, and the surface temperature was assumed constant. The low pressure conditions approximated a perfectly-stirred reactor. Thus the near-surface concentrations were very uniform. Since the temperature of the deposition surface was constant, the deposition rates were also very uniform. It is also clear from the figure that the nonuniformity of the film increased during the simulation.

The near surface mass fractions of one of the gas-phase species is plotted in a similar manner as the two previous plots. This is done to show the evolution of the concentration profiles as may be needed to analyze the efficacy of a particular reactor geometry. In this case, a reactant species, WF_6, is arbitrarily chosen to illustrate the surface composition variation. In Fig. (6.19), the time evolution of ψ_{WF_6} shows a decrease of this reactant versus time. In Fig. (6.20), the nonuniformity is illustrated by plotting the surface mass fraction referenced to its value at the left edge of the wafer, as in Fig. (6.18). From this figure, it is evident that the nonuniformity changes dramatically during the initial deposition, but changes more slowly at later times. This is likely due to the field establishing a quasi-steady flux of species to the surface. The establishment of this quasi-steady state is due to the fact that the deposition rates are extremely slow compared to diffusion transport.

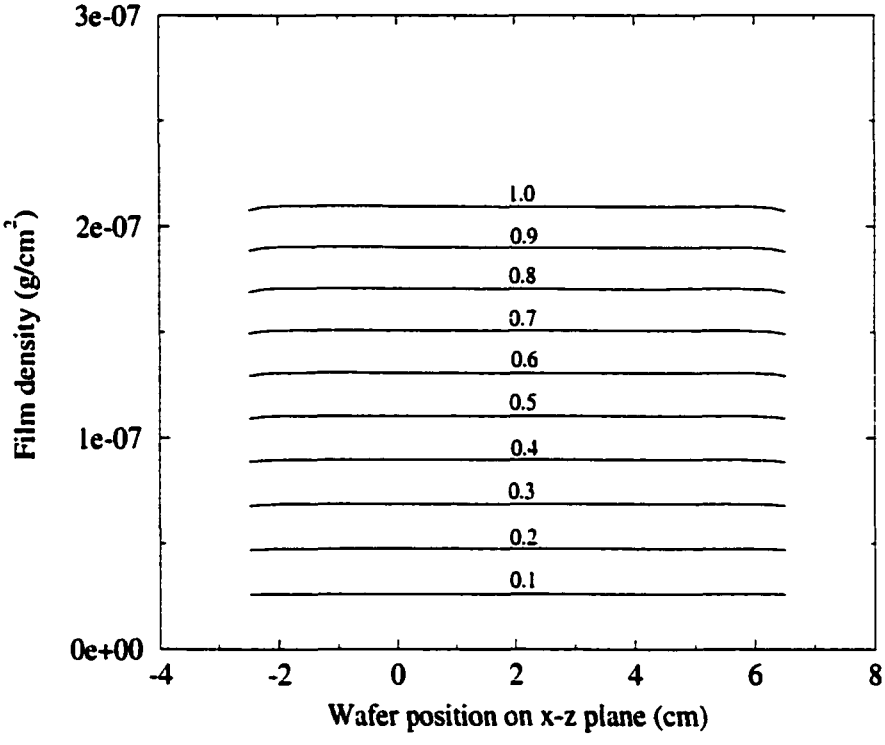

Figure 6.17: Areal density of deposited tungsten ($g\,cm^{-2}$) at the intersection of the wafer surface and the $x - z$ plane. The numbers on the curves are the simulation time.

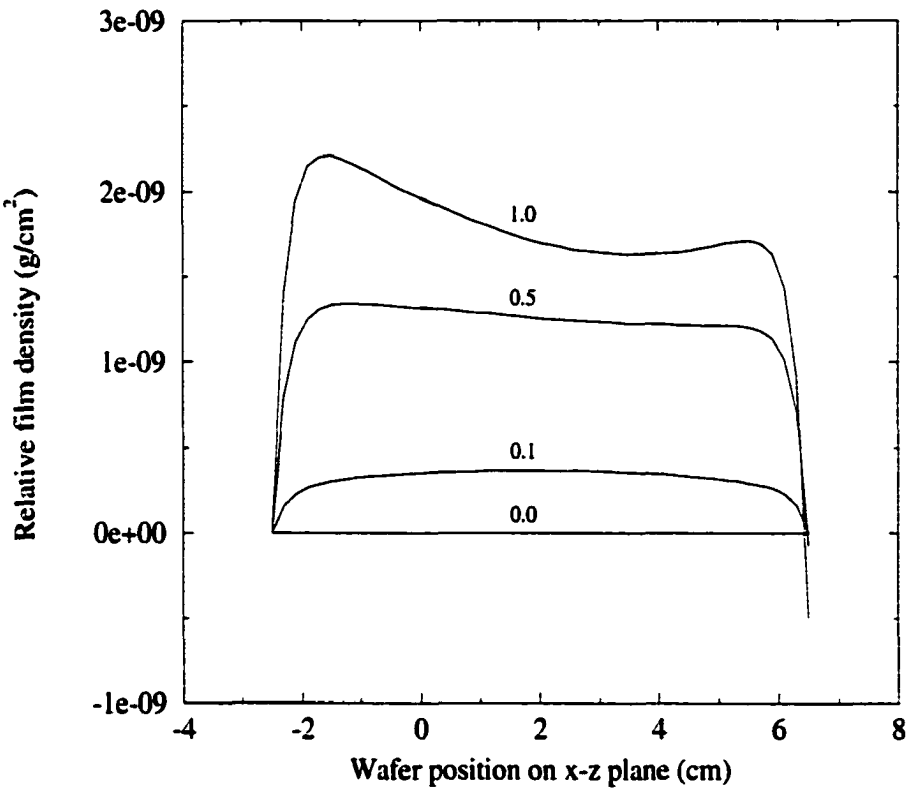

Figure 6.18: Areal density of deposited tungsten ($g\,cm^{-2}$) at the intersection of the wafer surface and the $x - z$ plane plotted relative to its value at the left-edge of the wafer. The numbers on the curves are the simulation time.

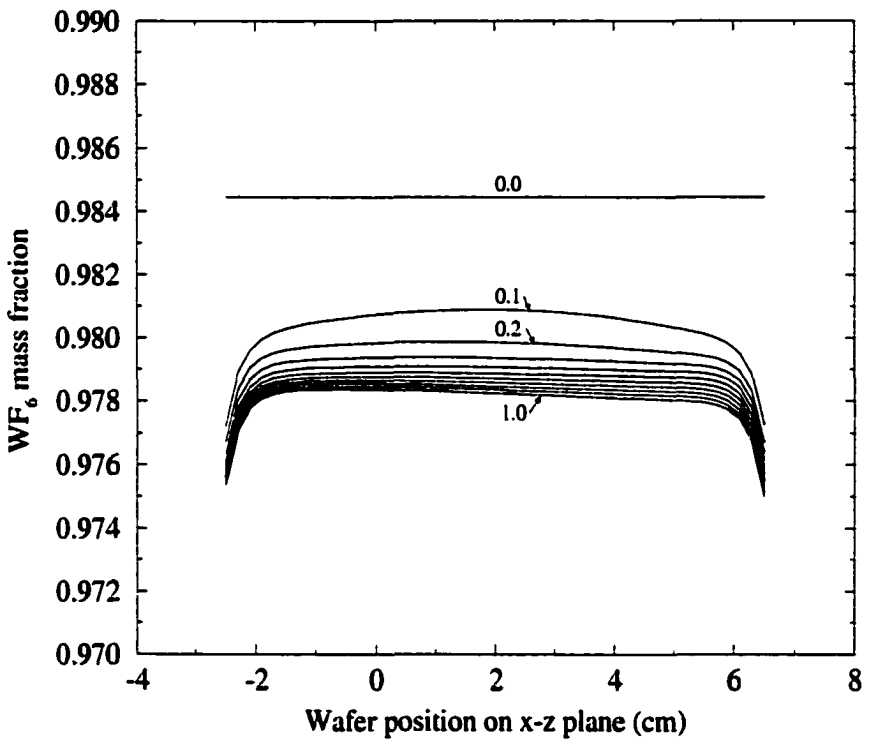

Figure 6.19: Surface mass fraction of gaseous WF_6 at the intersection of the wafer surface and the $x - z$ plane. The numbers on the curves are the simulation time.

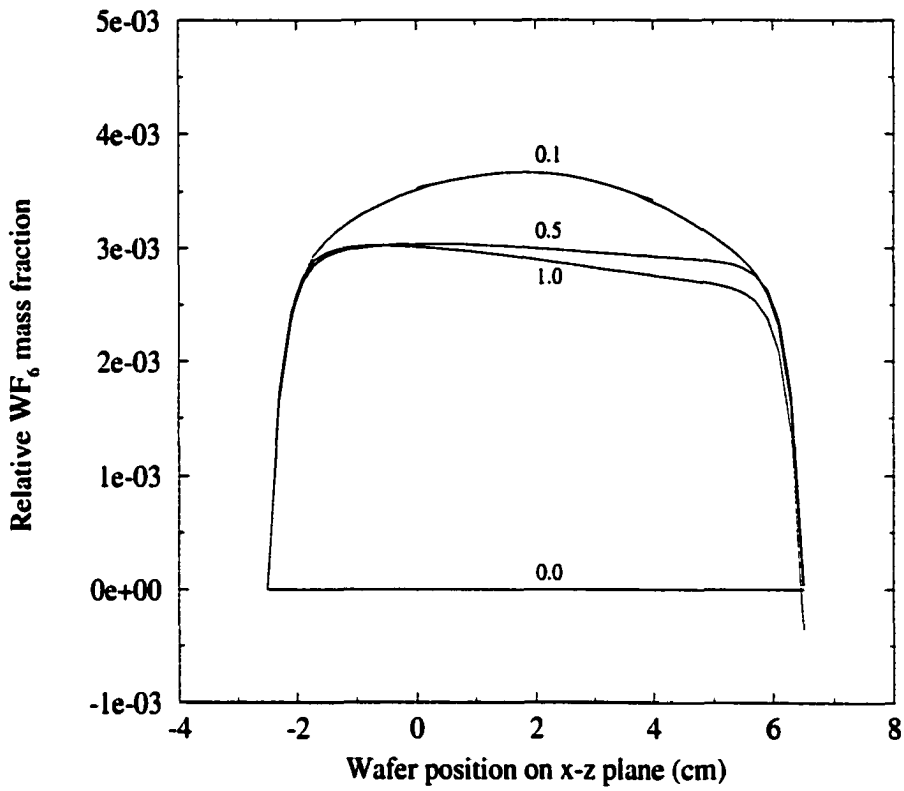

Figure 6.20: Surface mass fraction of gaseous WF_6 at the intersection of the wafer surface and the $x - z$ plane plotted relative to the its at the left-edge of the wafer. The numbers on the curves are the simulation time.

Table 6.3: Heterogeneous Reactions in CVD of Diamond: $k = A\theta^b \exp(-E/\mathcal{R}\theta)$.

	REACTION	A	b	E
1.	CH(S)+H<=>C(S,R)+H2	1.00E-01	0.0	0.0
	Coefficients are sticking parameters...			
2.	C(S,R)+H<=>CH(S)	1.00E+00	0.0	0.0
	Coefficients are sticking parameters...			
3.	C(S,R)+C<=>D+C(S,R)	3.30E-01	0.0	0.0
	Coefficients are sticking parameters...			
4.	C(S,R)+CH<=>D+CH(S)	3.30E-01	0.0	0.0
	Coefficients are sticking parameters...			
5.	C(S,R)+CH2<=>D+CH(S)+H	3.30E-01	0.0	0.0
	Coefficients are sticking parameters...			
6.	C(S,R)+CH3<=>D+CH(S)+H2	3.30E-01	0.0	0.0
	Coefficients are sticking parameters...			
	Motz-Wise correction used on sticking coeffs.			

Table 6.4: Homogeneous Reactions in CVD of Diamond: $k = A0^b \exp(-E/\mathcal{R}0)$.

	REACTION	A	b	E
1.	2CH3(+M)=C2H6(+M)	9.03E+16	-1.2	654
	Low pressure limit:	3.18E+41	-7.03	2726
	TROE centering:	6.04E-01	6927	132
	H2 Enhanced by	2.00E+00		
2.	CH3+H(+M)=CH4(+M)	6.00E+16	-1	0
	Low pressure limit:	8.00E+26	-3	0
	H2 Enhanced by	2.00E+00		
3.	CH4+H=CH3+H2	2.20E+04	3	8750
4.	CH3+H=CH2+H2	9.00E+13	0	15100
5.	CH2+H=CH+H2	1.00E+18	-1.6	0
6.	CH+H=C+H2	1.50E+14	0	0
7.	CH+CH2=C2H2+H	4.00E+13	0	0
8.	CH+CH3=C2H3+H	3.00E+13	0	0
9.	CH+CH4=C2H4+H	6.00E+13	0	0
10.	C+CH3=C2H2+H	5.00E+13	0	0
11.	C+CH2=C2H+H	5.00E+13	0	0
12.	C2H6+CH3=C2H5+CH4	5.50E-01	4	8300
13.	C2H6+H=C2H5+H2	5.40E+02	3.5	5210
14.	C2H4+H=C2H3+H2	1.10E+14	0	8500
15.	CH2+CH3=C2H4+H	3.00E+13	0	0
16.	H+C2H4(+M)=C2H5(+M)	2.21E+13	0	2066
	Low pressure limit:	6.37E+27	-2.76	-54
	H2 Enhanced by	2.00E+00		
17.	C2H5+H=CH3+CH3	1.00E+14	0	0
18.	H2+C2H=C2H2+H	4.09E+05	2.4	864.3
19.	H+C2H2=C2H3	2.33E+11	0	-1284
20.	C2H3+H=C2H2+H2	4.00E+13	0	0
21.	C2H3+CH2=C2H2+CH3	3.00E+13	0	0
22.	C2H3+C2H=C2H2+C2H2	3.00E+13	0	0
23.	C2H3+CH=CH2+C2H2	5.00E+13	0	0
24.	CH2(SING)+M=CH2+M	1.00E+13	0	0
	H Enhanced by	0.00E+00		
25.	CH2(SING)+CH4=CH3+CH3	4.00E+13	0	0
26.	CH2(SING)+C2H6=CH3+C2H5	1.20E+14	0	0
27.	CH2(SING)+H2=CH3+H	7.00E+13	0	0
28.	CH2(SING)+H=CH2+H	2.00E+14	0	0
29.	CH2+CH2=C2H2+H2	4.00E+13	0	0
30.	C2H2+M=C2H+H+M	4.20E+16	0	107000
31.	C2H4+M=C2H2+H2+M	1.50E+15	0	55800
32.	C2H4+M=C2H3+H+M	1.40E+16	0	82360
33.	H+H+M=H2+M	1.00E+18	-1	0
	H2 Enhanced by	0.00E+00		
34.	H+H+H2=H2+H2	9.20E+16	-0.6	0

6.2.4 CVD of Diamond in a Simple 2-D Reactor

The model was used to compute the deposition rates of diamond in Tables (6.4) and (6.3), were based on the work of Dandy and Coltrin (1995); Coltrin and Dandy (1993). The purpose of this study was to test the solver on a CVD system with substantial gas phase chemistry, since the previous studies focused on CVD of tungsten, which was assumed to have no gas phase reactions occurring during the deposition.

The simulation was conducted on a two-dimensional square domain, which was discretized into a uniform 21 × 21 grid. The length of the sides of the domain was 10 cm. This domain could be thought of to represent a simplified model of a long horizontal reactor with a square cross-section. It was assumed that the susceptor consisted of the entire left wall and was maintained at a constant 1200 K for $t > 0$. The top and bottom walls were insulated, and the right wall was externally heated to 2500 K. It was assumed in the computations that deposition occurred only on the susceptor surface.

The feed gas to the reactor was a mixture of 1% CH_4 (mole fraction) in H_2 at 40 Torr. It was assumed that the gas entered a heater which isobarically heated the gas to 2200 K. A kinetic computation was performed using Lutz (1997) assuming that the residence time was 1 s, and the reaction temperature was 2200 K. The computations yielded the initial condition for the inlet gas mole fractions:

$$\chi_{H} = 1.490 \times 10^{-3} \qquad \chi_{H_2} = 9.882 \times 10^{-1} \qquad \chi_{AR} = 0.0$$

$$\chi_{C_2H} = 3.557 \times 10^{-11} \qquad \chi_{C_2H_3} = 1.874 \times 10^{-6} \qquad \chi_{CH_2} = 3.837 \times 10^{-7}$$

$$\chi_{C} = 2.345 \times 10^{-8} \qquad \chi_{C_2H_5} = 9.920 \times 10^{-7} \qquad \chi_{CH} = 2.651 \times 10^{-9}$$

$$\chi_{CH_2(SING)} = 3.493 \times 10^{-9} \qquad \chi_{CH_4} = 9.191 \times 10^{-3} \qquad \chi_{CH_3} = 3.627 \times 10^{-4}$$

$$\chi_{C_2H_2} = 3.459 \times 10^{-4} \qquad \chi_{C_2H_4} = 2.753 \times 10^{-4} \qquad \chi_{C_2H_6} = 1.169 \times 10^{-4}.$$

The initial site fractions were

$$z_{CH(S)} = 0.9544$$

$$z_{C(S,R)} = 0.0456.$$

The simulation was conducted for $0 < t < 5.0$ s. The time step was 0.01 s. The results are shown in Figs. (6.21) and (6.22). In Fig. (6.21) contours of CH_4 and H are shown at $t = 5.0$ s. Thermal diffusion played an important role in the distribution of CH_4, H, and all other species in the system. The Rayleigh number of the flow was quite low ($\mathsf{Ra} \approx 10$), since the fluid density was small. The fluid density was small because approximately 93% of its mass was H_2. The mass fractions of H and CH_4 were 2.8×10^{-3} and 4.4×10^{-3}, respectively. Pathlines in the flowfield are shown in Fig. (6.22)(a). The maximum fluid speed was approximately 0.7 $\mathrm{cm\,s^{-1}}$. The areal density of diamond is shown at time $t = 5.0$ s in Fig. (6.22)(b). The deposition profile was nearly uniform, due to the low Rayleigh number and high diffusion transport rates. The film growth rate predicted in this system was several orders of magnitude less than the growth rates reported in Dandy and Coltrin (1995). The most likely cause for this was that the temperature distribution was not conducive to the creation of the necessary precursors for diamond growth at the surface. The temperature distribution was approximately linear in the x-direction. Thus, the mean temperature was 1,800 K, while in the arc jet reactor simulations of Dandy and Coltrin (1995), most of the gas was closer to the exit temperature of the plasma arc jet. Furthermore, a species critical to diamond growth, atomic hydrogen, diffused away from the susceptor towards the hot wall as a result of thermal diffusion. At the susceptor surface, atomic hydrogen was rapidly consumed to make H_2.

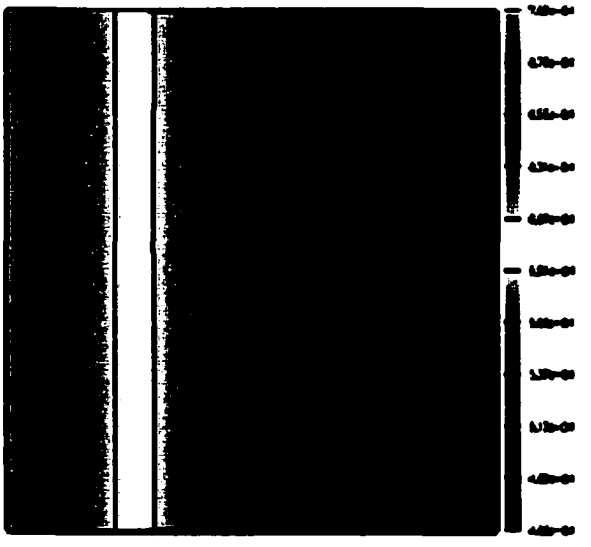

(a)

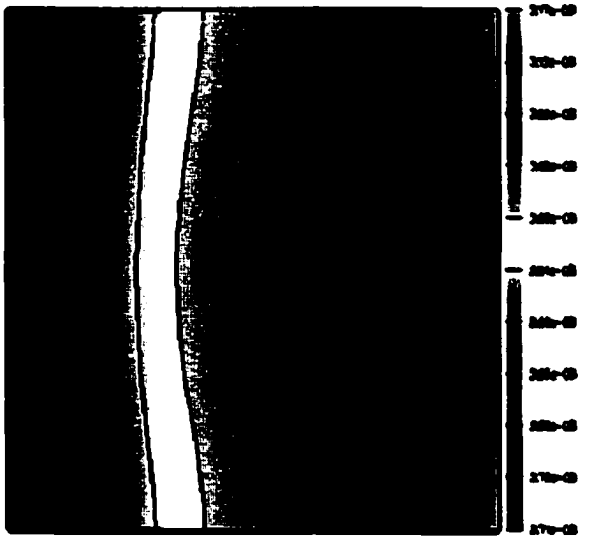

(b)

Figure 6.21: Contours of mole fraction of (a) methane and (b) atomic hydrogen at $t = 5.0$ s.

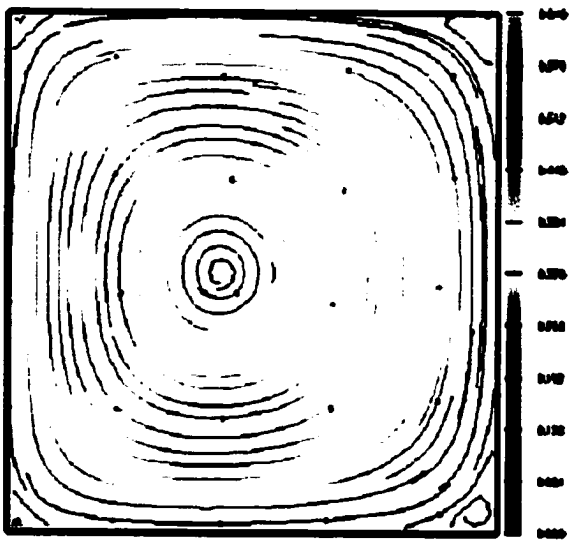

(a)

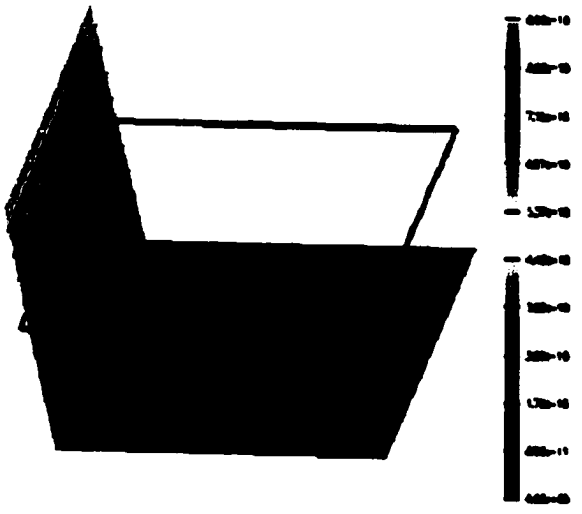

(b)

Figure 6.22: (a) Streamlines ($\mathrm{cm\,s^{-1}}$) and (b) diamond deposition areal density $\mathrm{g\,cm^{-2}}$ at $t = 5.0$ s.

6.3 CPU Costs of the CVD Batch Solver

A study was conducted to ascertain the CPU costs of the various components of the CVD batch model solver. This study was needed to determine which components, if significantly optimized, would improve the overall solver performance. The study was conducted by simulating a CVD batch system that had a large and complicated homogeneous and heterogeneous reaction mechanism.

The system of interest was CVD of silicon carbide. Homogeneous and heterogeneous reaction mechanisms for this system were developed by Allendorf and Kee (1991), and are shown in Tables 6.6 and 6.7, respectively. The gas phase mechanism consists of 33 gas phase species and 81 reactions, and the heterogeneous mechanism consists of 7 surface species, 2 bulk species, and 35 reactions.

A simulation was conducted on a 21 × 21 grid for 20 iterations. Each iteration took approximately 89 s, and the total memory requirements were approximately 35 MB. A summary of the CPU cost as a percentage of the total computation time is shown in Table (6.5).

Referring to the table, over 90% of the total CPU time was used in the stiff solve, species solve, and the computation of the multicomponent diffusion coefficients.

The stiff solve took nearly two-thirds of the total CPU time, due to the complexity of the reaction mechanism. Fortunately, the stiff solves are perfectly parallelizable, and one would take advantage of this in a parallel computing environment.

The computation of the $\mathbf{\Gamma}$, the effective multicomponent diffusion coefficients took nearly 18% of the total CPU time These results were rather startling, because it took much longer to compute $\mathbf{\Gamma}$ than it did to compute $\boldsymbol{D}$, the matrix of multicomponent diffusion coefficients. Even though the computation of $\boldsymbol{D}$ requires the computation of the inverse of an $M \times M$ matrix, where M is the number of gas species, this can be done iteratively with an optimized LAPACK routine (Anderson et al., 1999). The computation of $\mathbf{\Gamma}$ requires a matrix multiply $\boldsymbol{A} \times \boldsymbol{B}$, where $\boldsymbol{A}$ and $\boldsymbol{B}$ are both

Model Component	CPU Time (% of Total)
Slow Part of Species Equation	9.16
Slow Part of Energy Equation	0.33
Stiff Species and Energy Equations	65.10
Momentum Equation	0.14
Hydrostatic Pressure Equation	0.16
Pressure Correction Equation	0.12
$\mathbf{\Gamma}$	17.86
$\boldsymbol{d}^{\Gamma}$ and k	3.33
μ	0.36
$\boldsymbol{j}$	0.70
Other fluid properties	0.70
Miscellaneous	2.04
Total	100.00

Table 6.5: CPU cost associated with the batch CVD solver for a sample CVD problem with large homogeneous and heterogeneous reaction mechanism.

$M \times M$ matrices. This calculation is thus an order M^3 operation at every grid point. Fortunately, computing $\mathbf{\Gamma}$ every iteration is probably not necessary. Performing the calculations every third or fourth iteration would yield tremendous savings in total CPU time. Not computing the fluid properties every iteration would decrease the accuracy of the solution, but studies could be performed to determine the tradeoff between the solution accuracy and computational cost.

The species equation (slow) solves took about 9% of the total CPU time. This was due to the large number of gas phase species. CPU savings would be realized if the $\nabla \cdot (s\nabla)$ operator was better optimized, since this term is called M^2 times per iteration.

The momentum equation took only 0.14% of the total CPU time. This was due to the fact that the same operator was used for all three components of the momentum equation. This operator changes each iteration, however.

The pressure equation solves consumed all approximately the same amount of time as the momentum equation. The energy equation took a bit more time, since there were many terms that needed to be evaluated.

Table 6.6: Homogeneous Reactions in CVD of Silicon Carbide: $k = A\theta^b \exp(-E/\mathcal{R}\theta)$.

	REACTION	A	b	E
1.	C3H8=CH3+C2H5	1.70E+16	0	84840
2.	CH3+C3H8=CH4+N*C3H7	1.10E+15	0	25140
3.	H+C3H8=H2+N*C3H7	5.62E+07	2	7700
4.	I*C3H7=CH3+C2H4	2.00E+10	0	29500
5.	N*C3H7=CH3+C2H4	9.55E+13	0	31000
6.	C2H3+C3H8=C2H4+I*C3H7	1.00E+11	0	10400
7.	C2H5+C3H8=C2H6+I*C3H7	1.00E+11	0	10400
8.	C3H6+H=CH2CHCH2+H2	5.01E+12	0	1500
9.	C3H6+C2H5=CH2CHCH2+C2H6	1.00E+11	0	9200
10.	C3H8+CH2CHCH2=N*C3H7+C3H6	3.98E+11	0	16200
11.	C3H6=CH2CHCH2+H	1.00E+13	0	78000
12.	CH2CHCH2+H=C3H4+H2	1.00E+13	0	0
13.	CH4+H=CH3+H2	2.20E+04	3	8750
14.	CH2+H=CH+H2	1.00E+18	-1.6	0
15.	CH+CH2=C2H2+H	4.00E+13	0	0
16.	CH+CH4=C2H4+H	6.00E+13	0	0
17.	C2H6+H=C2H5+H2	5.40E+02	3.5	5210
18.	CH2+CH3=C2H4+H	3.00E+13	0	0
19.	H2+C2H=C2H2+H	4.09E+05	2.4	864.3
20.	C2H3+C2H=C2H2+C2H2	3.00E+13	0	0
21.	CH2+CH4=CH3+CH3	4.00E+13	0	0
22.	CH2+H=CH2+H	2.00E+14	0	0
23.	CH2+C2H2=H2CCCH+H	1.20E+13	0	6600
24.	C2H4+M=C2H2+H2+M	1.50E+15	0	55800
25.	CH3+C3H8=CH4+I*C3H7	1.10E+15	0	25140
26.	H+C3H8=H2+I*C3H7	8.71E+06	2	5000
27.	I*C3H7=H+C3H6	6.31E+13	0	36900
28.	N*C3H7=H+C3H6	1.26E+14	0	37000
29.	I*C3H7+C3H8=N*C3H7+C3H8	3.02E+10	0	12900
30.	C2H3+C3H8=C2H4+N*C3H7	1.00E+11	0	10400
31.	C2H5+C3H8=C2H6+N*C3H7	1.00E+11	0	10400
32.	C3H6+CH3=CH2CHCH2+CH4	8.91E+10	0	8500
33.	C3H8+CH2CHCH2=I*C3H7+C3H6	3.98E+11	0	16200
34.	CH2CHCH2=C3H4+H	3.98E+13	0	70000
35.	C3H6=C2H3+CH3	6.31E+15	0	85800
36.	CH2CHCH2+CH3=C3H4+CH4	1.00E+12	0	0
37.	CH3+H=CH2+H2	9.00E+13	0	15100
38.	CH+CH=C2H+H	1.00E+14	0	0
39.	CH+CH3=C2H3+H	3.00E+13	0	0
40.	C2H6+CH3=C2H5+CH4	5.50E+00	4	8300
41.	C2H4+H=C2H3+H2	1.10E+14	0	8500
42.	C2H5+H=CH3+CH3	1.00E+14	0	0
43.	C2H3+H=C2H2+H2	4.00E+13	0	0
44.	C2H3+CH=CH2+C2H2	5.00E+13	0	0
45.	CH2+C2H6=CH3+C2H5	1.20E+14	0	0
46.	CH2+CH2=C2H2+H+H	4.00E+13	0	0
47.	C2H2+M=C2H+H+M	4.20E+16	0	107000
48.	C2H4+M=C2H3+H+M	1.40E+16	0	82360

CONTINUED ON NEXT PAGE

	CONTINUED FROM PREVIOUS PAGE REACTION	A	b	E
49.	H+H+H2=H2+H2	9.20E+16	-0.6	0
50.	SIH4=SIH3+H	3.69E+15	0	93000
51.	SIH4+H=SIH3+H2	1.46E+13	0	2500
52.	SIH4+SIH=SI2H3+H2	1.45E+12	0	2000
53.	SIH2=SI+H2	1.06E+14	-0.9	45000
54.	SIH2+H=SIH3	3.81E+13	0	2000
55.	SIH2+SI2=SI3+H2	3.55E+11	0	2000
56.	H2SISIH2=SI2H2+H2	3.16E+14	0	53000
57.	H2+SIH=SIH3	3.45E+13	0	2000
58.	H2+SI2=SIH+SIH	1.54E+13	0	40000
59.	SI2H5=SI2H3+H2	3.16E+14	0	53000
60.	H+SI2=SIH+SI	5.15E+13	0	5300
61.	SIH2+SI2H6=SI3H8	1.81E+14	0	0
62.	CH3+CH3(+M)=C2H6(+M)	9.03E+16	-1.2	654
	Low pressure limit	3.18E+41	-7.13	2762
	TROE centering[2]:	6.04E-01	6927	132
	H2 Enhanced by	2		
63.	H+C2H4(+M)=C2H5(+M)	2.21E+13	0	2066
	Low pressure limit:	6.37E+27	-2.76	-54
	H2 Enhanced by	2		
64.	CH2+M=CH2+M	1.00E+13	0	0
	H Enhanced by	0.000E+00		
65.	H3SISIH=H2SISIH2	1.15E+20	-3.1	6630
66.	SIH4=SIH2+H2	6.67E+29	-4.8	63450
67.	SI2H6=SIH4+SIH2	3.24E+29	-4.2	58000
68.	SIH4+SIH3=SI2H5+H2	1.77E+12	0	4400
69.	SIH4+SIH=SI2H5	1.43E+13	0	2000
70.	SIH2+H=SIH+H2	1.39E+13	0	2000
71.	SIH2+SIH3=SI2H5	6.58E+12	0	2000
72.	SIH2+SI3=SI2H2+SI2	1.43E+11	0	16200
73.	SI2H6=H3SISIH+H2	7.94E+15	0	56400
74.	H2+SI2=SI2H2	1.54E+13	0	2000
75.	H2+SI3=SI+SI2H2	9.79E+13	0	47200
76.	SI2H2+H=SI2H3	8.63E+14	0	2000
77.	H3SISIH+SIH4=SI3H8	6.02E+13	0	0
78.	SIH3+SI2H5=SI3H8	3.31E+13	0	0
79.	CH3+H(+M)=CH4(+M)	6.00E+16	-1	0
	Low pressure limit:	8.00E+26	-3	0
	SRI centering:	4.50E-01	797	979
	H2 Enhanced by	2.00		
80.	H+C2H2(+M)=C2H3(+M)	5.54E+12	0	2410
	Low pressure limit:	2.67E+27	-3.5	2410
	H2 Enhanced by	2		
81.	H+H+M=H2+M	1.00E+18	-1	0
	H2 Enhanced by	0.000E+00		

[2]Parameters listed in this row are not A, b, and E. Details may be found in Coltrin et al. (1996).

Table 6.7: Heterogeneous Reactions in CVD of Silicon Carbide: $k = A\theta^b \exp(-E/\mathcal{R}\theta)$.

	REACTION	A	b	E
1.	H+SI(S)=>SI(S)-H	2.18E+12	0.5	0
2.	H+C(S)=>C(S)-H	2.18E+12	0.5	0
3.	2SI(S)-H=>2SI(S)+H2	7.23E+24	0	61000
4.	2C(S)-H=>2C(S)+H2	7.23E+24	0	61000
5.	CH4+SI(S)=>C(S)+B1(B)+2H2	4.20E+07	0.5	0
6.	CH3+SI(S)=>CH(S)+B1(B)+H2	8.67E+11	0.5	0
7.	CH2+SI(S)=>C(S)+B1(B)+H2	8.97E+11	0.5	0
8.	CH+SI(S)=>CH(S)+B1(B)	9.31E+11	0.5	0
9.	C2H5+2SI(S)=>C(S)+CH(S)+2H2+2B1(B)	5.76E+20	0.5	0
10.	C2H4+2SI(S)=>2C(S)+2H2+2B1(B)	9.37E+17	0.5	0
11.	C2H3+2SI(S)=>C(S)+CH(S)+2B1(B)+H2	5.97E+20	0.5	0
12.	C2H2+2SI(S)=>2C(S)+2B1(B)+H2	1.22E+19	0.5	0
13.	I*C3H7+3SI(S)	4.36E+29	0.5	0
	=>2C(S)+CH(S)+3B1(B)+3H2			
14.	N*C3H7+3SI(S)	4.36E+29	0.5	0
	=>2C(S)+CH(S)+3H2+3B1(B)			
15.	C3H6+3SI(S)=>3C(S)+3H2+3B1(B)	7.06E+26	0.5	0
16.	C3H4+3SI(S)=>3C(S)+3B1(B)+2H2	4.52E+29	0.5	0
17.	H2CCCH+3SI(S)=>2C(S)+CH(S)			
	+H2+3B1(B)	4.58E+29	0.5	0
18.	SIH2(S)=>SI(S)+H2	2.91E+14	0	9000
19.	CH2CHCH2+3SI(S)	4.47E+29	0.5	0
	=>2C(S)+CH(S)+2H2+3B1(B)			
20.	C3H2+3SI(S)=>3C(S)+H2+3B1(B)	4.64E+29	0.5	0
21.	SIH2+C(S)=>B2(B)+SIH2(S)	6.12E+11	0.5	0
22.	SIH4+C(S)=>B2(B)+SIH2(S)+H2	3.18E+10	0.5	18678
23.	SIH3+C(S)=>B2(B)+SIH(S)+H2	6.03E+11	0.5	0
24.	SIH+C(S)=>B2(B)+SIH(S)	6.23E+11	0.5	0
25.	SI+C(S)=>B2(B)+SI(S)	6.33E+11	0.5	0
26.	SI2H5+2C(S)	3.95E+20	0.5	0
	=>2B2(B)+SIH(S)+SIH2(S)+H2			
27.	SI2H3+2C(S)=>2B2(B)+SIH2(S)			
	+SIH(S)	4.02E+20	0.5	0
28.	SI2+2C(S)=>2B2(B)+2SI(S)	4.14E+20	0.5	0
29.	SI2H6+2C(S)=>2SI(S)+2B2(B)+3H2	2.11E+20	0.5	18678
30.	H3SISIH+2C(S)=>2B2(B)+2SIH2(S)	4.00E+20	0.5	0
31.	H2SISIH2+2C(S)=>2B2(B)+2SIH2(S)	4.00E+20	0.5	0
32.	SI2H2+2C(S)=>2B2(B)+2SIH(S)	4.07E+20	0.5	0
33.	SI3+3C(S)=>3B2(B)+3SI(S)	2.30E+29	0.5	0
34.	2CH(S)=>2C(S)+H2	2.25E+24	0	61000
35.	2SIH(S)=>2SI(S)+H2	2.25E+24	0	61000

Chapter 7

CONCLUSION

7.1 Summary of Work

A model of chemical vapor deposition batch reactors was developed based on a finite difference method and implemented using the overset grid method. A solver was written in object-oriented C++ and FORTRAN using the OVERTURE library to manipulate overset grids and perform other tasks necessary to solve partial differential equations. The CHEMKIN library was used to compute the gas phase reaction rates and thermodynamic properties. The SURFACE CHEMKIN library was used to compute the heterogeneous reaction rates, and CHEMKIN TRANSPORT was used to compute the transport properties.

A new method for computing rigorous multicomponent diffusion was implemented. In this approach, the ordinary multicomponent diffusion coefficients are transformed into a new matrix of effective multicomponent diffusion coefficients by means of a matrix transformation. This matrix is shown in Wangard et al. (2000) to have several properties that simplify the solution of large systems of coupled species equations. In short, a diagonalized implicit scheme is used for the diffusion terms. In the linearized case, the diffusion equation (less reaction and convection terms) is unconditionally stable. This scheme fully decouples the species equations from each other.

A first-order splitting is used to solve the species and energy equations, since they are tightly coupled by source terms from homogeneous and heterogeneous chemical reactions. The fast (stiff) part of the equations form a stiff system of ordinary differential equations at each grid point, while the slow (non-stiff) parts form a set

of partial differential equations that are spatially coupled, but relatively easy to solve.

The momentum equation is solved by a variable coefficient projection method. The momentum equation is solved by first determining the hydrostatic pressure field, that is the pressure field that would exist in a static fluid. The momentum equation is then solved in each coordinate direction. The same operator is used for all three coordinate directions. A standard variable density projection is then used to obtain a velocity field that satisfies continuity.

7.2 Review of Results

Referring to the CVD validation study, it is evident that the solver conserves mass, and predicts deposition rates consistent with that of other models. Of course, the meaningfulness of the result depends wholly on the model describing the reaction kinetics. This type of model is not particularly good for testing out new types of reaction mechanisms, due to the large computational overhead. Instead, a simple 1-D model would be preferable. The preferred use of this work is to examine the effects of reactor geometry and system operating conditions on the resulting deposition uniformity.

The natural convection studies showed that the formation of buoyancy rolls may be beneficial. A multicomponent natural convection study showed that it is possible to generate very nearly uniform surface composition conditions at a deposition surface in a batch reactor. Indeed, the uniform surface conditions in the multicomponent natural convection study resulted from the presence buoyancy rolls in a bottom-heated reactor.

The natural convection studies also provided insight as to how to reduce or eliminate vortex shedding. Vortex shedding is highly undesirable because it is unlikely

that uniform conditions could occur at any deposition surface. The instabilities result from large thermal gradients, especially if the hot region is lower than the cold region. Insulating hot surfaces from cold surfaces or introducing temperature transition zones may reduce or eliminate vortex shedding.

Three separate CVD mechanisms were tested. The first mechanism was used to model CVD of tungsten by H_2 reduction WF_6. This model consisted of a simple heterogeneous mechanism and no gas phase chemistry. The second mechanism included both homogeneous and heterogeneous kinetics and was used to model CVD of diamond. The third mechanism was an elaborate homogeneous and heterogeneous model of CVD of silicon carbide. This last mechanism was tested to assess the CPU usage for a large, complicated reaction mechanism.

It was found in the timing study, that the majority of CPU time was spent in the stiff reaction solve. This was not unexpected, given the complexity of the mechanism. Also, a significant portion (20%) of the CPU time was spent computing the effective ordinary multicomponent diffusion coefficients. This was due to the that computing Γ required M^3 operations at each grid point, where M is the number of gas phase species. This results from the transformation given by Eq. (2.39), which consists of the matrix multiplication of $\boldsymbol{WDW}$ with $\boldsymbol{C}$. The cost of solving the species equations was about 9%, because there were so many (33) equations.

7.3 Recommendations

The solver can be improved in many ways. A list of the following recommendations is as follows:

- Implement parallelism to the stiff solver component. Since the stiff equations parallelize perfectly, a parallelized stiff solver would yield tremendous improvements in total CPU usage, especially in systems with complicated reaction

mechanisms.

- Parallelize the computation of fluid properties. This would involve developing a parallel computational equivalent of CHEMKIN and CHEMKIN TRANSPORT.

- Decrease CPU time associated with computation of the effective ordinary diffusion coefficients, $\mathbf{\Gamma}$. Another approach would be to reconsider a new formulation of the diffusion coefficients which is defined to operate on the vector of mass fraction gradients. This subject is discussed in Section 4.4.9 of Ern and Giovangigli (1994). Lastly, the CPU time associated with the diffusion coefficients may be reduced by not computing them every iteration; the error of such a simplification could investigated.

- Optimize the $\nabla\cdot(s\nabla)$ operator in OVERTURE. Presently, this operator accepts only single component scalar grid functions. In the species continuity equations, this operator is called for each element of $\rho\mathbf{\Gamma}$ and the vector of thermal diffusion coefficients. If the operator were written to accept matrix arguments, such as $\rho\mathbf{\Gamma}$, and assuming that the operator returned a multicomponent grid function in which the mnth component contained $\nabla\cdot(\rho\Gamma_{mn}\nabla)$, CPU time could be reduced by vectorizing computations in the operator function.

- Combine the hydrostatic and pressure projection equations into one overall pressure equation. This would save one Poisson solve. This suggestion was attempted without success.

7.4 CVD in Continuous Flow Systems

The following changes are necessary to convert the CVD batch solver to a CVD continuous flow reactor (CFR) solver. These changes are to be made to the governing equations and additional boundary conditions are needed.

7.4.1 Changes to Governing Equations

Converting the batch CVD code to a CFR code requires no changes to the governing equations of species conservation, continuity, and momentum. However, the batch CVD reactor is a constant-volume system, the c_v form of the energy equation was used in the present work. In the CFR, the background pressure is constant, and thus the c_p-form of the energy equation is preferable, where c_p is the mean specific heat capacity at constant pressure defined by

$$cp = \sum_{m=1}^{M} c_{p_m} \psi_m, \tag{7.1}$$

where c_{p_m} is the specific heat capacity of the mth species. The c_p-form of Eq. (2.6) is given by the following:

$$\rho c_p \frac{D\theta}{Dt} = \nabla \cdot (k \nabla \theta) - \sum_{m=1}^{M} \left(h_m r_m + c_{p_m} (\boldsymbol{j}_m \cdot \nabla \theta) \right), \tag{7.2}$$

where h_m is the specific enthalpy of the mth species, including the energy of formation, and it is assumed that Dp/Dt is considered negligible.

The splitting of Eq. (7.2) is analogous to the procedure given in Section 5.3.2. The fast part of this equation given by

$$\frac{\partial \theta}{\partial t} = -\frac{1}{\rho c_p} \sum_{m=1}^{M} h_m r_m \tag{7.3}$$

would be used instead of Eq. (5.9). The discretization of the slow part is given by

$$\left[\rho^n c_p^n \left(\frac{1}{\Delta t} \boldsymbol{I} - \boldsymbol{u}^n \cdot \nabla \right) - \nabla \cdot (k^n \nabla) + \sum_m c_{p_m}^n \boldsymbol{j}_m^n \cdot \nabla \right] \theta^{n+1} = \frac{\rho^n c_p^n}{\Delta t} \theta^n, \tag{7.4}$$

and would be used instead of Eq. (5.25).

Also, since the background pressure is constant, the pressure smoothing steps performed after the fast and slow energy and species solves would consist of enforcing the consistency of the ideal gas law as follows:

$$\rho^{n+1} = \frac{p}{R^{n+1} \theta^{n+1}} \tag{7.5}$$

7.4.2 Boundary Conditions

Two additional boundary conditions appear in a CFR: (1) inflow and (2) outflow boundaries. The following modifications are necessary to add these two boundary condition types to the solver. First, all fluid properties, such as viscosity, thermal conductivity, diffusion coefficients, etc. should be extrapolated to the ghost line. At the inflow boundaries, Dirichlet conditions may be imposed at the boundary nodes for the velocity components, the mass fractions, and the temperature. At the outflow surfaces, Neumann conditions are imposed on the velocity components, the mass fractions, and the temperature. Also, at the outflow boundaries, homogeneous Dirichlet conditions are imposed on the velocity projection equation, Eq. (5.57), since the velocity at the outflow is not known. Since the gradient of the projection is used to correct the velocity field, a homogeneous Dirichlet conditions on the projection equation allow the normal component of the velocity at outflow boundaries to change after the projection step. Finally, it is noted that the projection equation system is not singular, and the solution method is simpler than in the present work.

Bibliography

Allendorf, M. D. and Kee, R. J. (1991). A model of silicon carbide chemical vapor deposition. *Journal of the Electrochemical Society*, 138(3):841–852.

Anderson, E., Bai, Z., Bischof, C., Blackford, S., Demmel, J., Dongarra, J., Croz, J. D., Greenbaum, A., Hammarling, S., McKenney, A., and Sorensen, D. (1999). *LAPACK Users' Guide*. The Society for Industrial and Applied Mathematics, third edition.

Anderson, J. D. (1989). *Introduction to Flight*. McGraw-Hill Book Company, New York, NY. 3rd edition.

Arora, R. and Pollard, R. (1991). A mathematical model for chemical vapor deposition processes influenced by surface reaction kinetics: Application to low-pressure deposition of tungsten. *Journal of the Electrochemical Society*, 138(5):1523–1537.

Balay, S., Gropp, W., McInnes, L. C., and Smith, B. (1996). *PETSc 2.0 Users Manual*. Mathematics and Computer Science Division, Argonne National Laboratory, Argonne. IL. ANL-95/11 - Revision 2.0.22.

Belfiore, L. (1999). Transport phenomena in chemical reactors. Unpublished.

Bell, J. B., Solomon, J. M., and Szymczak, W. G. (1994). Projection method for viscous incompressible flow in quadrilateral grids. *AIAA Journal*, 32(10).

Bird, R., Stewart, W. E., and Lightfoot, E. N. (1960). *Transport Phenomena*. John Wile & Sons, New York, NY.

Blewer, B. and McConica, C., editors (1989). *Tungsten and Other Refractor Metals for VLSI Applications IV*. The Materials Research Society, Pittsburgh, PA.

Boltzmann, L. (1964). *Lectures on Gas Theory.* University of California Press, Berkely and Los Angeles, CA. Originally published under the title *Vorlesungen über Gastheorie* by J. A. Barth, Leipzig—Part I, 1896; Part II, 1898.

Cengel, Y. A. and Boles, M. A. (1989). *Thermodynamics: An Engineering Approach.* McGraw-Hill Publishing Company, New York, NY.

Chapman, S. and Cowling, T. G. (1939). *The Mathematical Theory of Non-uniform Gases.* Cambridge University Press.

Chesshire, G. S. and Henshaw, W. D. (1999). *The Overture Grid Classes Users' Guide, Version 1.0.* Scientific Computing Group (CIC-19), Los Alamos National Laboratory, Los Alamos, NM and Center for Applied Scientific Computing, Lawrence Livermore National Laboratory, Livermore, CA.

Chorin, A. J. (1967). A numerical method for solving incompressible viscous flow problems. *Journal of Computational Physics*, 2:12–26.

Cohen, S. D. and Hindmarsh, A. C. (1994). *CVODE User Guide.* Center for Computation Sciences & Engineering, Lawrence Livermore National Laboratory, Livermore, CA.

Coltrin, M. E. and Dandy, D. S. (1993). Analysis of diamond growth in subatmospheric dc plasma-gun reactors. *Journal of Applied Physics*, 74(9):5803–5820.

Coltrin, M. E., Kee, R. J., and Miller, J. A. (1984). A mathematical model of the coupled fluid mechanics and chemical kinetics in a chemical vapor deposition reactor. *Journal of the Electrochemical Society*, 131(2):425–434.

Coltrin, M. E., Kee, R. J., Rupley, F. M., and Meeks, E. (1996). *Surface Chemkin-III: A Fortran Package for Analyzing Heterogeneous Chemical Kinetics at a Solid-Surface — Gas-Surface Interface.* Sandia National Laboratory, Albuquerque, NM. SAND96-8217.

Coltrin, M. E., Wixom, R. R., and Dandy, D. S. (2000). *Surfkin: A Program to Solve Transient and Steady State heterogeneous Reaction Kinetics.* Sandia National Laboratory, Albuquerque, NM. SAND2000-1202.

Connell, S. D. and Stow, P. (1986). The pressure correction method. *Computers & Fluids*, 14(1):1–10.

Dandy, D. S. (2000). Private communication.

Dandy, D. S. and Coltrin, M. E. (1995). A simplified analytical model of diamond growth in direct current arcjet reactors. *Journal of Materials Research*, 10(8):1993–2010.

Demirdzic, I. and Peric, M. (1990). Finite volume method for prediction of fluid flow in arbitrarily shaped domains with moving boundaries. *International Journal for Numerical Methods in Fluids*, 10:771–790.

Ern, A. and Giovangigli, V. (1994). *Multicomponent Transport Algorithms (Lecture Notes in Physics, New Series M : Monographs, Vol 24).* Springer-Verlag, New York, NY.

Ern, A. and Giovangigli, V. (1995). Fast and accurate multicomponent transport property evaluation. *Journal of Computational Physics*, 120:105–116.

Ern, A., Giovangigli, V., and Smooke, M. D. (1996). Numerical study of a three-dimensional chemical vapor deposition reactor with detailed chemistry. *Journal of Computational Physics*, 126(1):21–39. doi:10.1006/jcph.1996.0117.

Ferziger, J. H. and Kaper, H. G. (1972). *Mathematical theory of Transport Processes in Gases.* North-Holland Publishing Company, Amsterdam and American Elsevier Publishing Company, New York, NY.

Ferziger, J. H. and Peric, M. (1996). *Computational Methods for Fluid Dynamics.* Springer-Verlag, Berlin, Germany.

Gresho, P. M. and Sani, R. L. (1987). On pressure boundary conditions for the incompressible navier-stokes equations. *International Journal for Numerical Methods in Fluids*, 7:1111–1145.

Henshaw, W. D. (1998). *A Primer for Writine PDE Solvers with Overture.* Scientific Computing Group (CIC-19), Los Alamos National Laboratory, Los Alamos, NM. LA-UR-96-3894.

Henshaw, W. D. (1999a). *Ogen: An Overlapping Grid Generator for Overture.* Center for Applied Scientific Computing, Lawrence Livermore National Laboratory, Livermore, CA. UCRL-MA-132237.

Henshaw, W. D. (1999b). *PlotStuff: A Class for Plotting Stuff from Overture; based on GL_GraphicsInterface, A Graphics Interface Based on OpenGL; based on GenericGraphicsInterface, A Generic Graphics Interace. User Guide, Version 1.00.* Center for Applied Scientific Computing, Lawrence Livermore National Laboratory, Livermore CA. UCRL-MA-132238.

Henshaw, W. D. (2000). *Overture Finite Difference Operators and Boundary Conditions.* Center for Applied Scientific Computing, Lawrence Livermore National Laboratory, Livermore CA.

Henshaw, W. D., Kreiss, H.-O., and Reyna, L. G. M. (1994). A fourth-order-accurate difference approximation for the incompressible navier-stokes equations. *Computers & Fluids*, 23(4):575–593.

Hirsch, C. (1988). *Numerical Computation of Internal and External Flows. Volume 1: Fundamentals of Numerical Discretization.* John Wiley & Sons.

Hirschfelder, J. O., Curtiss, C. F., and Bird, R. B. (1954). *The Molecular Theory of Gases and Liquids.* John Wiley & Sons, New York, NY.

Holstein, W. L. (1988). Thermal diffusion in metal-organic chemical vapor deposition. *Journal of the Electrochemical Society*, 135(7):1788–1793.

How, T. Y. and Wetton, B. T. R. (1991). Second-order convergence of a projection scheme for the incompressible navier-stokes equations with boundaries. *SIAM Journal of Numerical Analysis*, 30(3):609–629.

Huang, L. C. and Wu, Y. D. (1994). The component-consistent pressure correction projection method fo the incompressible navier-stokes equations. *Computers Math. Applic.*, 31(11):1–21.

Ismail, K. A. R. and Scalon, V. L. (2000). A finite element free convection model for the side wall heated cavity. *International Journal of Heat and Mass Transfer*, 43:1373–1389.

Jeans, J. H. (1925). *The Dynamical Theory of Gases.* Dover Publications, Inc., 4th edition.

Jenkinson, J. P. and Pollard, R. (1984). Thermal diffusion effects in chemical vapor deposition. *Journal of the Electrochemical Society*, 131(12):2911–2917.

Jensen, K. F. (1989). *Microelectronics Processing: Chemical Engineering Aspects*, chapter 5. American Chemical Society.

Kee, R. J., Dixon-Lewis, G., Warnatz, J., Coltrin, M. E., and Miller, J. A. (1986). *A Fortran Computer Code Package for the Evaluation of Gas-Phase Multicomponent Transport Properties.* Sandia National Laboratory, Albuquerque, NM. SAND86-8246.

Kee, R. J., Rupley, F. M., Meeks, E., and Miller, J. A. (1996). *Chemkin-III: A Fortran Chemical Kinetics Package for the Analysis of Gas Phase Chemical and Plasma Kinetics.* Sandia National Laboratory, Albuquerque, NM. SAND96-8216.

Kleijn, C. (1991). *Transport Phenomena in Chemical Vapor Deposition Reactors.* PhD thesis, Technishe Universiteit Magnificus.

Kleijn, C. R. and Hoogendoorn, C. J. (1991). Transport phenomena in tungsten lpcvd in a single-wafer reactor. *Journal of the Electrochemical Society*, 138(2):509–517.

Kleijn, C. R., van der Meer, H., and Hoogendoorn, C. J. (1989). A mathematical model for lpcvd in a single wafer reactor. *Journal of the Electrochemical Society*, 136(11):3423–3433.

Leal, L. G. (1992). *Laminar Flow & Convective Transport Processes. Scaling Principles & Asymptitic Analysis.* Butterworth-Heinemann.

Lutz, A. (1997). *Senkin v. 3.8.* Sandia National Laboratory, Albuquerque. NM.

Majda, A. and Sethian, J. (1985). The derivation and numerical solution of the equations for zero mach number combustion. *Combustion Science and Technology*, 42:185–205.

McConica, C. M., Baker, K., Bean, H., and Kuchta, E. (1994). Fundamental studies on integrated circuit chemical vapor deposition reactor design for waste minimization. *Unpublished.*

Moffat, H. K. and Jensen, K. F. (1988). Three-dimensional flow effects in silicon cvd in horizontal reactors. *Journal of the Electrochemical Society*, 135(2):459–471.

Monchick, L. and Mason, E. A. (1961). Transport properties of polar gases. *Journal of Chemical Physics*, 35:1676.

Morosanu, C. E. (1990). *Thin Films by Chemical Vapour Deposition.* Elsevier, New York, NY.

Nakamura, S. and Fasol, G. (1997). *The Blue Laser Diode.* Springer-Verlag, Berlin.

Okkerse, M., de Croon, M. H. J. M., Kleijn, C. R., van den Akker, H. E. A., and Martin, G. B. (1998). A surface and a gas-phase mechanism for the description of growth on the diamond(100) surface in an oxy-acetylene torch reactor. *Journal of Applied Physics*, 84(11):6387–6398.

Okkerse, M., Kleijn, C. R., van den Akker, H. E. A., de Croon, M. H. J. M., and Martin, G. B. (2000). Two-dimensional simulation of an oxy-acetylene torch diamond reactor with a detailed gas-phase and surface mechanism. *Journal of Applied Physics*, 88(7):4417–4428.

Panton, R. L. (1990). *Incompressible Flow.* John Wiley & Sons.

Patankar, S. V. (1980). *Numerical Heat Transfer and Fluid Flow.* Hemisphere Publishing Corporation.

Pember, R. B., Almgren, A. S., Bell, J. B., Colella, P., Howell, L., and Lai, M. (1999). A higher-order projection method for the simulation of unsteady turbulent non premixed combustion in an industrial burner. *Unknown.*

Press, W. H., Teukolsky, S. A., Vetterling, W. T., and Flannery, B. P. (1992). *Numerical Recipes in FORTRAN.* Press Syndicate of the University of Cambridge.

Quinlan, D. (1999). *A++/P++ Users Guide.* Scientific Computing Group (CIC-19), Los Alamos National Laboratory, Los Alamos, NM, Livermore, CA.

Salinger, A. G., Shadid, J. N., Hutchinson, S. A., Hennigan, G. L., Devine, K. D., and Moffat, H. K. (1999). Analysis of gallium arsenide deposition in a horizontal

chemical vapor deposition reactor using massively parallel computations. *Journal of Crystal Growth*, 203:516–533.

Sampath, W. S. (2001). Private communication.

Siegel, R. and Howell, J. R. (1981). *Thermal Radiation Heat Transfer*. Hemisphere Publishing Corporation, New York, NY, second edition.

Sportisse, B. (2000). An analysis of operator splitting techniques in the stiff case. *Journal of Computational Physics*, 161:140–168.

Strikwerda, J. C. (1989). *Finite difference schemes and partial differential equations*. Wadsworth & Brooks/Cole Advanced Books & Software, Pacific Grove, CA.

von Schubert, B. S. (1995). Approximate boundary conditions for the flow of a mixture of reacting gases. *Acta Mechanica*, 111:161–170.

Wangard, W., Dandy, D. S., and Miller, B. L. (2000). A numerically stable method for integration of the multicomponent species diffusion equations. submitted to *J. Comput. Phys.*

White, F. (1979). *Fluid Mechanics*. McGraw Hill Book Company.

Wilke, C. R. (1950). A viscosity equation for gas mixtures. *Journal of Chemical Physics*, 18:517–519.